2010

Novel sensorless generator control and grid fault ride-through strategies for variable-speed wind turbines and implementation on a new real-time simulation platform

Sheng Yang
Iowa State University

Novel sensorless generator control and grid fault ride-through strategies for variable-speed wind turbines and implementation on a new real-time simulation platform

by

Sheng Yang

A dissertation submitted to the graduate faculty

in partial fulfillment of the requirements for the degree of

DOCTOR OF PHILOSOPHY

Major: Electrical Engineering

Program of Study Committee:
Venkataramana Ajjarapu, Major Professor
James D. McCalley
Diane Rover
Zhengdao Wang
Zhijun Wu

Iowa State University

Ames, Iowa

2010

DEDICATION

I would like to dedicate this thesis to my wife Dan and to my son Kevin and to my daughter to be born without whose support I would not have been able to complete this work. I would also like to thank my family and friends for their loving guidance and financial assistance during the writing of this work.

TABLE OF CONTENTS

LIST OF TABLES

LIST OF FIGURES

ACKNOWLEDGEMENTS

I would like to take this opportunity to express my thanks to those who helped me with various aspects of conducting research and the writing of this thesis. First and foremost, my major professor Dr. Venkataramana Ajjarapu for his guidance, patience and support throughout this research and the writing of this thesis. His insights and words of encouragement have often inspired me and renewed my hopes for completing my Ph.D research. I would also like to thank my committee members for their efforts and contributions to this work: Dr. James D. McCalley, Dr. Diane Rover, Dr. Zhengdao Wang, and Dr. Zhijun Wu. I would additionally like to thank Mr. In Kwon Park for his excellent technical support for RTDS and Mr. Hao Chen and Mr. Di Wu for their kindly lab assistance.

ABSTRACT

This thesis contains studies regarding the modeling, control, and protection of variable-speed wind turbines and the real-time implementation.

The usage of MW-size variable-speed wind turbines as sources of energy has increased significantly during the last decade. Advantages over fixed-speed wind turbines include more efficient wind power extraction, reduced grid power fluctuation, and improved grid reactive power support. Two types of typical generation systems for large-size variable-speed wind turbines exist. One is the doubly-fed induction generator (DFIG) with a partial-scale power electronic converter. The other is the permanent-magnet synchronous generator (PMSG) with a full-scale power electronic converter. This thesis is to address the modeling of these two wind turbine systems, including the complete aerodynamic and mechanical and electrical components.

In this context, this thesis gives special focus on the mechanical sensorless control and grid fault ride-through strategies of variable-speed wind turbines. Improved solutions are analyzed and verified.

In the electrical controller of a DFIG, A mechanical speed sensor is normally required to provide accurate information of the machine speed and rotor position. However, sensorless operation is desirable because the use of a mechanical speed sensor coupled with the machine shaft has several drawbacks in terms of degraded robustness, extra cost and cabling, and difficult maintenance. In this thesis, the design and analysis of a new sensorless vector controller using a reduced-order state observer is addressed in detail. Results have revealed that the proposed sensorless observer is more robust against parameter variations than other speed estimation schemes.

Nowadays, almost all the grid code specifications over the world have included fault ride-through requirements for grid-connected wind turbines. In US, as mandated by the Federal Energy Regulatory Commission (FERC) Order 661-A, wind farms are required to remain online in the presence of severe voltage disturbances as low as 0.0 pu, as measured at the high voltage side of the wind generator step-up transformer, for up to 9 cycles (150 ms). These strict requirements present a significant challenge to the existing wind turbine technologies. In this thesis, an improved technique combining the traditional crowbar protection circuit and the demagnetizing current to ride-through symmetrical grid voltage dips is analyzed and verified for a DFIG-based wind turbine. This method reduces the crowbar activation time and helps the wind turbine resume its normal operation as soon as the fault is less severe, even before the fault clearance. This thesis also proposes an improved fault ride-through technique for a PMSG-based wind turbine to mitigate the dc-link overvoltage. This technique can be directly embedded into the original wind turbine electrical controller without using any extra protection hardware. It ensures the dc-link voltage is kept within the acceptable range during a voltage dip and the post-disturbance recovery period.

In this thesis, a novel integrated simulation platform is developed based on industry standard simulation tools, RTDS^{TM} and dSPACE^{TM}. The aforementioned wind generation systems and the proposed control and protection schemes are all modeled and implemented in real-time on this simulation platform. The necessary measures in hardware and software aspects to enable the collaborative simulation of these two industry standard simulators are addressed. Results have shown this integrated real-time simulation platform has broad application prospects in wind turbine control design and grid interconnection studies.

CHAPTER 1. INTORDUCTION

1.1 Background

1.1.1 Wind Energy

Sustainable development is an emerging theme for the twenty-first century due to the potential energy crisis and increasingly serious environmental issues. Especially, more environmentally benign electric power systems are playing a critical part of this new thrust. Wind energy systems in the United States and Europe have become the fastest growing source of electric power. Grid- tied photovoltaic systems are entering the marketplace in large numbers. Full cells that will generate electricity without emissions are on the horizon.

Winds result from the movement of air masses in the atmosphere. These movements of air are created by pressure differences that exert a force causing air masses to move from a region of high pressure to one of low pressure. These pressure differences are caused by differential solar heating of the atmosphere. Therefore, the wind energy can also be considered as an indirect form of solar energy.

Wind energy is not new to mankind. Wind has been utilized as a source of power for at least 3000 years, for grinding grain, pumping water, propelling sailing ships, and other early industrial applications. Today, due to the potential energy crisis and increasingly serious environmental issues, wind energy has become the most promising and fastest-growing renewable energy resource in many parts of world.

According to the Year End 2009 Market Report prepared by American Wind Energy Association, the U.S. wind industry installed close to 10,000 MW of new generating capacity in 2009, which broke all previous records. The total installed wind power capacity in the U.S. is

now over 35,000 MW in the end of 2009. The annual and cumulative wind power installations are shown in Figure 1.1.

In the map of cumulative wind capacity by state shown in Figure 1.2, Texas holds the leading position in wind capacity bringing it past the 9-GW mark. It is worth noting that Iowa now has a total of 3,670 MW installed, consolidating its second position, behind Texas and ahead of California. It is expected that wind can provide 20% of U.S. electricity needs by 2030 [1]. The total installed wind power capacity will reach 300 GW.

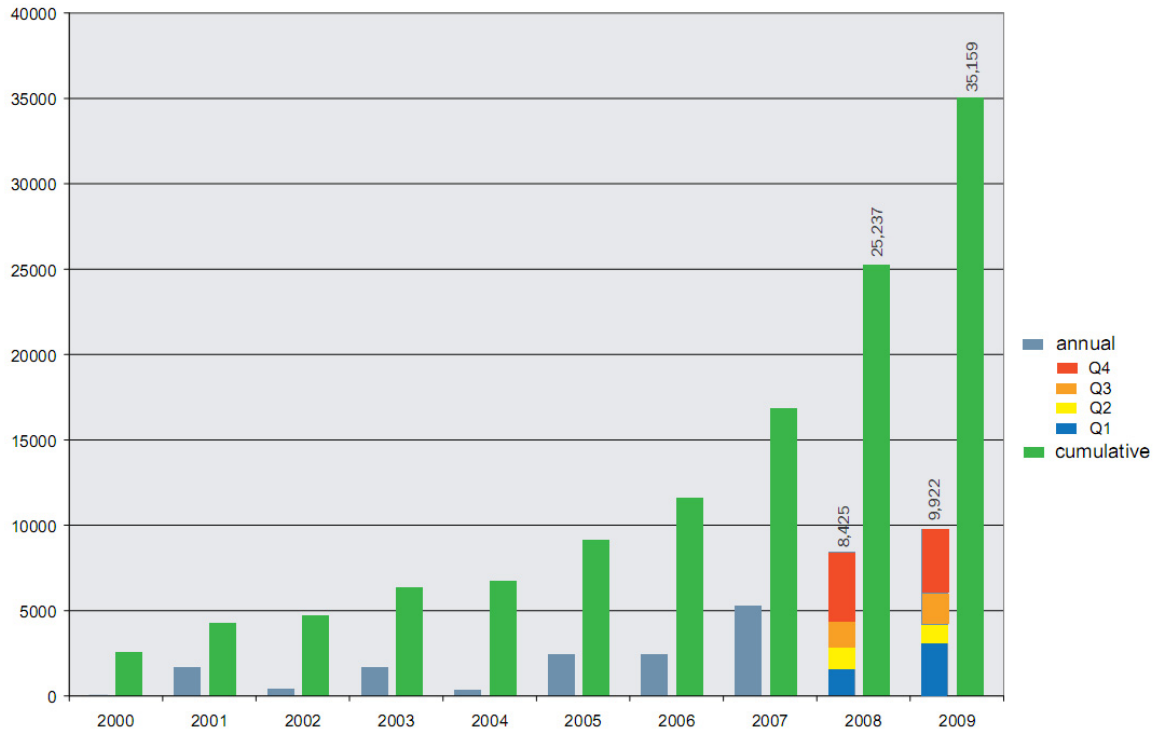

Figure 1.1 U.S. annual and cumulative wind power installations (sources: American Wind Energy Association, 4th Quarter 2009 Market Report).

1.1.2 Status and Challenges

Wind turbines convert the aerodynamic energy from winds to the electrical energy to be delivered to the power grid. Although the fundamental principle of wind energy conversion by a wind turbine is straightforward, a wind turbine itself is a complex system combining knowl-

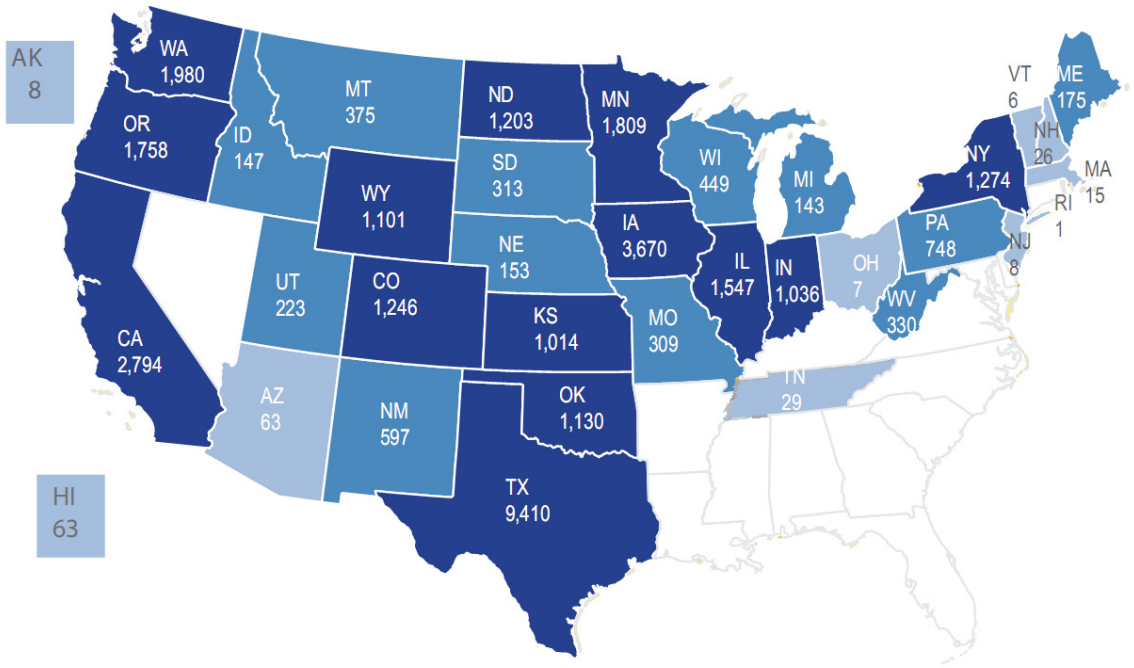

Figure 1.2 Cumulative wind capacity by state (sources: American Wind Energy Association, 4th Quarter 2009 Market Report).

edge of various fields, including aerodynamic, mechanical, structural, electrical, and control engineering.

In the last decade, two major technological developments have taken place in the field of wind turbine technology. Firstly, the size of an individual wind turbine or the scale of a wind farm has significantly increased to reduce the cost of wind power. The nominal power of an individual wind turbine has grown from several tens of KW to multi-MW class. A typical wind farm consists of several tens to hundreds of such wind turbines.

The second development in wind turbine technology is the switch from a fixed-speed wind turbine to a variable-speed wind turbine. The rotational speed of a fixed-speed wind turbine is determined by the frequency of the power grid, the gear ratio and the generator design. It does not depend on the wind speeds, which never keep a constant value in reality. On the other hand, the rotational speed of a variable-speed wind turbine can be controlled within

certain design limits to accommodate the wind variability. Obviously the variable-speed wind turbine has substantial advantages over the fixed-speed wind turbines in many aspects, such as increased energy yield, improved power quality, and enhanced reactive power support in grid fault conditions. Most wind turbine manufacturers have now changed the design of their main products to the variable-speed concept. The market share of variable-speed wind turbines was already over 70 percent in 2002 [2].

The advanced features of variable-speed wind turbines require a more complicated and sophisticated control system to complete all the tasks. The main tasks of the control system of a variable-speed wind turbine are to

- control the electrical power extracted from the aerodynamic power captured by the wind turbine blades in order to achieve optimum power output;
- limit the power capture in high wind speeds and maintain operation until cut-off in low wind speeds;
- protect turbine electrical and mechanical components from damage caused by transient overshooting in grid fault conditions;
- provide grid voltage support by reactive power injection in grid fault conditions.

As will be discussed in the next section, a rotor position sensor plays a vital role in the control system of a variable-speed wind turbine. Using a sensor implies several drawbacks such as the cost and reliability. Recently it tends to eliminate the mechanical position sensor and implement estimation methods in the control system, which is the "Sensorless Control". The challenge is to design an accurate and reliable estimator to achieve comparable performance for the controller without a mechanical position sensor.

Despite the advancements in wind turbine technologies, grid integration has always been a significant concern, because it is not as easy as "plug and play". Without proper designs of grid connection interfaces and control strategies, renewable energy generation units, such as wind turbines in large wind farms, would not operate properly during grid disturbances. Moreover, power system reliability might be compromised due to the integration of geographically

distributed renewable energy sources that suffer from limitations such as low energy density and intermittent power production.

Traditionally wind turbines are considered as distribution generation. They are not required to contribute to power system voltage and frequency control during grid disturbances and should be disconnected in such conditions. As the result of substantial scaling up of individual wind turbines and wind farms, the wind power penetration in today's power systems has increased dramatically. More and more conventional power plants like coal, gas, and steam turbines have been replaced by wind turbines. Disconnection of large wind farms in grid fault conditions is likely to cause cascaded grid voltage collapse and even blackout in today's power system. Therefore, power system operators in many countries have revised their grid connection requirements for wind turbines and wind farms. Wind turbines must be able to ride-through certain transient voltage dips, i.e., wind turbines should stay connected during grid disturbances and resume operation as soon as the grid voltage is recovered. Wind turbines are also required to contribute to grid voltage recovery like traditional power plants.

The new grid connection codes pose serious challenges to wind turbine manufacturers. For current wind turbine technologies, especially the variable-speed concept, the turbine electrical components are vulnerable to grid disturbances, even for a small voltage dip. Transient overvoltages or overcurrents are likely to occur and damage the power electronic converters or other electric components. The mechanical components such as the drive train are also subject to increased stress during grid disturbances. Some protection schemes have been proposed to prevent wind turbines from damage and enhance the fault ride-through capability. However, as will be discussed in the following context in the thesis, some types of variable-speed wind turbines still have difficulty in severe grid fault ride-through. This research will try to investigate the characteristics of wind turbines in grid fault conditions and improve the fault ride-through design.

While many problems in grid integration have been identified and remedial actions have been suggested, issues still remain that hinder the introduction of renewable energy sources as a major contributor to power systems. One major reason is the lack of a trustworthy validation

infrastructure for designing and testing grid interfaces on realistic systems of reasonable size and complexity. As a result, a comprehensive and accurate simulation tool or platform is strongly needed for the development and analysis of future renewable energy systems. Such comprehensive hi-fidelity studies can be conducted using hardware-software co-simulation, namely, Hardware-In-the-Loop (HIL) simulation. This research will try to respond to the above challenge by developing an integrated real-time simulation platform for wind turbine studies.

1.2 Research Overview

1.2.1 Motivation

1.2.1.1 Sensorless Control

Wind turbines are the core component in the wind energy conversion system (WECS) and have undergone a dramatic development during the last two decades using the latest technology improvement in power electronics, aerodynamics, and mechanical drive train design . A wind turbine is normally composed of following five components:

- mechanical system (turbine rotor, shafts, gearbox and generator rotor);
- generator and drive system (generator and power converters);
- pitch servo system;
- control system (wind turbine control system and generator control system);
- protection system of the wind turbine.

The block diagram of a generic wind turbine is shown in Figure 1.3. Notations are: v_w = wind speed; T_{mec} = mechanical torque; ω_{rot} = rotational speed of turbine rotor; ω_{gen} = rotational speed of generator rotor; θ_{gen} = generator rotor angle; T_e = electrical torque; P = active power; P_{ref} = active power reference; Q = reactive power; Q_{ref} = reactive power reference; U_s = stator voltage; I_s = stator current; I_r = rotor current; f_e = grid electrical frequency; U_r^{ref} = rotor voltage reference; U_{ref} = stator voltage reference; β = pitch angle; β_{ref} = pitch angle reference.

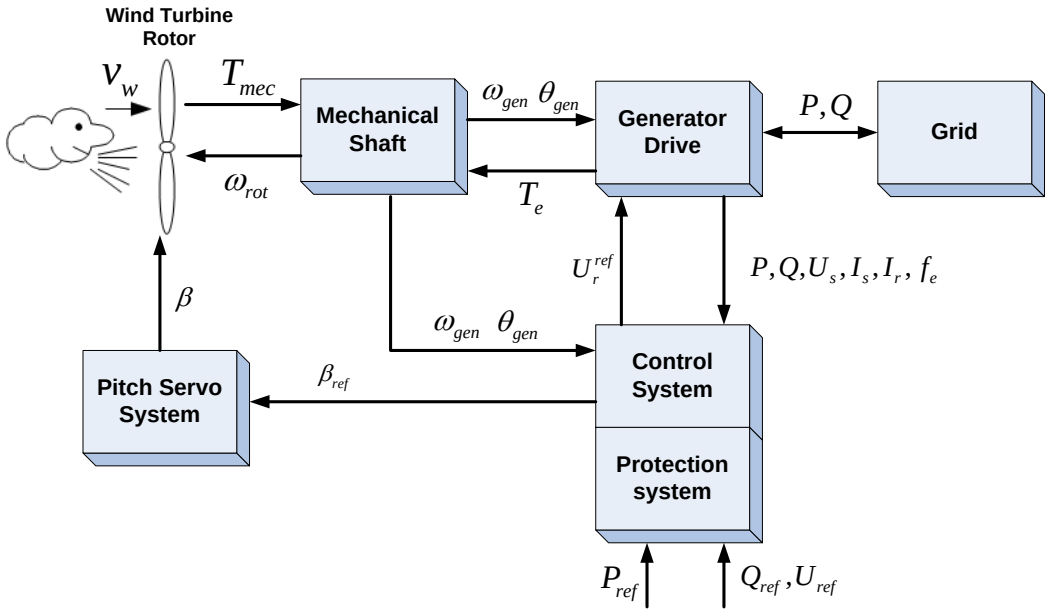

Figure 1.3 Variable-speed wind turbine system diagram.

Wind turbines can operate with either a fixed speed or a variable speed. Most of early installed wind turbines operate at fixed speed. They are designed to capture maximum wind energy and achieve maximum efficiency at only one particular wind speed. Although they have advantages of simple and robust structure, they have more serious drawbacks in terms of mechanical stress and limited power quality control. For example, fluctuations of winds are transmitted as fluctuations in the mechanical torque and then in the electrical power injected into grid, which might lead to voltage fluctuations and collapse.

Among recently installed wind turbines, variable speed wind turbines are the dominant type. They are designed to capture maximum wind energy and achieve maximum efficiency over a wide range of wind speeds. This is done by continuously adjusting the rotational speed of the wind turbine according to wind speeds and keeping the tip speed ratio constant at a value that corresponds to the maximum mechanical power capture. Another advantage is that fluctuations of winds are absorbed by changes in the generator speed, thus relieving the mechanical stress.

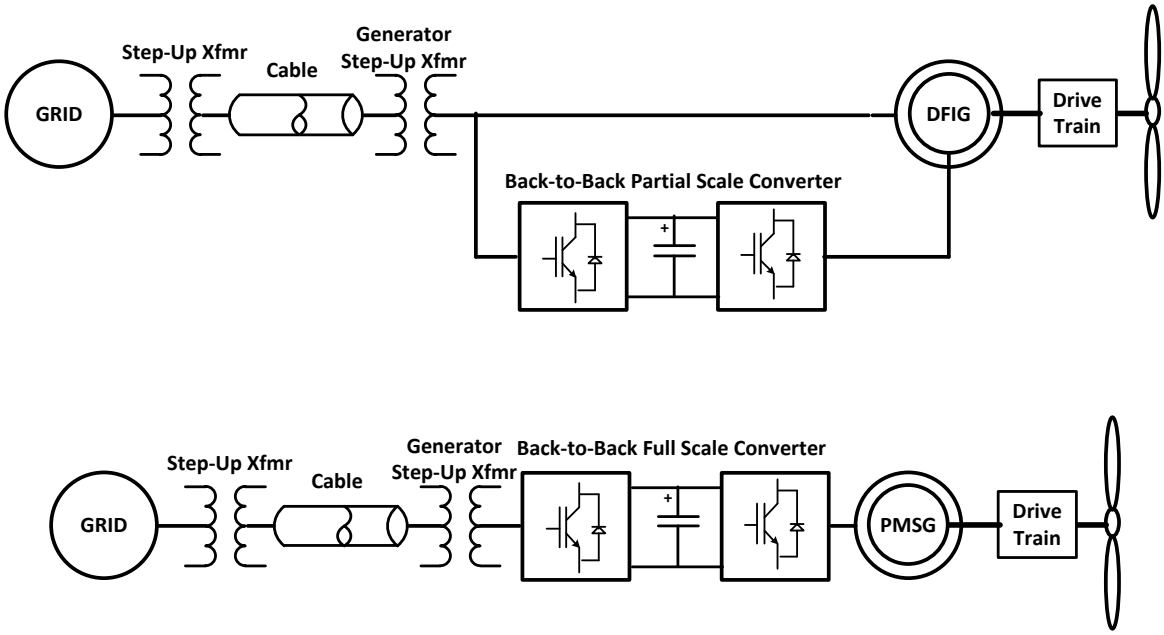

Figure 1.4 Variable-speed wind turbine system equipped with DFIG (upper) and PMSG (lower).

Apparently, the generator and drive system plays an important role in the variable speed wind turbine. Both induction and synchronous generators can be equipped in the variable speed wind turbine and interfaced with grid through power converters. Most modern large-scale variable speed wind turbines are based on the doubly-fed induction generator (DFIG) and permanent magnet synchronous generator (PMSG) [3] [4]. In the DFIG configuration, the stator of a DFIG is directly connected to the grid and the rotor winding is connected to a partial scale back-to-back voltage source converter (VSC) which provides variable-frequency rotor voltage. The main advantage of this configuration is that the power converter has to handle just a fraction of the rated wind turbine power, typically around 30% of rated. However, in the PMSG configuration, the generator is connected to the grid via a full scale back-to-back VSC through a DC link. Two variable-speed wind turbine systems equipped with DFIG and PMSG are shown in Figure 1.4.

The block diagram of the control system in Figure 1.3 is expanded with more details as shown in Figure 1.5 using the DFIG configuration as an example. The overall control system has two hierarchical control levels that are related to each other with different bandwidths,

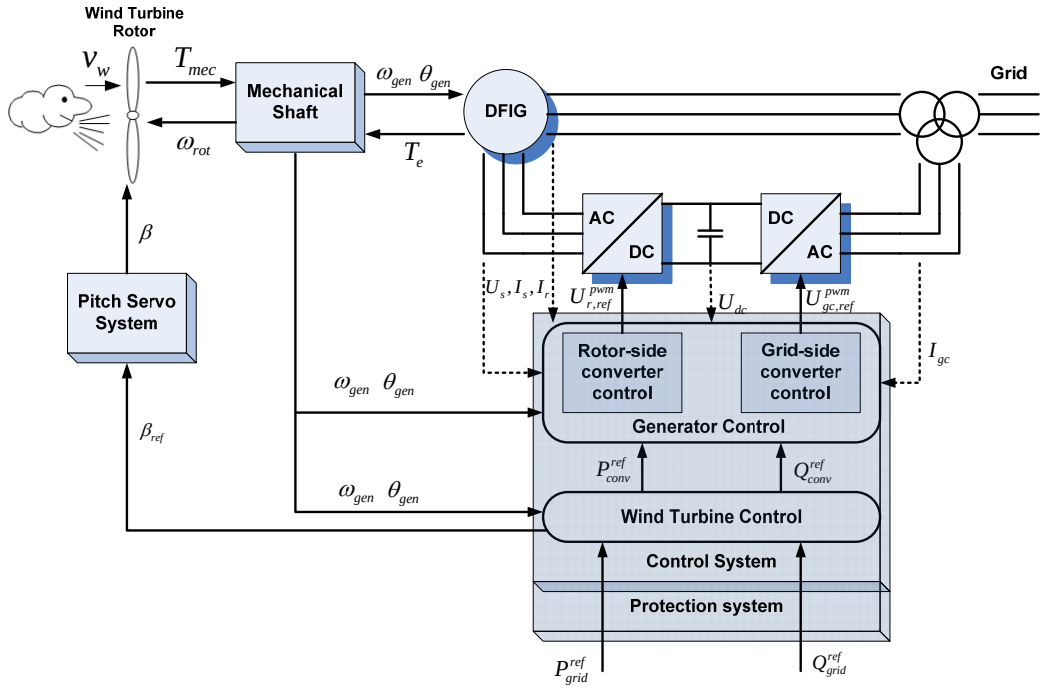

Figure 1.5 Variable-speed wind turbine equipped with a DFIG and its control system.

namely, generator control level and wind turbine control level. The generator control, with a fast dynamic response, contains the electrical control of the rotor-side power converter and the grid-side power converter. By injecting variable frequency voltages into the rotor via the rotor-side power converter using pulse-width modulation (PWM) technique, the active and reactive power at the stator side can be controlled independently. The grid-side power converter controller functions to maintain the DC voltage between two converters at a constant value and keep the reactive power at the grid side to zero. The wind turbine control, with slow dynamic response, supervises both the active and reactive power reference values of the generator control level as well as the pitch servo system of the wind turbine.

As mentioned in the previous section, a position sensor is used to implement the vector control strategy for wind turbine generators. Rotor position is directly obtained from the position sensor. It is used to transfer rotor variables from their natural reference frame to the stator-flux-oriented reference frame or the stator-voltage-oriented reference frame and reversely.

Furthermore, rotor angular speed is estimated using the position sensor by calculating the position difference in a small sampling period. Thus, position sensors play an important role in the vector controller. The performance of the system depends on the accuracy of the rotor position and speed information derived from the position sensor.

Recently, in the motor drive research community, research has concentrated on the elimination of the position sensor at the machine shaft without deteriorating the dynamics performance of the drive control system [5] [6] [7]. Vector controller without a position sensor is referred to as the "Sensorless Vector Control". The advantages of sensorless induction motor drives are reduced hardware complexity and lower cost, reduced size of the drive machine, elimination of the sensor cable, better noise immunity, increased reliability, and less maintenance requirements. Operation in hostile environments mostly requires a motor without position sensors. The DFIG is basically a wound rotor induction machine that shares most characteristics with the cage rotor induction machine in induction motor drives. However, the sensorless control for wind turbine generators has not yet drawn much attention as that for cage rotor induction machines. Therefore, the research question becomes:

Can an accurate electrical controller be implemented on the generator of a variable-speed wind turbine without using a mechanical position sensor?

Since DFIG-based variable speed wind turbines are widely used in wind energy conversion system, sensorless control of DFIGs has received increasing attention recently. The rotor current of DFIGs is available for measurement, which is not possible in cage rotor induction motors. This provides more flexibility in designing sensorless control schemes. However,only a limited number of research addressing sensorless control of doubly-fed induction machines is found in the literature [8]-[15]. Rotor position estimation approaches proposed in [8]-[12] are open-loop estimators, where the rotor position is directly synthesized from measured voltages and currents by reference frame transformation and rotor speed is obtained via differentiation. Observer dynamics and design guidelines were not discussed. Moreover, open-loop estimators are highly dependent on machine parameters and the accuracy of estimation is not guaranteed.

The earliest work [8] proposes a position sensorless scheme using only the rotor variables as the measured signals. It is actually a rotor flux-based estimator involving the integration of the rotor back electromotive force (back-EMF). Since the rotor slip frequency is very low around synchronous speed, this sensorless scheme gives poor performance for operation around synchronous speed. The sensorless control methods in [9]-[11] are based on open-loop rotor current estimators where the estimated current is compared to the measured current and the rotor position is derived using open-loop algebraic calculation. The rotor angular speed is therefore obtained via differentiation. For example, in [9], the commercial product ROTODRIVE is presented where a rotor current estimator is proposed using load active and reactive power. In [10], the rotor current in the stator-flux-oriented reference is estimated from the stator current in the stationary reference frame. In [11], the stator flux magnetizing current is used to derive the rotor position. Generally speaking, these open-loop estimators suffer from low accuracy due to machine parameter errors. None of them addresses the modeling and design method of the rotor position estimator. Moreover, obtaining the speed via differentiation of the rotor position may produce a noisy speed estimation[10].

Closed-loop MRAS observers have been proposed and studied in [13]-[15] based on the original work [16]. Four MRAS observers using different output variables for speed adaptation were analyzed and compared. The adaptive models therein are all based on static flux-current relations, and therefore, are very sensitive to machine inductances as shown in the parameter sensitivity analysis. Another drawback is that all MRAS observers are implemented in the stationary reference frame, where the electrical variables are sinusoidal functions of time in steady state. Hence, the observer might become inaccurate or even unstable in digital implementation as described in [17].

1.2.1.2 Fault Ride-Through

Variable-speed wind turbines equipped with DFIGs and PMSGs have different behavior in grid fault conditions [18]. Since the stator of the DFIG is directly connected to the grid, wind turbines equipped with the DFIG are very sensitive to grid disturbances. The severe

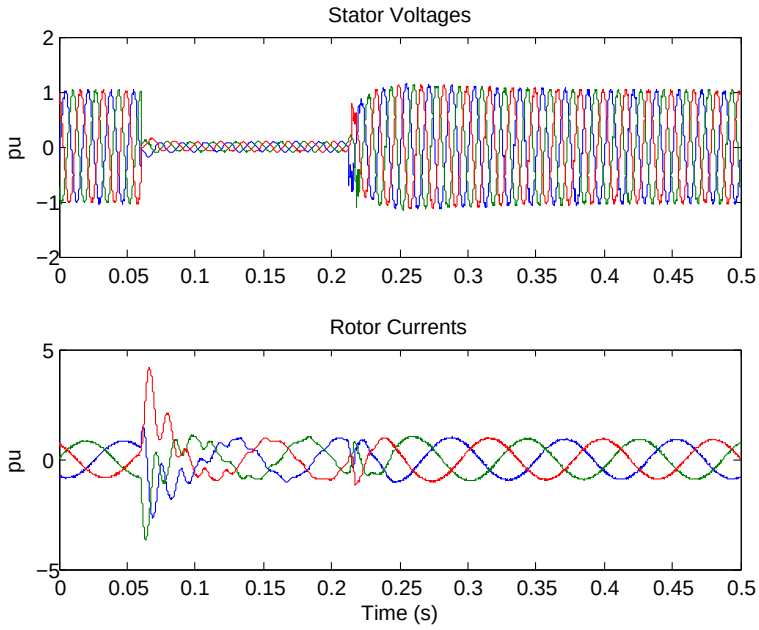

Figure 1.6 DFIG rotor currents during a grid three-phase short-circuit fault.

grid voltage dips may cause overvoltages and overcurrents in the rotor windings that could destroy the partial scale power electronic converter if no protection schemes are implemented. Figure 1.6 shows three-phase rotor winding currents of a DFIG-based wind turbine when a three-phase short-circuit fault occurs near the stator terminal. It can be seen that when the fault occurs transient rotor currents can increase as high as 4 pu that could easily destroy the rotor-side voltage source converter if no protection elements are included.

Before the new grid codes are exerted, wind turbine manufacturers usually connect an external circuit with anti-parallel thyristors and resistors, which is called "crowbar", to the rotor winding. The crowbar immediately disconnects the rotor-side converter from the rotor winding when a grid fault is detected. Therefore, the induced high transient rotor current will flow through the crowbar circuit instead of the converter, protecting the power electronic equipment from damage. However, this solution does not conform to the new grid codes which require wind turbines remain online under certain voltage dips. Moreover, tripping wind turbines by the crowbar may contribute to increase the grid voltage drop as no electric active and reactive powers are generated by the wind turbine.

Compared to the DFIG-based wind turbines, the PMSG-based wind turbines with a full-scale power converter inherently has better fault ride-through capabilities because it is decoupled from the grid by the DC-link capacitor. However, the DC-link capacitor is likely to be overcharged during grid disturbances and this will cause unacceptable overvoltages on the DC bus.

Therefore, the research question follows:

Can an effective fault ride-through strategy be implemented on variable-speed wind turbines to protect electrical and mechanical components with minimum hardware elements?

1.2.1.3 Real-Time Simulation

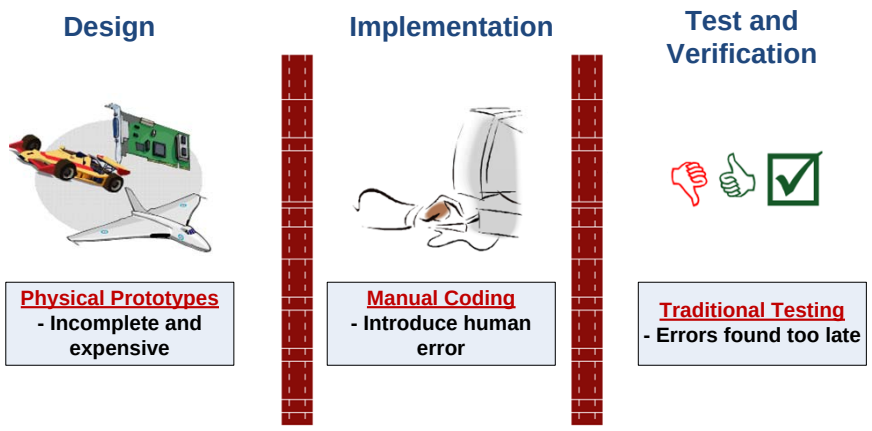

Figure 1.7 Traditional controller design flow.

Today, to design a controller for an increasingly complex system, i.e., the electric ship propulsion system, a systematic and efficient design flow should be relied on. In the traditional controller design flow shown in Figure 1.7, design takes place in the early stage of the process while test and implementation of the control systems has to wait until late in the process. Since the integration of hardware and software takes place so late in the development cycle, the discovery of errors are usually too late and ofter result in production delays, as well as additional expenses in verification tests. Control engineers today are addressing these

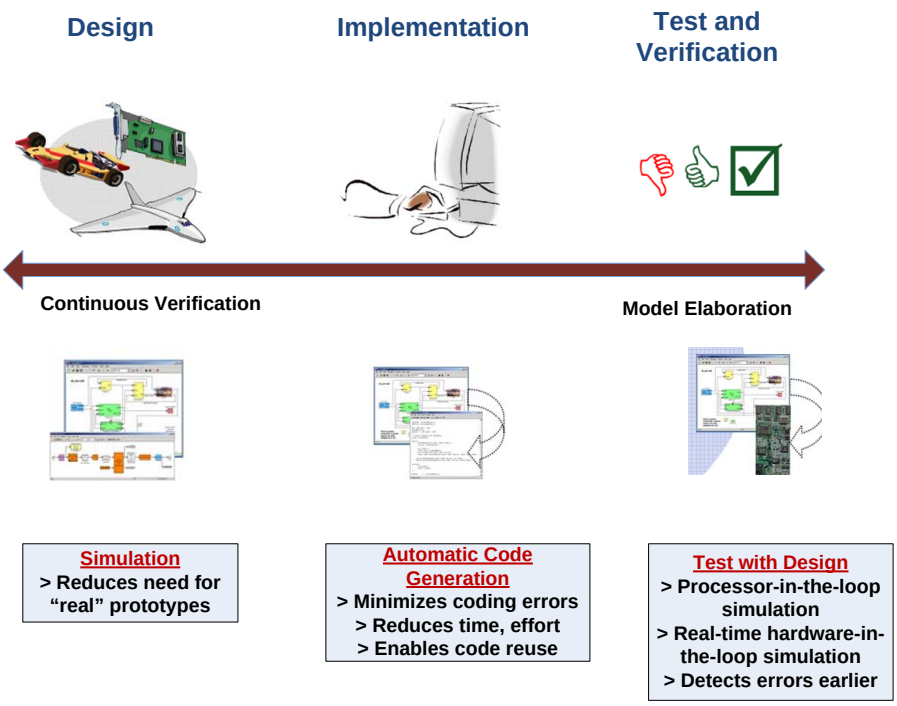

Figure 1.8 Model-based design flow.

challenges using a model-based design approach shown in Figure 1.8, with the help of a set of sophisticated software and hardware tools. For example, model-based design software, such as MATLAB/Simulink, and real-time hardware-in-the-loop simulation are used throughout the development process for system characterization, simulation, rapid prototyping, and testing. In this way, the implementation and test are moved earlier in the development cycle so that control engineers can discover problems early and save costs.

It is worth noting that the hardware-in-the-loop simulation has entered the model-based design flow and become the only way to bridge the gap between the offline software-only simulation and final system production [19]. In the traditional design flow, when the control algorithm has been developed and validated by software simulation, people usually try to implement the control algorithm on a controller and build an actual hardware experimental platform for testing. The advantages of using the hardware-in-the-loop simulation are summarized as follows:

- Software-only simulation is unable to replicate actual operation conditions.
- Final system construction is time-consuming, expensive, and error-prone if design errors and bugs are not discovered by Software-only simulation.
- Hardware-in-the-loop simulation reduces development time and avoids unnecessary losses resulting from any design errors and bugs because of the absence of a real plant.

The need for real-time simulation capabilities has been recognized for many years in the power electronics and power systems areas. Therefore, the research question is:

Can a real-time hardware-in-the-loop simulation platform be developed for variable-speed wind turbines for control system design and fault ride-through strategy investigation?

We propose to simulate a complete variable-speed wind turbine in the RTDS, and implement the control system on the dSAPCE real-time controller. Details of the simulation platform and implementation procedures are presented in the next chapter.

1.2.2 Objective

As discussed in the last section, this thesis investigates the control and protection of variable-speed wind turbines and develops a real-time simulation platform for validation.

The main objectives of this research are summarized below:

- Develop accurate and robust sensorless controllers for DFIG-based variable-speed wind turbines;
- Investigate the dynamic behavior of DFIG- and PMSG-based variable-speed wind turbines during grid disturbances;
- Develop measures for fault ride-through of DFIG- and PMSG-based variable-speed wind turbines with minimum hardware elements;
- Develop a real-time simulation platform for studies of variable-speed wind turbines.

The first objective is to design a sensorless controller for variable-speed wind turbines. A state observer will be used to estimate rotor speed and position. Since the estimated rotor speeds and positions are critical information for the electrical controller, the stability and accuracy of estimated variables are of utmost importance. Therefore, the stability condition of the observer, as well as the relation between observer dynamics and observer parameter selections, will be investigated. The goal is to propose a set of explicit design guidelines to ensure observer stability and obtain desired dynamics. Moreover, since the observer uses the plant model for estimations, the sensitivity against plant model parameter variations will be analyzed and compared with existing speed estimators.

The second objective is to investigate the dynamic behavior of variable-speed wind turbines and propose fault ride-through solutions to mitigate the negative consequences. It is desired that the minimum hardware element is included in the fault ride-through solution because it increases the system cost and complexity. Considering the fact that the power electronic converter in DFIG-based wind turbines has limited rating and therefore limited ride-through capability, it is proposed to apply a combined approach that consists of hardware and software components to ride-through the grid fault. For PMSG-based wind turbines, a software-only ride-through approach is proposed.

The third objective is to apply the developed models and controller on a real-time simulation platform using the model-based design approach. The model-based design approach has been very successful in controller design and verification in aerospace and automobile industry. In this research, the model-based design approach will be applied to the entire process of the development of the sensorless controller and the fault ride-through controller for variable-speed wind turbines. The entire wind turbine system will be implemented on a state-of-the-art integrated real-time hardware-in-the-loop simulation environment. The integrated simulation environment will be developed based on RTDS^{TM}and dSPACE^{TM}, which are industry standard simulators. In this way, various implementation constraints can be taken into account and examined before a entire system is build in the laboratory. Moreover, fault conditions can easily be generated and fault ride-through solutions can be tested in various conditions.

1.2.3 Thesis Outline

The structure of this thesis reflects the research objectives discussed above. The integrated real-time simulation platform setup is described and the implementation details are addressed in Chapter Two. Real-time simulation results are organized and presented in the corresponding chapters followed. In Chapter Three, the DFIG model and sensorless vector control are introduced. The proposed speed-adaptive reduced-order observer is analyzed in all aspects, including the structure, closed-loop observer model, observer gain design, and parameter sensitivity analysis. In Chapter Four, modeling details of the PMSG-based VSWT, including wind aerodynamics, the electrical and mechanical components, and the electrical and mechanical controllers are introduced. The digital implementation of the overall model in RTDS and dSPACE environment will also be addressed. Chapter Five presents the fault ride-through analysis and proposed solutions for both types of variable-speed wind turbines. Chapter Six concludes this thesis with the summary of contributions and suggestions for future work.

CHAPTER 2. A NEW REAL-TIME SIMULATION PLATFORM

2.1 State of The Art

With the ever evolving complexity of power and power electronics systems, their wide use in all aspects of todays industrial, residential, and military installations, and with increased pressure for reduced time-to-market and costs, the need for extensive real-time simulation is inevitable. Todays power electronic devices and controllers are often interfacing with small- or large-scale power systems for power conversion and regulation in various applications, such as renewable energy systems and naval electric ships. There is a need for rigorous and thorough performance evaluation of a digital controller and its corresponding power electronic device within the context of the host power system before commissioning. There is also a need for a critical investigation of the dynamic behavior of electric power systems with high penetration of wind power using physical components, so that the reality can be emulated in a laboratory as close as possible. There are generally two approaches to address this need.

The common approach is based on off-line transient digital simulation with the help of a set of software tools, e.g., PSCAD/EMTDC, MATLAB/SIMULINK, DIgSILENT/PowerFactory, or the Virtual Test Bed. These tools are capable of representing power electronic devices and electric power systems, as well as control logics and algorithms for digital controllers. However, off-line simulation studies are not able to reproduce the run-time behavior of digital controllers and real-time events in electric power systems. Therefore, potential design bugs in the real-time environment cannot be discovered, and the complete evaluation and testing of digital controllers is a formidable task.

An alternate approach is using an hardware-in-the-loop configuration, in which real-time simulation based on mathematical models replaces part of the real systems or components,

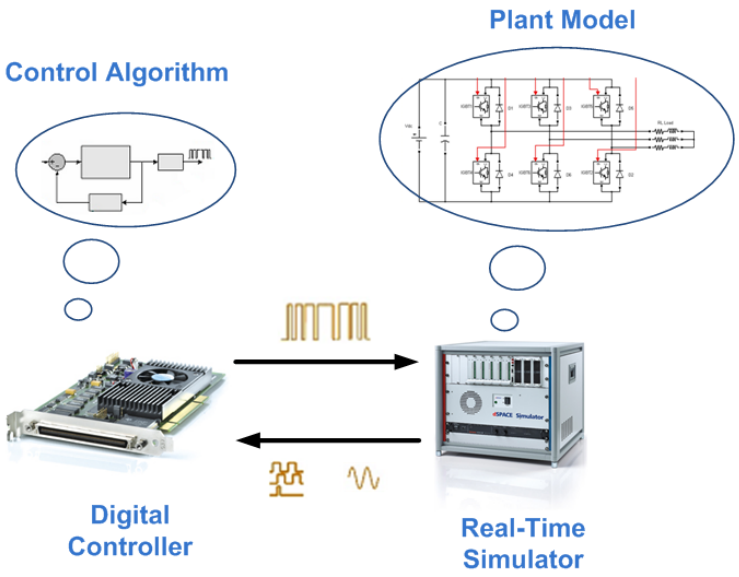

Figure 2.1 Concept of real-time hardware-in-the-loop simulation.

and interacts with real hardware. This concept is shown in Figure 2.1. In this way, such comprehensive hi-fidelity studies can be conducted using the real-time hardware-in-the-loop simulation.

The real physical hardware under test of an hardware-in-the-loop simulation is a digital controller that interacts with the simulated electrical system, i.e., power system and/or power electronic components. This is called signal-level simulation because only low-power control signals are exchanged between the hardware and the simulator. These signals are usually within the range of ± 10 V and $0 - 100$ mA. Since the control algorithm is developed and implemented on real hardware, non-ideal phenomena such as discreteness, nonlinearities, truncation error, execution time, and communication delay are taken into consideration in the hardware-in-the-loop simulation. Potential design errors could be revealed in an early stage, and system performance can be optimized for real conditions. The hardware-in-the-loop simulation is often employed in aerospace and automotive applications for assessment of controller hardware. Recently this concept has also been employed by the power electronics and electric drives community [20] [21]. However, the hardware-in-the-loop simulation has not been widely used on the wind energy conversion system.

The hardware-in-the-loop concept and technologies have been employed to design and test control system in the past two decades. In [20], the hardware-in-the-loop test for a rail vehicle control system is achieved by connecting the physical vehicle control system to a real-time vehicle simulator in closed-loop operation. The real-time simulator is built based on several old dSPACE processors and interface boards. The locomotive model is distributed over several processors resulting a sampling time of 30 μs. Reference [22] presents a PC-based tool for real-time controller testing and rapid controller prototyping. The real-time PC-based simulator is a PC-cluster consisting of several target PCs with different processing speeds. FireWire (IEEE 1394) communication links between target PCs enable parallel simulation of models with step sizes down to 20 μs. Reference [23] presents a controller rapid prototyping tool using both the virtual test bed (VTB) and dSPACE. The VTB used here as the system simulator is a non-real-time platform. Reference [24] demonstrates how a real-time simulated motor drive based on the HyperSim simulator can be interfaced to a real drive controller (Motorolla MC68332 microcontroller) for designing and testing. The switching frequency of the PWM voltage source inverter used in the real-time simulation is close to 4 kHz.

The Real-Time Digital Simulator (RTDS) has been chosen as the real-time simulator for the real-time hardware-in-the-loop simulation in power system and power electronics areas. In reference [25], the plant consisting of the utility grid, microgrid and interfacing inverters, is simulated in the RTDS. A external dSPACE controller is used for implementation of the proposed controller. In [26], a wind turbine model is implemented in RTDS that is interfaced with actual external hardware, while dSPACE is used to provide wind velocity profiles for testing. Reference [21] studies a stochastic-based FPGA controller for an induction motor drive. The complete induction motor drive is simulated in RTDS and the controller is implemented in a Xilinx FPGA development board. With help of the RTDS Gigahertz Processing Card (GPC), the frequency of PWM signals can reach up t0 50 kHz. The integrated real-time simulation environment with RTDS and dSPACE was proposed in [27] and [28]. In [27], the environment is used to study grid impacts of distributed generation and simulation results are interpreted from the power systems point of view. Reference [28] studied a permanent magnet synchronous

generator-based wind turbine and grid interaction using this environment. However, not only the controller but also the wind turbine model are implemented in dSPACE, resulting limited calculation power of the dSPACE.

In this research, a novel integrated simulation platform based on industry standard simulation tools, RTDS and dSPACE, is proposed. Unlike the work presented in [27] and [28], the proposed platform emulates the actual physical interface where firing pulses and measurements are transmitted between the power electronic converter and its digital controller as in the real wind turbine control system. The simulation time-step of the overall power system and wind turbine models and the controller is 50 μs, while that of the voltage source converter is less than 2 μs [29].

2.2 System Setup

The RTDS is a fully digital electromagnetic transient power system simulator that operates in real time. In other words, power system simulation results produced by RTDS represent the realistic conditions in the real power network. This is achieved by its high-speed Gigahertz Processing Cards (GPCs) solving network and component model equations in a very short period of time. Moreover, the RTDS has a number of high-speed analog/digital input/output ports that can be conveniently interfaced with external instrumentation, such as controller units and protective relays. This makes it an ideal tool in power system industry for design and testing of power system control schemes and protection equipment. The newly introduced Gigahertz Processor Card (GPC) and Giga-Transceiver Input/Output (GTIO) Card in RTDS allow the gating signals to be read in a very small time step ($< 2\mu s$) and provide small time step ($< 2\mu s$) simulations of power converters [29]. The clock rate of the slave controller in the dSPACE board is 20 MHz, allowing high-frequency PWM signals to be generated.

The dSPACE system is a collection of software and hardware tools for model-based industrial control design. The dSPACE DS1103 system used in this research includes a 1-GHz PowerPC controller board and the Real-Time Interface (RTI) software. RTI enables rapid prototyping of the control scheme developed in Matlab/Simulink environment by converting it

into machine codes that can be executed on the PowerPC processor. Again, rich input/output ports are provided on the controller board for interfacing with equipment being controlled.

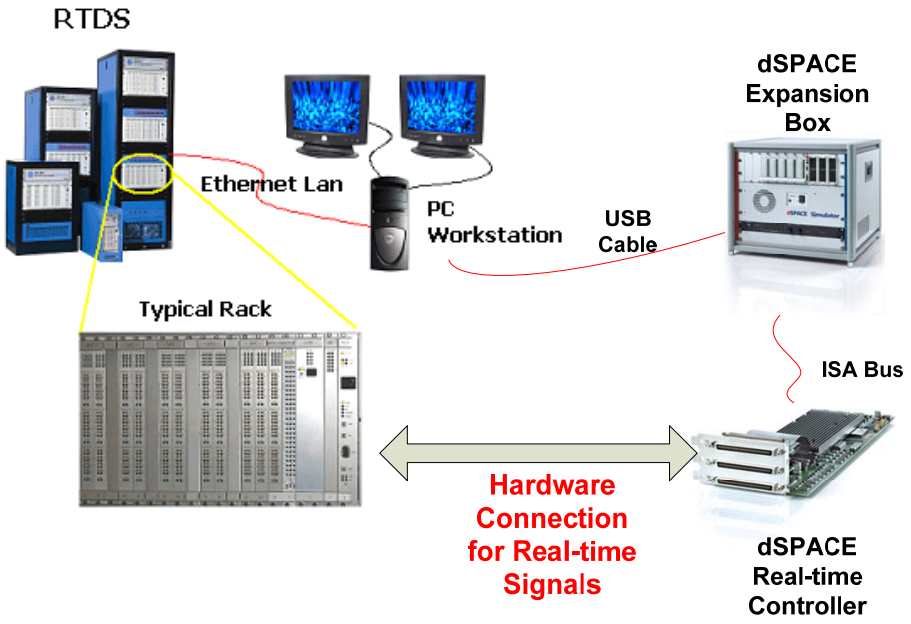

Figure 2.2 Overview of real-time hardware-in-the-loop simulation setup.

The overview of the hardware connection between RTDS and dSAPCE is illustrated in Figure 2.2. The connection diagram is shown in Figure 2.3. Figure 2.4 shows the detail wiring diagram between these two simulators. In RTDS-side, electrical input/output signals are passed through Giga-Transceiver Analog Output (GTAO), Giga-Transceiver Analog Input (GTAI), and Giga-Transceiver Digital Input (GTDI) cards. Eleven measurement signals in analog format including the instantaneous AC voltages, AC currents, the DC voltage, the machine rotor speed and angle are sent out via the GTAO card. In dSPACE-side, these measurements are read into analog-digital channels for signal processing and then passed to the controller. Among the control signals generated by the dSPACE controller, the pitch angle control signal in analog format is received by the GTAI card, while 12-bit firing pulses for the MSC and GSC are read by the GTDI card. The GTDI card allows the firing pulses to be read in a very small time-step ($< 2\mu s$). Considering the typical PWM frequency for MW-size power electronic converters is 1-5 kHz, the firing pulses appeared on the GTDI card terminals

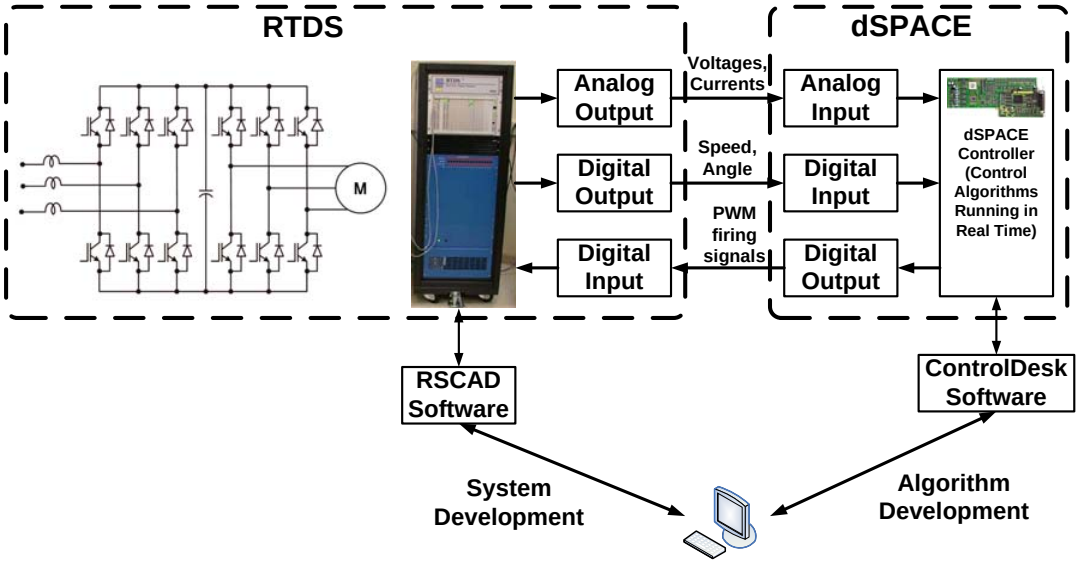

Figure 2.3 Connection diagram of real-time hardware-in-the-loop simulation.

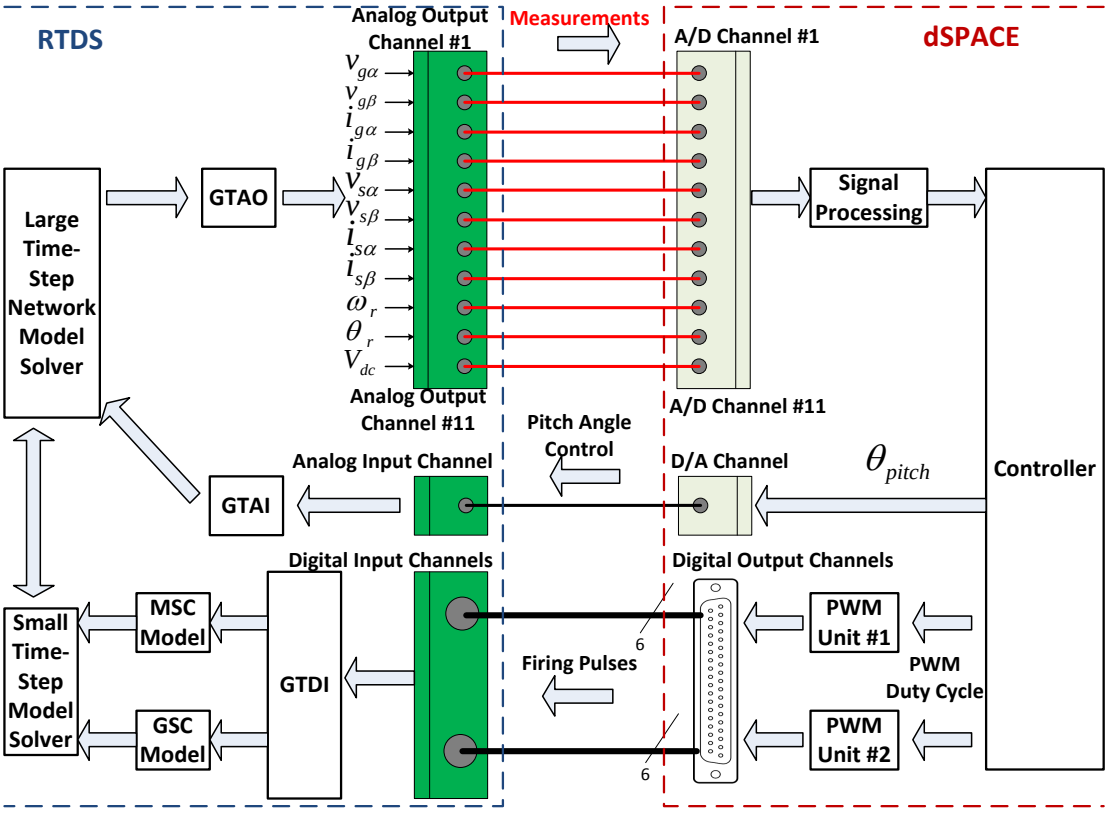

Figure 2.4 Detail wiring diagram of real-time hardware-in-the-loop simulation.

can be accurately represented in the RTDS simulation.

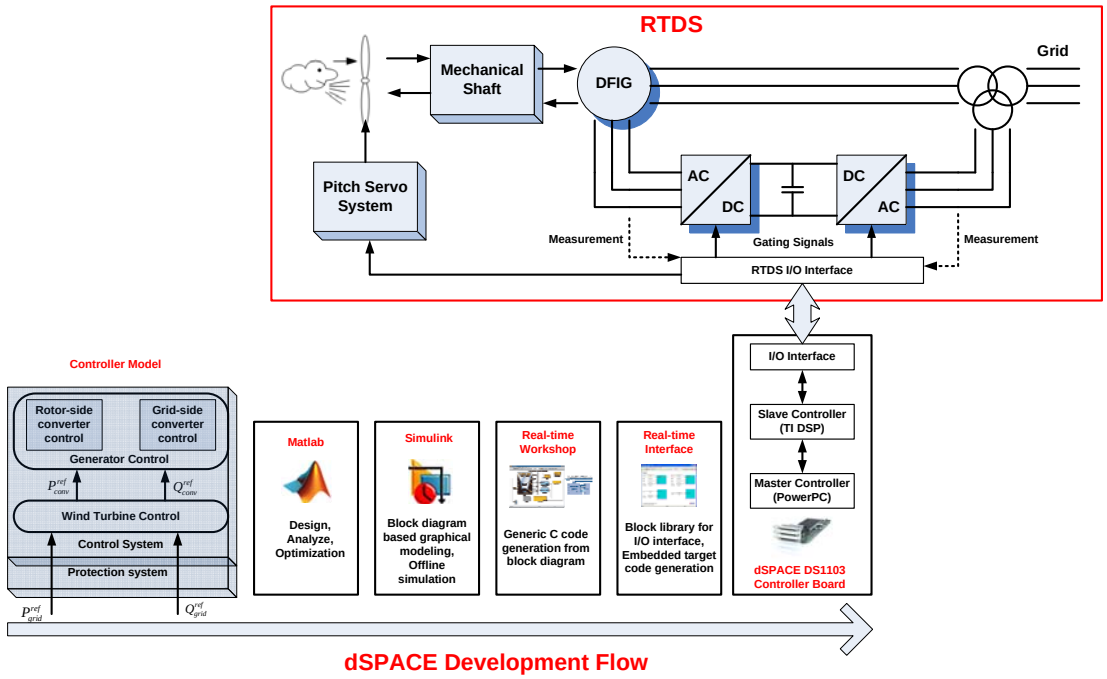

Figure 2.5 Real-time hardware-in-the-loop simulation of a DFIG-based wind turbine.

The general setup and implementation scheme for a DFIG-based variable-speed wind turbine on the proposed real-time simulation platform is shown in Figure 2.5. A complete DFIG-based variable speed wind turbine model and a simplified system model including the transmission line and the equivalent system are simulated in RTDS. The scaled voltage, current, speed, and angle signals of the simulated DFIG are generated by the RTDS and sent to the dSPACE controller board through the RTDS's GTAO card. On the dSPACE controller board, the received analog signals are digitized by on-board analog-to-digital converters (ADCs) and processed by the master controller. The command PWM gating signals are then generated by the slave controller and sent back to the simulated power converters in RTDS, completing a cycle of the real-time simulation.

The general setup and implementation scheme for a PMSG-based variable-speed wind turbine on the proposed real-time simulation platform is shown in Figure 2.6. In our opinion, the RTDS is better for power system network simulation as well as small time-step power electronic

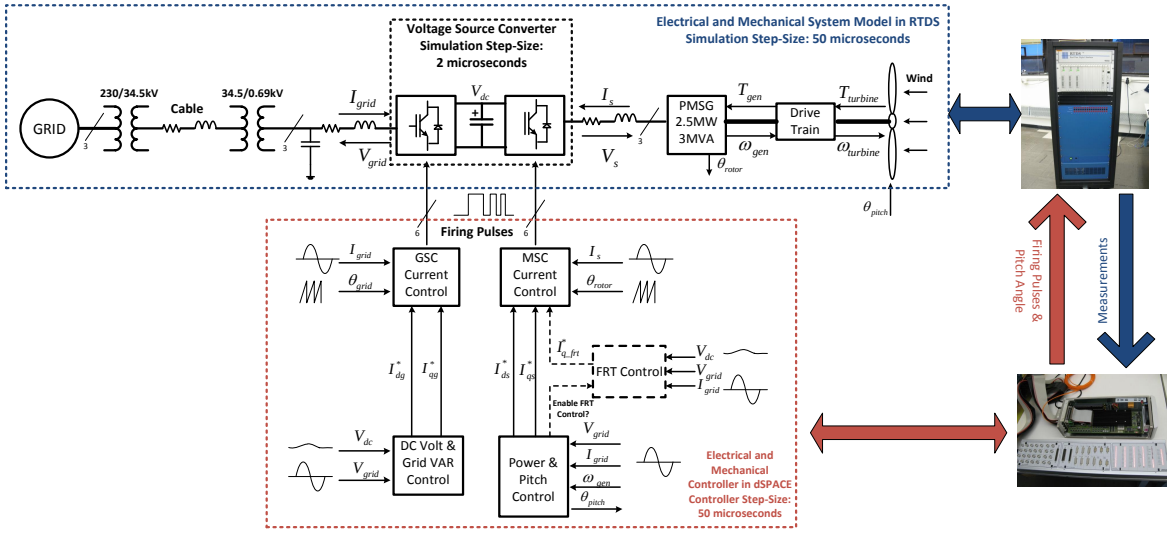

Figure 2.6 Real-time hardware-in-the-loop simulation of a PMSG-based wind turbine.

converter simulation, while the dSPACE DS1103 system is more suitable for controller design and implementation. Therefore, the overall electrical and mechanical PMSG-based VSWT model is executed on RTDS, whereas its controller is implemented on dSPACE. In this way, the utilization of computation power of both simulators is maximized. Moreover, the actual physical interface between the controller and equipment being controlled can be exercised for realistic testing results.

The dSPACE DS1103 controller has ten PWM output channels, among which six channels (PWM1-PWM6) can be used to drive a three-phase 2-level converter bridge model in RTDS. The rest four (PWM7-PWM10) are single-phase PWM output channels. This poses a problem in this study where a total number of twelve IGBTs in a back-to-back voltage source converter need to be controlled. An extra circuit including a "NOT" logic gate can be designed to solve this problem. However, a firing pulse conditioning module in RTDS can also be used for this purpose without extra hardware. As shown in Figure 2.7, three single-phase firing pulses generated from dSPACE are connected as a 6-bit firing word. The firing pulses conditioner then applies an "XOR" operation to the firing word and three additional PWM channels are created for IGBTs in the lower part of each converter leg. The conditioned firing pulses can

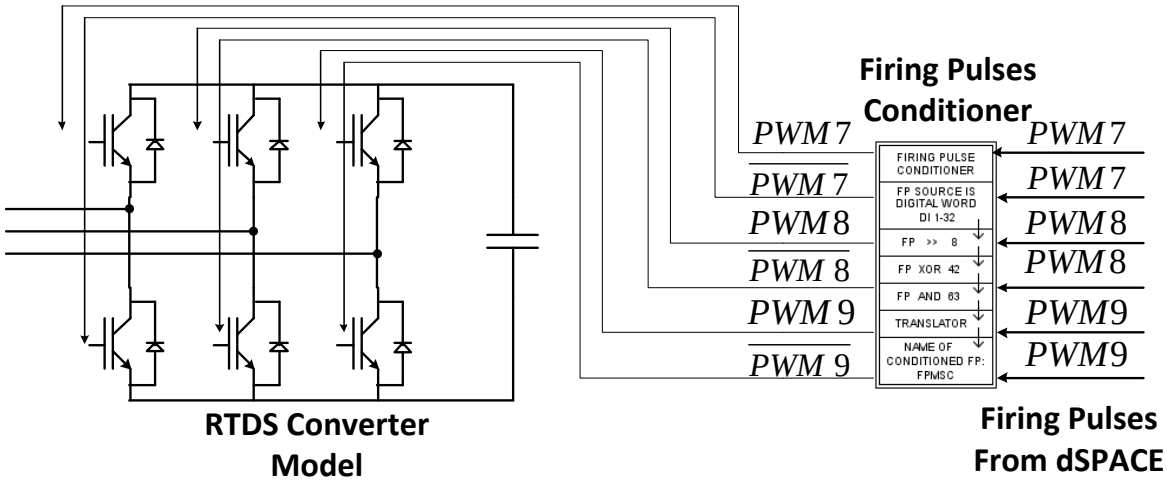

Figure 2.7 Firing pulse conditioner.

now be used to drive another three-phase 2-level converter bridge model.

2.3 Benchmark Testing

To validate the feasibility of the integrated real-time simulation platform and the modeling approach, a simplified case including only the model of a PMSG with reduced inertia, a power electronic inverter, and the controller was firstly developed in both the Matlab/Simulink environment and the real-time simulation platform. Both models use the same set of machine data and controller parameters. The model benchmark test results are shown in Figure 2.8 and Figure 2.9. In this test, the PMSG was operating as a motor. The electromagnet torque was maintained at 1 pu. The reference rotor speed was reduced to 0.8 pu at 0.5 sec and raised to 1.0 pu again at 3.0 sec. The steady-state and transient results show great agreement between the offline and real-time simulation models. The waveforms of firing pulses in a small period generated by Matlab/Simulink and the integrated real-time simulation platform are shown in Figure 2.10 and Figure 2.11, respectively. They are close to each other. It took the offline model on a 2.53-GHz computer more that 50 seconds to complete a 5-sec run. Note that the offline simulation model only contains a small part of components compared to the full PMSG-based VSWT model. In other words, the simulation time can be reduced at least ten

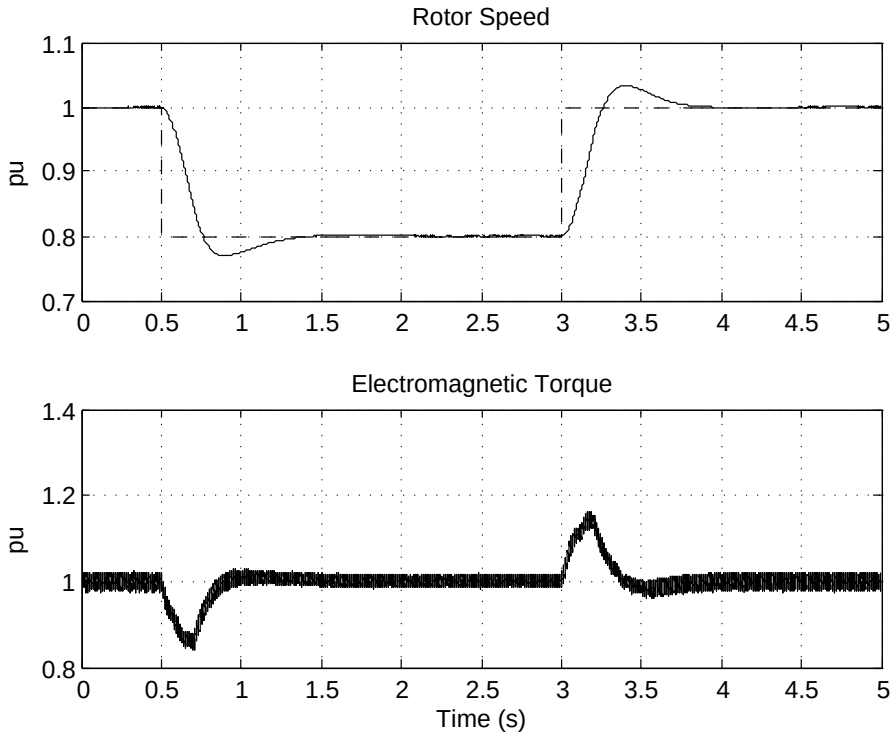

Figure 2.8 PMSG speed and torque in real-time simulation.

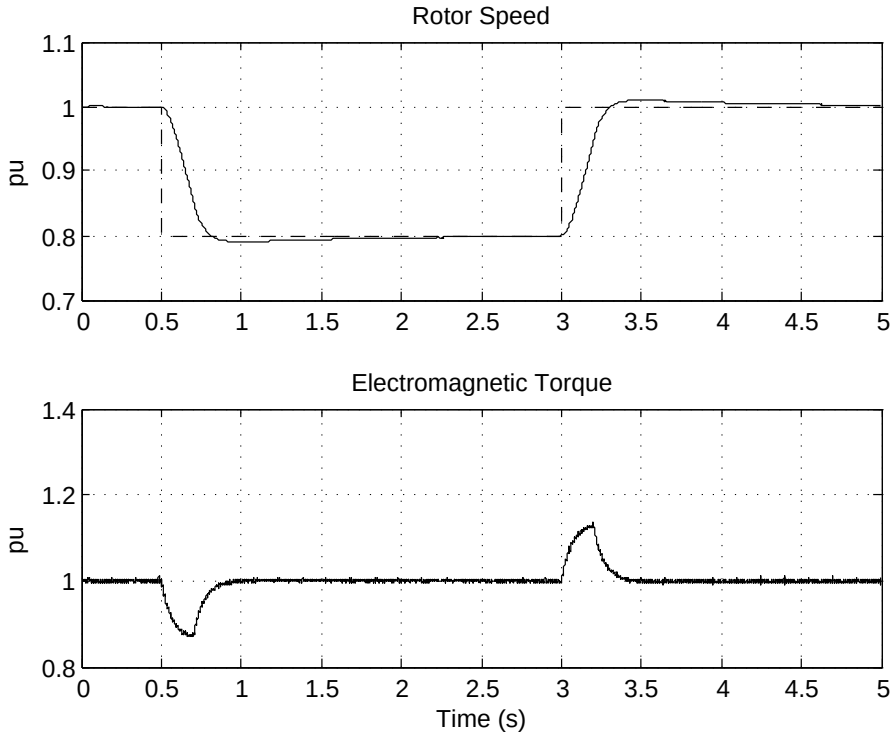

Figure 2.9 PMSG speed and torque in offline Simulink simulation.

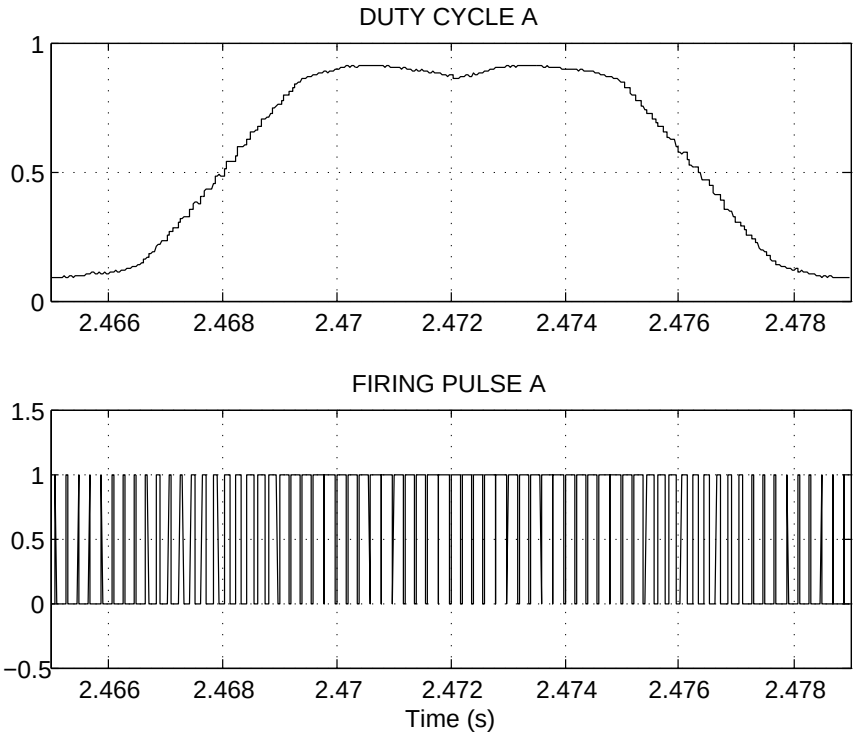

Figure 2.10 Duty cycle and firing pulse in offline Simulink simulation.

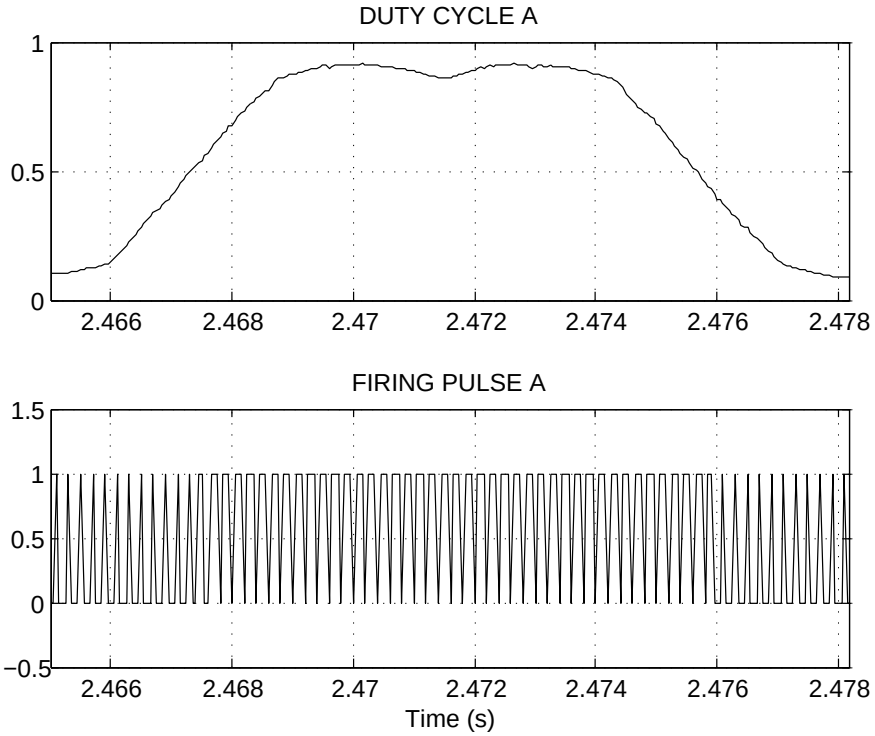

Figure 2.11 Duty cycle and firing pulse in real-time simulation.

times by the real-time simulation platform.

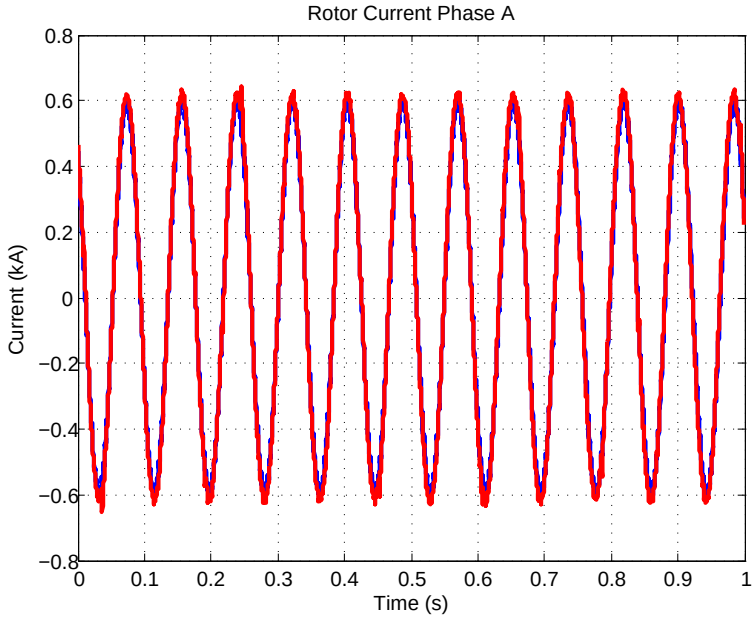

Figure 2.12 Rotor current of a 1.5-MW DFIG at the rated operating condition in offline simulation (blue) and real-time simulation (red).

Secondly, a complete DFIG-based 1.5-MW wind turbine model was developed in both the Matlab/Simulink environment and the real-time simulation platform for benchmark. The generator parameters at the rated operating condition and slow dynamic responses were compared. In the rated operating condition, the wind speed was 15 m/s and the rotor speed was regulated at 1.2 pu to get the rated electric power output (1.5 MW). It can be seen from Figure 2.12 to Figure 2.16 that the steady-state responses for the wind turbine model on these two simulation platforms are a good match. Next the wind speed was assumed to drop rapidly from 15 m/s to 12 m/s at t=0.5 second. Results are shown in Figure 2.17 to Figure 2.20. Due to the large inertia of the wind turbine, it takes around 10 seconds to reach another operating point. Although the model behavior in this slow dynamics is not a perfect match as in the steady-state, the overall error margin is less than 5 percent. However, the simulation speed is significantly reduced. It took Matlab/Simulink 450 seconds using the normal mode or 210 seconds using the accelerator mode compared with the real-time simulation completed in exactly 10 seconds.

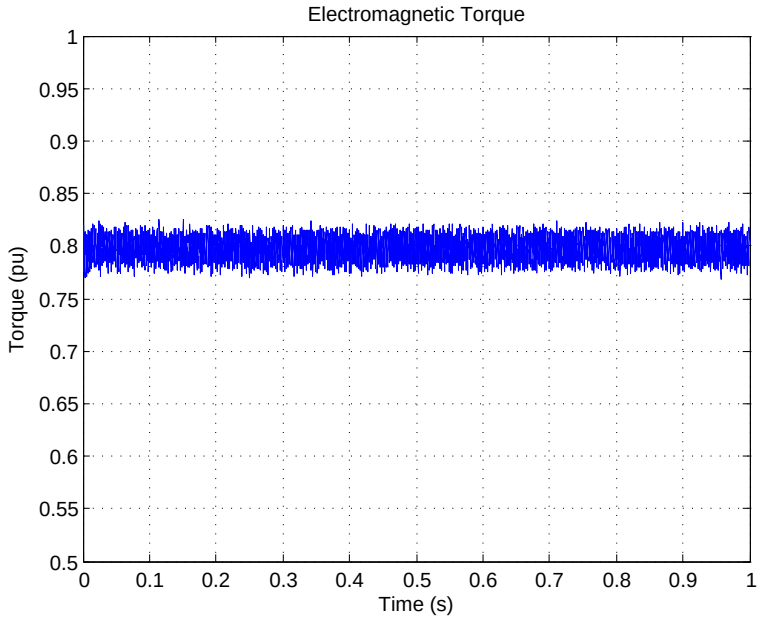

Figure 2.13 Electromagnetic torque of a 1.5-MW DFIG at the rated operating condition in offline simulation.

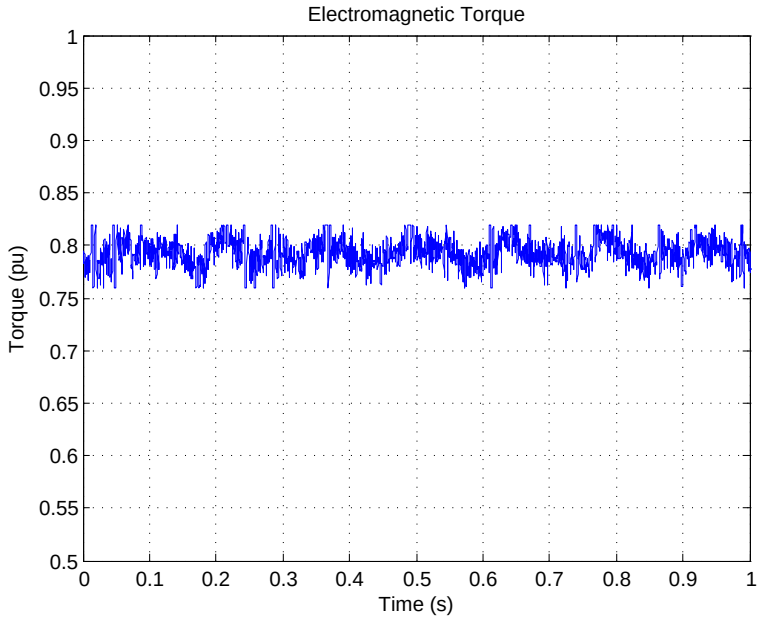

Figure 2.14 Electromagnetic torque of a 1.5-MW DFIG at the rated operating condition in real-time simulation.

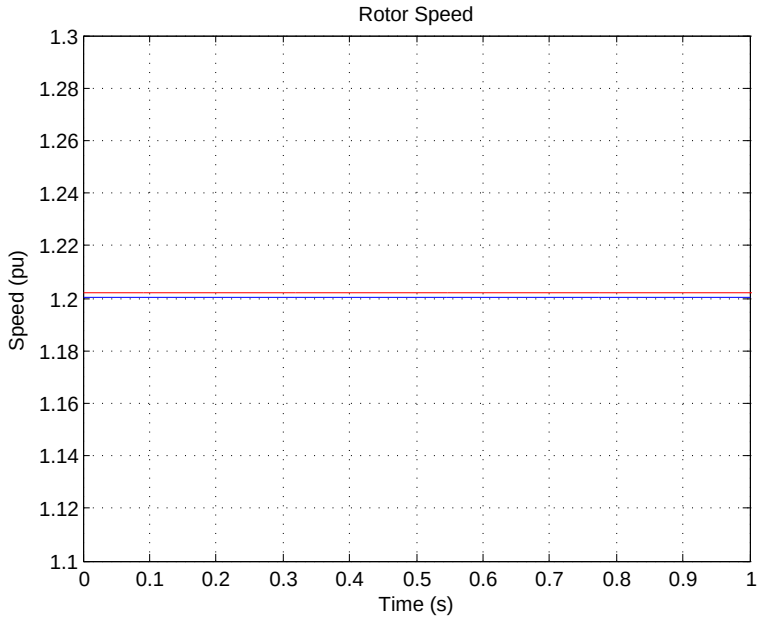

Figure 2.15 Rotor speed of a 1.5-MW DFIG at the rated operating condition in offline simulation (blue) and real-time simulation (red).

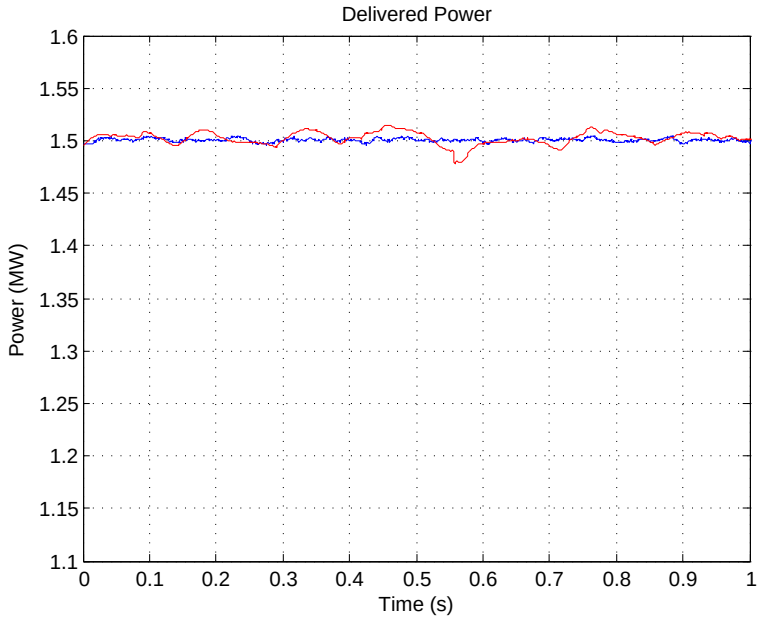

Figure 2.16 Electric power of a 1.5-MW DFIG at the rated operating condition in offline simulation (blue) and real-time simulation (red).

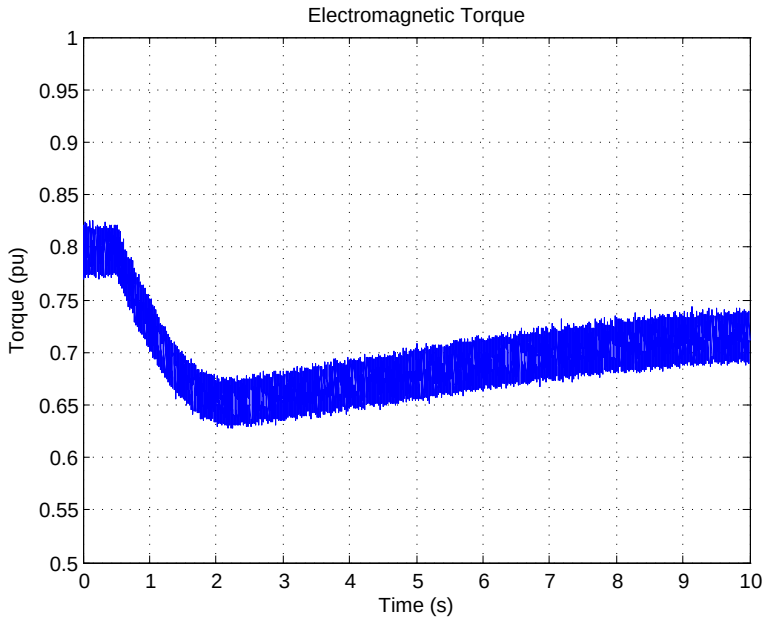

Figure 2.17 Electromagnetic torque of a 1.5-MW DFIG operating at wind speed dropping from 15 m/s to 12 m/s in offline simulation.

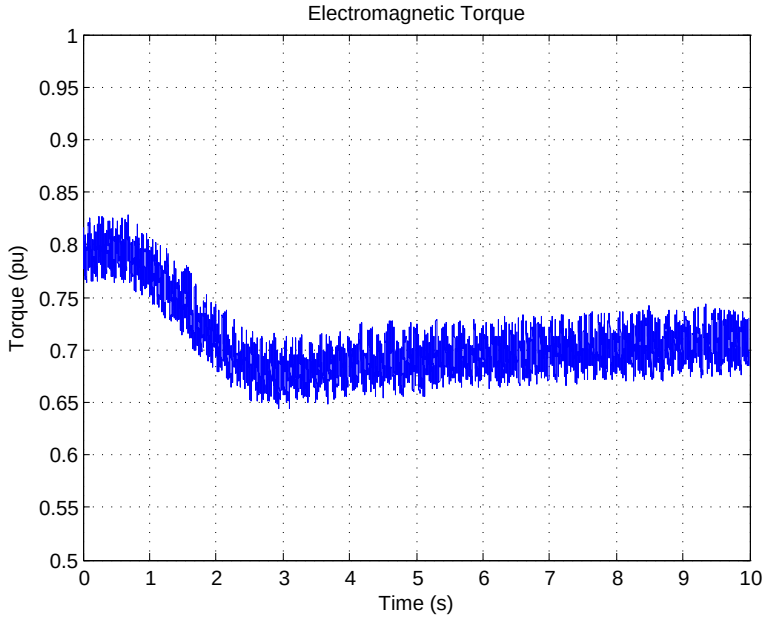

Figure 2.18 Electromagnetic torque of a 1.5-MW DFIG operating at wind speed dropping from 15 m/s to 12 m/s in real-time simulation.

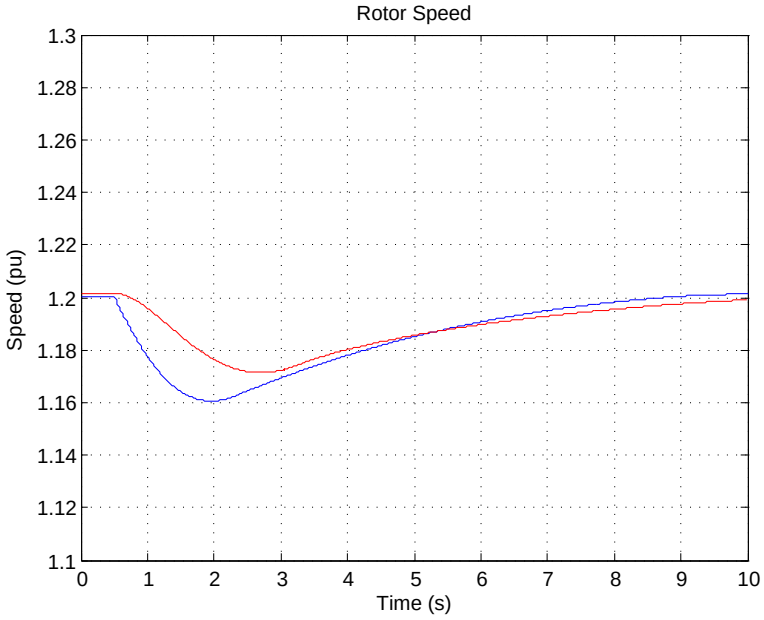

Figure 2.19 Rotor speed of a 1.5-MW DFIG operating at wind speed dropping from 15 m/s to 12 m/s in offline simulation (blue) and real-time simulation (red).

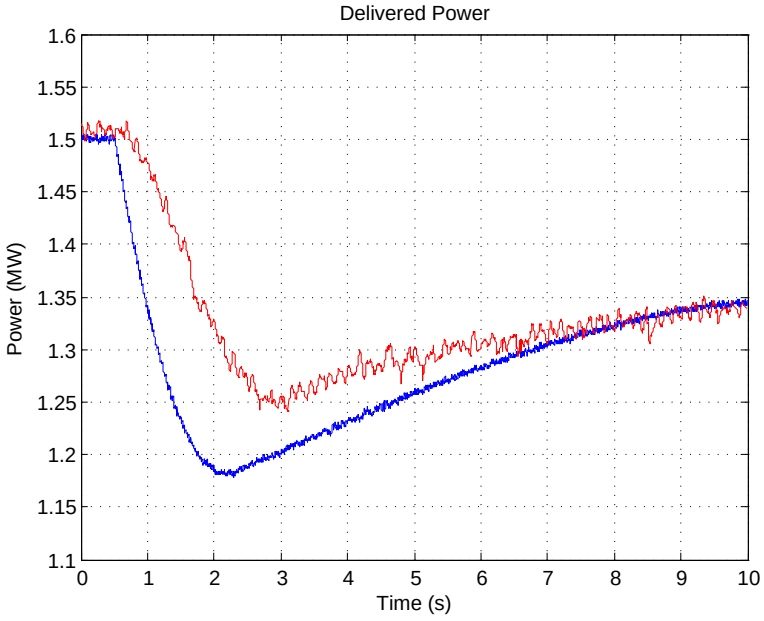

Figure 2.20 Electric power of a 1.5-MW DFIG operating at wind speed dropping from 15 m/s to 12 m/s in offline simulation (blue) and real-time simulation (red).

CHAPTER 3. NOVEL SENSORLESS CONTROL FOR DFIG-BASED WIND TURBINES

In this chapter, a speed-adaptive reduced-order observer for sensorless vector control of DFIG is proposed. The observer is a simulation of the rotor current dynamic model with feedback of the estimation error and a speed adaptation loop. Feedback and adaptation gains are designed based on the closed-loop observer model. A parameter sensitivity analysis reveals that this observer is robust against machine parameter variations in the normal operating regions. Simulation results demonstrate desired steady-state and dynamic performance of this sensorless control approach for DFIG-based variable speed wind turbines.

All model variables and machine parameters in this chapter are explained in Table 3.1.

Table 3.1 DFIG model variables

s, r	subscripts for stator and rotor variables
d, q	subscripts for variables in direct and quadrature axis
$\boldsymbol{v_s}, \boldsymbol{v_r}$	stator and rotor voltage space vectors
$\boldsymbol{i_s}, \boldsymbol{i_r}$	stator and rotor current space vectors
$\boldsymbol{\psi_s}, \boldsymbol{\psi_r}$	stator and rotor flux space vectors
R_s, R_r	stator and rotor resistance
L_s, L_r, L_m	stator, rotor and mutual inductance
σ	$= 1 - L_m^2/(L_s L_r)$, leakage coefficient
ρ	$= L_m^2/(\sigma L_s L_r)$
ω_a	arbitrary reference frame angular speed
ω_e	synchronous angular electrical speed
ω_s	stator angular electrical speed
ω_r	rotor angular electrical speed
ω_{sl}	$= \omega_s - \omega_r$, slip frequency
θ_r	rotor angular electrical angle
T_e, T_l	electromagnetic and load torque
n_p	number of pole pairs

3.1 Introduction

DFIG is very attractive for variable speed generation, especially for wind energy conversion systems (WECS), where it is driven by the wind turbine and its stator is directly connected to the grid. The rotor winding of the DFIG is connected to a back-to-back power converter which provides variable-frequency rotor voltage. Advantages of DFIG-based variable speed wind turbines are numerous [3]. Firstly, the maximal mechanical power attainable from the wind can be extracted and converted to fixed-frequency electric power by adjusting machine speed and electromagnetic torque. Secondly, only a fraction of the nominal electric power flows through the power converter, thus reducing its loss and cost. Moreover, stator side active and reactive power can be independently controlled.

The conventional control system of DFIGs is based on the stator-flux-oriented vector control [30]-[32]. The rotor current space vector is decomposed into two current components fixed to the synchronously rotating stator-flux-oriented reference frame using the rotor position information. Decoupled control of electromagnetic torque and flux is achieved in this way. Rotor position/speed sensors installed on the rotor shaft are required for the transformation of the rotor current space vector between different reference frames in the vector control system. Control of AC machines, especially cage rotor induction motors, without these shaft sensors has been an active research area in the last three decades [5]-[7] due to advantages of system robustness, easy installation and maintenance.

Since DFIG-based variable speed wind turbines are widely used in WECS today, sensorless control of DFIGs has received increasing attention recently [8]-[15]. The rotor current of DFIGs is available for measurement, which is not possible in cage rotor induction motors. This provides more flexibility in designing sensorless control schemes for DFIGs. Rotor position estimation approaches proposed in [8]-[12] are generally open-loop estimators, where the rotor position is directly synthesized from measured voltages and currents by reference frame transformation. The rotor speed is obtained via differentiation, which introduces noises into the speed estimation [10]. The analysis of estimator dynamics and design approaches were not addressed. Moreover, open-loop estimators are highly dependent on machine parameters and

the accuracy of estimation is not guaranteed. Closed-loop MRAS observers have been proposed and studied in [13]-[15] based on the original work in [16]. Four MRAS observers using different output variables for speed adaptation were analyzed and compared. The adaptive models therein are all based on static flux-current relations, and therefore, are very sensitive to the machine inductance as indicated in these references. Another drawback is that all MRAS observers are implemented in the stationary reference frame, where the electrical states are usually sinusoidal functions of time in steady state. Hence, it is difficult to design controller parameters and the observer might become inaccurate or even unstable in digital implementation [17].

In this research, a speed-adaptive reduced-order observer for sensorless vector control of DFIGs is proposed based on the original work in [33] and [34]. Instead of the full-order structure discussed in [33] and [34], the proposed observer only simulates a reduced-order model, which only consists of rotor current dynamics. Feedback of the rotor current estimation error and a speed adaptation loop are employed for speed and position estimation. The feedback gains and adaptation gains are designed to achieve desired bandwidth and stability margin based on the closed-loop observer dynamics. A parameter sensitivity analysis shows this observer is nearly independent on machine parameters in DFIG's normal operating regions.

3.2 DFIG Model

The DFIG can be modeled with the following voltage and flux equations in an arbitrary rotating reference frame similar to the cage rotor induction machine [35] [36] [37]:

$$\boldsymbol{v_s} = R_s \boldsymbol{i_s} + \frac{d\boldsymbol{\psi_s}}{dt} + j\omega_a \boldsymbol{\psi_s} \tag{3.1}$$

$$\boldsymbol{v_r} = R_r \boldsymbol{i_r} + \frac{d\boldsymbol{\psi_r}}{dt} + j(\omega_a - \omega_r)\boldsymbol{\psi_r} \tag{3.2}$$

$$\boldsymbol{\psi_s} = L_s \boldsymbol{i_s} + L_m \boldsymbol{i_r} \tag{3.3}$$

$$\boldsymbol{\psi_r} = L_r \boldsymbol{i_r} + L_m \boldsymbol{i_s} \tag{3.4}$$

The electromagnetic torque can be expressed using the following equation:

$$T_e = \frac{3}{2} n_p \frac{L_m}{\sigma L_s L_r} \mathrm{Im}\left\{\boldsymbol{\psi_s} \boldsymbol{\psi_r}^*\right\} \tag{3.5}$$

When the stator flux and rotor current are chosen as state variables, the state-space representation of the DFIG in an arbitrary rotating reference frame with the angular speed ω_a becomes

$$\dot{\mathbf{x}} = \mathbf{A}\mathbf{x} + \mathbf{B}\mathbf{u} \tag{3.6a}$$

$$\boldsymbol{i_r} = \mathbf{C}\mathbf{x} \tag{3.6b}$$

where

$$\mathbf{A} = \begin{bmatrix} -\frac{1}{\tau_s} - j\omega_a & \frac{L_m}{\tau_s} \\ \frac{\rho}{\tau_s L_m} + j\frac{\rho\omega_r}{L_m} & -\frac{\rho}{\tau_s} - \frac{1}{\sigma\tau_r} - j(\omega_a - \omega_r) \end{bmatrix} \tag{3.6c}$$

$$\mathbf{B} = \begin{bmatrix} 1 & 0 \\ -\frac{L_m}{\sigma L_s L_r} & \frac{1}{\sigma L_r} \end{bmatrix} \tag{3.6d}$$

$$\mathbf{C} = \begin{bmatrix} 0 & 1 \end{bmatrix}. \tag{3.6e}$$

3.3 Vector Control

This section provides a brief summary of the vector control system for DFIGs. Conventional DFIG control system is based on rotor current vector control in a synchronously rotating $d-q$ reference frame with the d-axis aligned along the stator flux. This permits decoupled control of electromagnetic torque and rotor excitation currents. Figure 3.1 shows the stator-flux-oriented reference frame [32]. In this figure, in addition to stator- and rotor-side natural reference frames, constituted by axes $D-Q$ and $\alpha-\beta$, respectively, the d direct axis is aligned with the stator flux-linkage space vector at any time. The stator-side natural reference frame remains stationary, while that corresponding to the rotor side rotates at ω_r electrical speed. The instantaneous angle between the stator-flux-oriented and the stationary reference frame is referred to as ρ_s. The instantaneous angle between the rotor-side natural reference frame and the stationary reference frame is denoted as θ_r.

In the stator-flux-oriented reference frame, considering that $\psi_{qs} = 0$ and $\omega_g = \omega_s$, the DFIG equations may be rewritten as follows:

$$|\boldsymbol{\psi_s}| = \psi_{ds} \Rightarrow L_m\,|\boldsymbol{i_{ms}}| = L_s i_{ds} + L_m i_{dr} \tag{3.7}$$

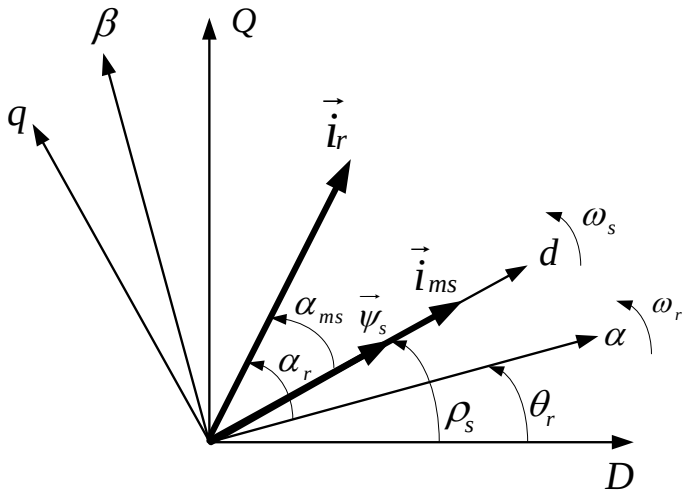

Figure 3.1 Stator-flux-oriented reference frame.

$$\psi_{dr} = L_r i_{dr} + L_m i_{ds} = \frac{L_m^2}{L_s} |\boldsymbol{i_{ms}}| + \sigma L_r i_{dr} \tag{3.8}$$

$$\psi_{qr} = L_r i_{qr} + L_m i_{qs} = \sigma L_r i_{qr} \tag{3.9}$$

$$v_{dr} = R_r i_{dr} + \sigma L_r \frac{d}{dt} i_{dr} - \omega_{sl} \sigma L_r i_{qr} \tag{3.10}$$

$$v_{qr} = R_r i_{qr} + \sigma L_r \frac{d}{dt} i_{qr} + \omega_{sl} \left(\frac{L_m^2}{L_s} |\boldsymbol{i_{ms}}| + \sigma L_r i_{dr} \right) \tag{3.11}$$

$$T_e = 1.5 n_p (\psi_{ds} i_{qs} - \psi_{qs} i_{ds}) = 1.5 n_p \frac{L_m^2}{L_s} |\boldsymbol{i_{ms}}| \, i_{qr} \tag{3.12}$$

where $|\boldsymbol{i_{ms}}|$ is stator magnetizing current space vector modulus. The overall structure of the vector control scheme, based on the aforementioned equations, is shown in Figure 3.2.

Vector control of the DFIGs has been extensively studied in previous literature [30]-[32]. In the stator-flux-oriented reference frame, the direct (d) axis component and quadrature (q) axis component of the rotor current vector $\boldsymbol{i_r}$ are i_{dr} and i_{qr}, which are directly related to the stator reactive power and active power, respectively. Thus, decoupled control of the the stator active and reactive power of a DFIG is achieved by controlling i_{qr} and i_{dr} to track desired reference values. To transform the rotor current vector between its natural reference frame rotating at the rotor angular speed ω_r and the stator-flux-oriented reference frame rotating at the synchronous speed ω_s, the knowledge of slip angle $\theta_{sl} = \theta_s - \theta_r$ where $\theta_s = \int \omega_s dt$ and

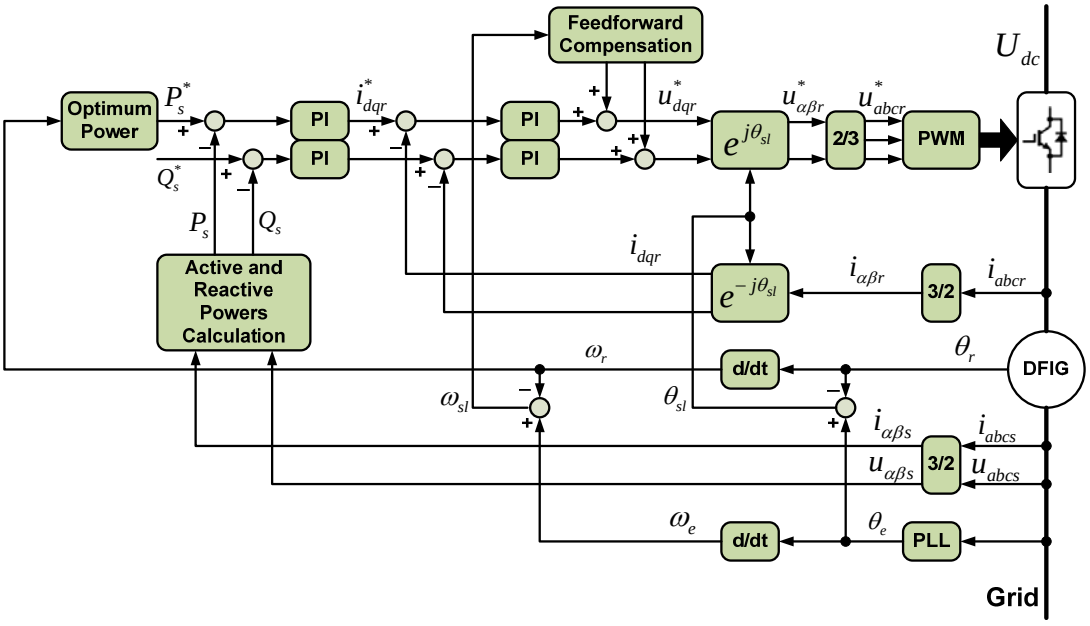

Figure 3.2 Vector control scheme for DFIGs.

$\theta_r = \int \omega_r dt$ is required for this field orientation. In the sensorless vector control system, the actual rotor position angle θ_r is not known and the estimated angle $\hat{\theta}_r = \int \hat{\omega}_r dt$ is obtained via estimators or observers. In closed-loop observers, rotor speed estimation is usually combined with flux estimation. The structure and parameters of observers have to be carefully designed and tuned such that desired observer dynamics are achieved.

If the stator flux and rotor current space vectors are chosen as complex state variables, the complex-valued DFIG model in the synchronous reference frame is given by

$$\frac{d}{dt}\boldsymbol{\psi_s} = (-a_1 - j\omega_s)\boldsymbol{\psi_s} + a_2\boldsymbol{i_r} + \boldsymbol{v_s} \tag{3.13}$$

$$\frac{d}{dt}\boldsymbol{i_r} = (a_3 + ja_4\omega_r)\boldsymbol{\psi_s} - (a_5 + j\omega_{sl})\boldsymbol{i_r} - a_4\boldsymbol{v_s} + a_6\boldsymbol{v_r} \tag{3.14}$$

where $a_1 = \frac{R_s}{L_s}$, $a_2 = \frac{R_s L_m}{L_s}$, $a_3 = \frac{R_s L_m}{\sigma L_s^2 L_r}$, $a_4 = \frac{L_m}{\sigma L_s L_r}$, $a_5 = \frac{R_s L_m^2 + R_r L_s^2}{\sigma L_s^2 L_r}$, and $a_6 = \frac{1}{\sigma L_r}$.

The parameters in the DFIG model are the stator resistance R_s, stator inductance L_s, rotor resistance R_r, rotor inductance L_r, mutual inductance L_m, and leakage coefficient $\sigma = 1 - L_m^2/(L_s L_r)$. The stator and rotor current space vectors are denoted by $\boldsymbol{i_s}$ and $\boldsymbol{i_r}$, the stator and rotor voltages by $\boldsymbol{v_s}$ and $\boldsymbol{v_r}$, and the stator and rotor flux by $\boldsymbol{\psi_s}$ and $\boldsymbol{\psi_r}$. The synchronous

speed, rotor electrical speed, mechanical speed, and slip speed are denoted by ω_s, ω_r, ω_m,and ω_{sl}, respectively. The electromagnetic torque is represented by

$$T_{em} = \frac{3}{2} n_p \frac{L_m}{L_s} \mathrm{Im}\left\{\boldsymbol{\psi_s} \boldsymbol{i_r^*}\right\} \tag{3.15}$$

where n_p is the number of pole pairs and the symbol "*" denotes the complex conjugate.

Vector control of DFIGs has been extensively studied in previous literature [30]-[32]. In the stator-flux-oriented reference frame, the direct (d) axis component and quadrature (q) axis component of the rotor current vector $\boldsymbol{i_r}$ are i_{dr} and i_{qr}, which are directly related to the stator reactive power and active power, respectively. Thus, decoupled control of the stator active and reactive power of a DFIG is achieved by controlling i_{qr} and i_{dr} to track desired reference values. The overall sensorless vector control system is shown in Figure 3.3. As shown in the figure, the d-axis rotor current command i_{dr}^* is calculated from the desired stator-side reactive power Q_s^*, while the q-axis rotor current command i_{qr}^* is generated from the speed proportional-integral (PI) controller for standalone drive applications, or the Maximum Power Point Tracking (MPPT) algorithm for grid-connected wind energy systems. To transform the rotor current vector between its natural reference frame rotating at the rotor angular speed ω_r and the stator-flux-oriented reference frame rotating at the synchronous speed ω_s, the knowledge of slip angle $\theta_{sl} = \theta_s - \theta_r$ where $\theta_s = \int \omega_s dt$ and $\theta_r = \int \omega_r dt$ is required for this field orientation. In the sensorless vector control system, the actual rotor position angle θ_r is not known and the estimated angle $\hat{\theta}_r = \int \hat{\omega}_r dt$ is obtained via estimators or observers. The structure and parameters of the sensorless observer have to be carefully designed and tuned such that desired observer dynamics are achieved. The speed and position observer is represented by a dashed box in Figure 3.3 and is the main focus of this chapter.

3.4 Novel Sensorless Vector Control Using A Speed-Adaptive Reduced-Order Observer

The speed-adaptive reduced-order observer proposed in this research is a simulation of the rotor current dynamic model with feedback of the estimation error and a speed adaptation loop [38]. The general block diagram is shown in Figure 3.4.

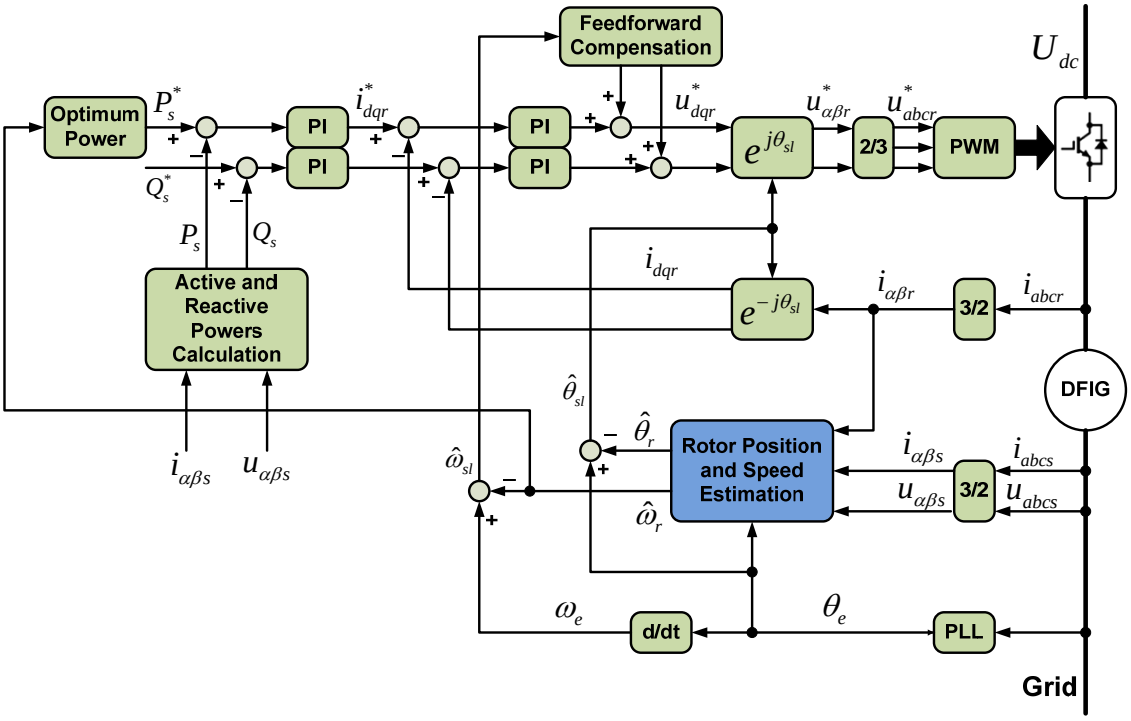

Figure 3.3 Sensorless control of DFIG.

3.4.1 Fundamental Structure

State observers are usually constructed as a simulation of the full-order dynamic model of the original system. Since the stator of DFIG is directly connected to the grid in most applications, the stator flux can be easily obtained from stator voltages and currents in the stator reference frame by the following equation

$$\boldsymbol{\psi_s^s} = \int (\boldsymbol{v_s^s} - R_s \boldsymbol{i_s^s}) dt. \tag{3.16}$$

The superscript "s" indicates the space vector is in the stator reference frame. Stator voltages as determined by the grid are known to be stiff and free of fluctuations in most of time except when severe grid faults occur. State currents are measurable quantities. Moreover, stator voltages and currents are 60 Hz signals, which introduce negligible errors when the pure integrator is replaced by a Low-Pass Filter (LPF) in the real implementation. Therefore, the stator flux in the stator reference frame can be considered as a known and accurate quantity. There is no need for calculating the stator flux estimation in the observer. Thus, only the rotor

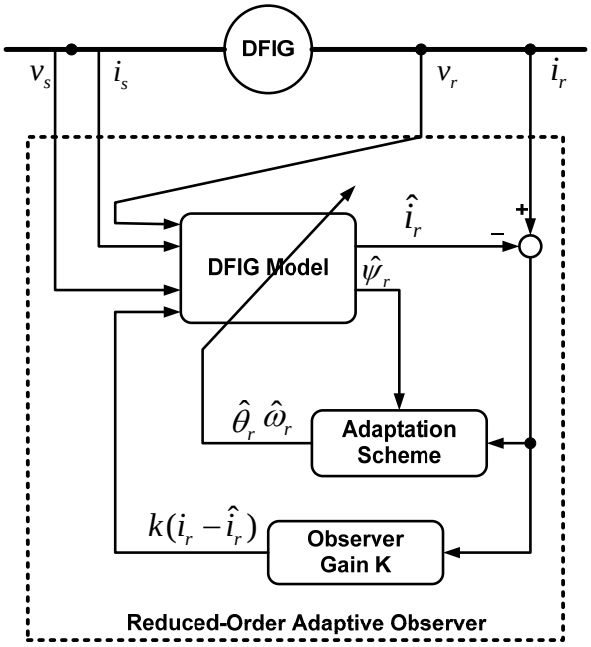

Figure 3.4 Speed-adaptive reduced-order observer.

current dynamic equation (3.14) is used to construct a reduced-order observer as

$$\begin{aligned}\frac{d\hat{\boldsymbol{i}}_{\boldsymbol{r}}}{dt} &= (a_3 + ja_4\hat{\omega}_r)\boldsymbol{\psi_s} - (a_5 + j\hat{\omega}_{sl})\hat{\boldsymbol{i}}_{\boldsymbol{r}} - a_4\boldsymbol{v_s} + a_6\boldsymbol{v_r} \\ &\quad + \boldsymbol{k}(\boldsymbol{i_r} - \hat{\boldsymbol{i}}_{\boldsymbol{r}})\end{aligned} \tag{3.17}$$

where $\boldsymbol{k} = k_1 + jk_2$ is the complex-valued observer gain.

The estimated variables are denoted by the symbol "ˆ". The rotor current estimation error is chosen as the corrective feedback to the observer because it is measurable and controllable by the sensorless vector control system. This is different from the sensorless vector controller for cage rotor induction motors. Because the observer equation is implemented in the synchronous reference frame, the stator flux $\boldsymbol{\psi_s}$ can be obtained by the reference frame transformation of $\boldsymbol{\psi}_{\boldsymbol{s}}^{\boldsymbol{s}}$ in (3.16). In the following analysis, machine parameters used in the observer are assumed to be accurate unless noted otherwise.

Subtracting the observer dynamic equation (3.17) from the rotor current dynamic equation (3.14), the rotor current estimation error dynamics of the observer are obtained as follows after

some algebraic manipulations

$$\begin{aligned}\dot{\boldsymbol{e}} &\triangleq \frac{d}{dt}(\boldsymbol{i_r} - \hat{\boldsymbol{i}}_{\boldsymbol{r}}) \\ &= -[a_5 + k_1 + j(\omega_{sl} + k_2)]\boldsymbol{e} + ja_6\hat{\boldsymbol{\psi}}_{\boldsymbol{r}}\Delta\omega_r\end{aligned} \tag{3.18}$$

where $\hat{\boldsymbol{\psi}}_{\boldsymbol{r}} = (a_4\boldsymbol{\psi_s} + \hat{\boldsymbol{i}}_{\boldsymbol{r}})/a_6$ and $\Delta\omega_r = \omega_r - \hat{\omega}_r$.

The electrical dynamics of the DFIG are characterized by two time scales. Generally speaking, the current dynamics are much faster than the flux dynamics [39]. Moreover, the mechanical dynamics are even slower than the electrical dynamics. Based on these assumptions, the error dynamics (3.18) can be considered as a linear system. Based on the linear control theory, the complex transfer function from the rotor speed estimation error $\Delta\omega_r$ to the rotor current estimation error $\Delta\boldsymbol{i_r}$ is

$$\begin{aligned}\boldsymbol{G_{i\omega}}(s) &= G_{i\omega d}(s) + jG_{i\omega q}(s) \\ &= \frac{ja_6(\hat{\psi}_{dr} + j\hat{\psi}_{qr})}{s + a_5 + k_1 + j(\omega_{sl} + k_2)}\end{aligned} \tag{3.19}$$

and we have

$$\boldsymbol{e}(s) = \boldsymbol{G_{i\omega}}(s)\Delta\omega_r. \tag{3.20}$$

By defining the error term

$$\epsilon = \frac{1}{a_6\left|\hat{\boldsymbol{\psi}}_{\boldsymbol{r}}^2\right|}\mathrm{Im}\left\{\Delta\boldsymbol{i_r}\hat{\boldsymbol{\psi}}_{\boldsymbol{r}}^*\right\} \tag{3.21}$$

and selecting a PI controller

$$\hat{\omega}_r = k_p\epsilon + k_i\int\epsilon dt \tag{3.22}$$

as the adaptive scheme, the open-loop transfer function from the rotor speed estimation error $\Delta\omega_r$ to the rotor speed estimation $\hat{\omega}_r$ can be obtained from (3.19)–(3.22) by

$$\begin{aligned}G_{op}(s) &= \frac{s + a_5 + k_1}{(s + a_5 + k_1)^2 + (k_2 + \omega_{sl})^2}\left(k_p + \frac{k_i}{s}\right) \\ &\triangleq G_{sys}(s)G_{adp}(s)\end{aligned} \tag{3.23}$$

where $G_{sys}(s)$ is defined to be the transfer function from the rotor speed estimation error $\Delta\omega_r$ to the error term ϵ and $G_{adp}(s)$ to be the transfer function of the PI adaptation controller.

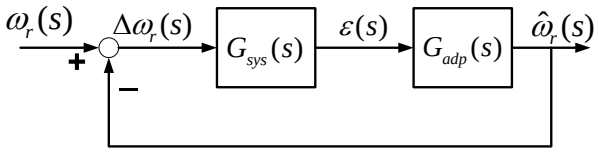

Figure 3.5 Block diagram of the closed-loop observer model.

Finally, the closed-loop transfer function from the actual rotor speed ω_r to the estimated rotor speed $\hat{\omega}_r$ is derived by

$$G_{cl}(s) = \frac{\hat{\omega}_r(s)}{\omega_r(s)} = \frac{G_{op}(s)}{1 + G_{op}(s)} \tag{3.24}$$

as shown in Figure 3.5. A variety of techniques, e.g., root locus plots and frequency responses, can be employed to design observer parameters based on this closed-loop observer model.

3.4.2 Design of Feedback and Adaptive Gains

Design of parameters in the speed-adaptive reduced-order observer is studied in this section. The parameters consist of the feedback gain $\boldsymbol{k}$ and adaptation gains k_p, k_i. By examining the open-loop transfer function (3.23), it is straightforward to select the following feedback gain

$$\boldsymbol{k} = k_1 + jk_2 \Rightarrow \begin{cases} k_1 = \omega_{ce} - a_5 \\ k_2 = -\omega_{sl} \end{cases} \tag{3.25}$$

where ω_{ce} is the crossover frequency of speed estimation loop in the observer. In this way, the open-loop transfer function of the observer is simplified to

$$G_{op}(s) = \frac{1}{s + \omega_{ce}} \left(k_p + \frac{k_i}{s} \right). \tag{3.26}$$

The adaptation gains k_p and k_i are designed by considering frequency responses of the observer model. We can select the crossover frequency ω_{ce} to be the same order as that of the rotor current PI control loop, or one order of magnitude larger than that of the speed control loop if the DFIG is speed-controlled, since it is desirable that an observer is faster than the plant dynamics in order to give good tracking. As known for the frequency responses of the closed-loop system, the phase delay at the crossover frequency introduced by the open-loop transfer

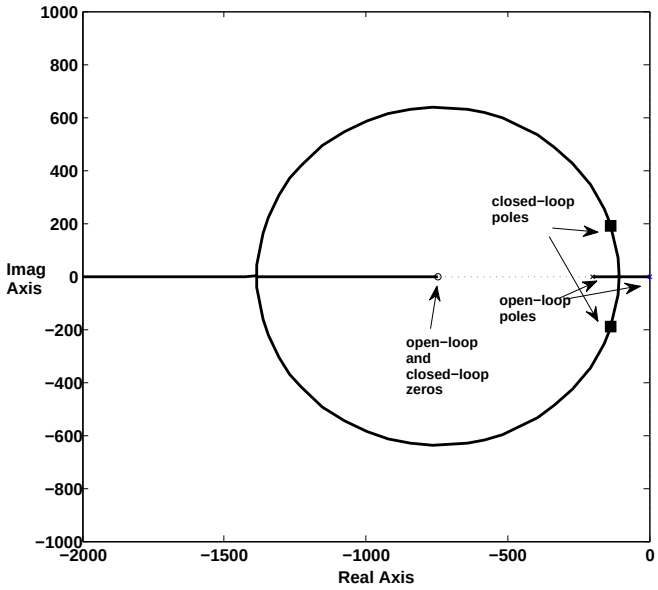

Figure 3.6 Root locus plot of the open-loop transfer function G_{op}.

function must be less than 180 degree in order for the closed-loop feedback system to be stable. Based on these design guidelines, the expression of open-loop transfer function (3.26) yields the following two equations at the crossover frequency:

$$\left| \frac{k_i}{\omega_{ce}} \cdot \frac{1 + (k_p/k_i)s}{s\,(1 + s/\omega_{ce})} \right|_{s=j\omega_{ce}} = 1 \tag{3.27}$$

and

$$\angle \frac{k_i}{\omega_{ce}} \cdot \frac{1 + (k_p/k_i)s}{s\,(1 + s/\omega_{ce})} \Big|_{s=j\omega_{ce}} = -180^\circ + \phi_{pm} \tag{3.28}$$

where ϕ_{pm} is the phase margin. The two adaptation gains of the PI controller can be calculated by solving these two equations with some reasonable crossover frequency and phase margin.

The root locus plot of the open-loop transfer function G_{op} is shown in Figure 3.6. This plot is based on the selection of a crossover frequency $\omega_{ce} = 200$ rad/sec(≈ 30 Hz) and a phase margin $\phi_{pm} = 60^\circ$. The corresponding adaptation gains k_p and k_i are solved from (3.27) and (3.28). The frequency responses of open-loop and closed-loop transfer functions are plotted in Figure 3.7. It can be predicted that the observer has good dynamic performance in terms of fast tracking and sufficient damping when the proposed feedback and adaptation gains are applied.

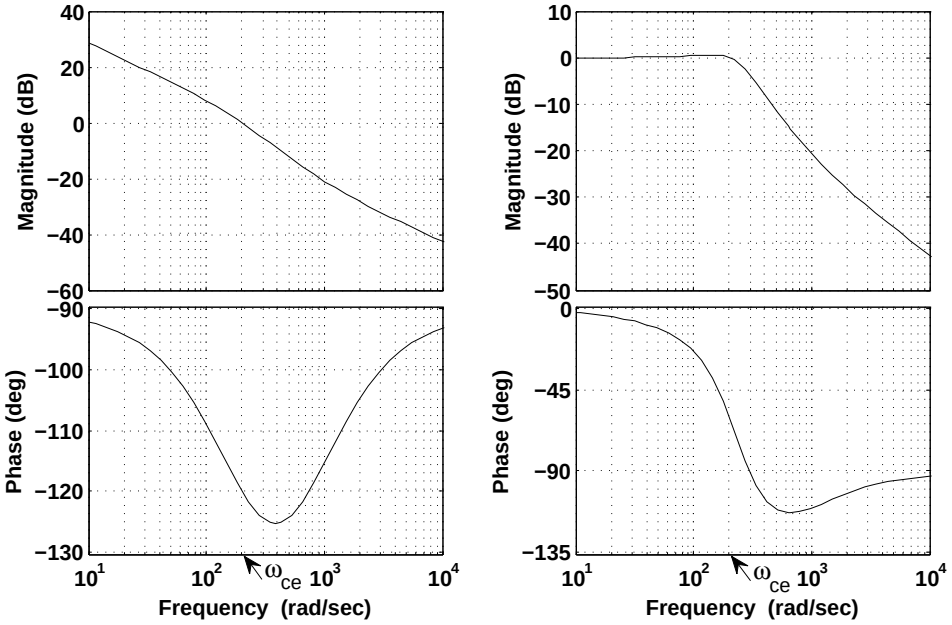

Figure 3.7 Frequency response of observer transfer functions: (left column) open-loop; (right column) closed-loop.

The implementation of gain k_2 in (3.25) in a real sensorless vector control system is unrealistic because the real rotor speed is required. However, with properly designed adaptation PI gains as discussed in this section, the estimated rotor speed can track the actual value very precisely. Hence, we can alternatively make an approximation of the gain by

$$k_2 = -\hat{\omega}_{sl} \tag{3.29}$$

without introducing any significant errors. This will be further demonstrated in simulation studies.

3.4.3 Parameter Sensitivity Analysis

In reality, parameter variations are unavoidable due to the temperature increase and magnetic saturation. The reduced-order observer is based on the rotor current dynamics, where all machine parameters including resistance and inductance are involved for estimation of rotor currents. Therefore, an observer study considering machine parameter variations is necessary. In this section, we assume an "open-loop" implementation of the observer, meaning that the

estimated speed and position output by the observer are not used in the vector control system. Under this assumption, the influences of each machine parameter variations on the speed estimation are investigated by deriving the relationship between the speed estimation error and parameter mismatch. The influences of parameter variations on "closed-loop" implementation of the observer will be studied by dynamic simulations in the next section.

Firstly, the influence of stator resistance variation is studied. The rotor current estimation error (3.20) can be reformulated to include the stator resistance error as

$$\boldsymbol{e}(s) = \boldsymbol{G_{i\omega}}(s)\Delta\omega_r + \boldsymbol{G_{iR_s}}(s)\Delta R_s \tag{3.30}$$

where $\Delta R_s = R_s - \hat{R}_s$. The transfer function $\boldsymbol{G_{i\omega}}(s)$ has been derived in (3.19), while $\boldsymbol{G_{iR_s}}(s)$ is shown as

$$\boldsymbol{G_{iR_s}}(s) = \frac{a_4\hat{\boldsymbol{i}}_{\boldsymbol{s}}}{(s + a_5 + k_1) + j(\omega_{sl} + k_2)} \tag{3.31}$$

where $\hat{\boldsymbol{i}}_s = (\boldsymbol{\psi_s} - L_m\hat{\boldsymbol{i}}_{\boldsymbol{r}})/L_s$.

Considering the assumption that the error term ϵ defined in (3.21) is driven to zero ($\epsilon = 0$) in the steady-state condition by the PI adaptation scheme, we can derive the rotor speed estimation error against the stator resistance error using (3.19), (3.21), (3.25), (3.29), (3.30), and (3.31) as

$$\Delta\omega_r = \frac{-a_4\omega_{ce}\mathrm{Im}\left\{\hat{\boldsymbol{i}}_{\boldsymbol{s}}\hat{\boldsymbol{\psi}}_{\boldsymbol{r}}^*\right\}\Delta R_s}{a_6\left|\hat{\boldsymbol{\psi}}_{\boldsymbol{r}}\right|^2\omega_{ce} + a_4\mathrm{Re}\left\{\hat{\boldsymbol{i}}_{\boldsymbol{s}}\hat{\boldsymbol{\psi}}_{\boldsymbol{r}}^*\right\}\Delta R_s}. \tag{3.32}$$

A more detailed derivation of (3.30)-(3.32) is given in the following context.

If the stator resistance in the control system is inaccurate ($\Delta R_s = R_s - \hat{R}_s \neq 0$), the rotor current error dynamics of the reduced-order observer can be found by subtracting (3.17) from (3.14) and taking into account the coefficient error in a_1, a_2, a_3, and a_5 due to the R_s mismatch. After some algebraic manipulations, the result is shown to be

$$\begin{aligned}\dot{\boldsymbol{e}} = \Delta\dot{\boldsymbol{i}}_{\boldsymbol{r}} &= -[a_5 + k_1 + j(\omega_{sl} + k_2)]\Delta\boldsymbol{i_r} \\ &\quad + ja_6\hat{\boldsymbol{\psi}}_{\boldsymbol{r}}\Delta\omega_r + a_4\hat{\boldsymbol{i}}_{\boldsymbol{s}}\Delta R_s.\end{aligned} \tag{3.33}$$

Therefore, (3.30) and (3.31) can be obtained by taking the Laplace transformation on (3.33).

From (3.21), the error term is shown to be

$$\epsilon = \frac{1}{a_6 \left|\hat{\boldsymbol{\psi}}_{\boldsymbol{r}}^2\right|}(\Delta i_{qr}\hat{\psi}_{dr} - \Delta i_{dr}\hat{\psi}_{qr}) \tag{3.34}$$

where

$$\Delta i_{dr} = G_{i\omega,d}(s)\Delta\omega_r + G_{iR_s,d}(s)\Delta R_s, \tag{3.35}$$

$$\Delta i_{qr} = G_{i\omega,q}(s)\Delta\omega_r + G_{iR_s,q}(s)\Delta R_s, \tag{3.36}$$

and $G_{i\omega,d}(s) = \mathrm{Re}\left\{\boldsymbol{G_{i\omega}}(s)\right\}$, $G_{i\omega,q}(s) = \mathrm{Im}\left\{\boldsymbol{G_{i\omega}}(s)\right\}$, $G_{iR_s,d}(s) = \mathrm{Re}\left\{\boldsymbol{G_{iR_s}}(s)\right\}$, $G_{iR_s,q}(s) = \mathrm{Im}\left\{\boldsymbol{G_{iR_s}}(s)\right\}$.

The error term is assumed to be driven to zero in the steady-state operation. Hence, (3.32) can be easily derived by equating the right-hand side of (3.34) to zero and solving the resulting equation.

Equation (3.37)-(3.39) are derived in the same manner as described above. Δ

Based on (3.32), the rotor speed estimation error for normal operating conditions of a typical 1.5-MW DFIG [43] can be shown on the torque-speed plane as in Figure 3.8 and Figure 3.9. It can be seen that the speed estimation error depends mainly on the speed that the DFIG is operating on. Although the speed errors are generally larger when DFIG is operating around the synchronous speed, they are still negligible. The error is more significant if the actual stator resistance is smaller than the value used in the observer as seen from Figure 3.9. However, this situation is unlikely to happen because the actual stator resistance is usually larger than the nominal value in reality due to the temperature increase.

Secondly, the influence of rotor resistance variation is studied in the same manner. The rotor current estimation error against the rotor resistance error and rotor speed error is shown by

$$\boldsymbol{e}(s) = \boldsymbol{G_{i\omega}}(s)\Delta\omega_r + \boldsymbol{G_{iR_r}}(s)\Delta R_r \tag{3.37}$$

where $\Delta R_r = R_r - \hat{R}_r$.

The transfer function $\boldsymbol{G_{iR_r}}(s)$ can be derived as

$$\boldsymbol{G_{iR_r}}(s) = \frac{-a_6\hat{\boldsymbol{i}}_r}{(s + a_5 + k_1) + j(\omega_{sl} + k_2)}. \tag{3.38}$$

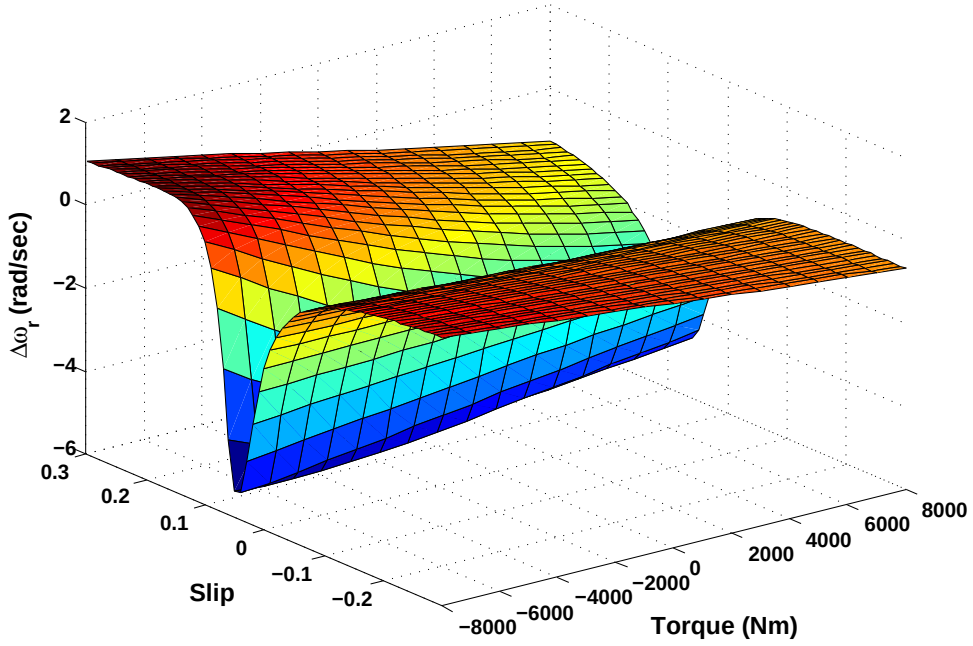

Figure 3.8 Effects of machine stator resistance variation on rotor speed estimation ($R_s = 1.5\hat{R}_s$).

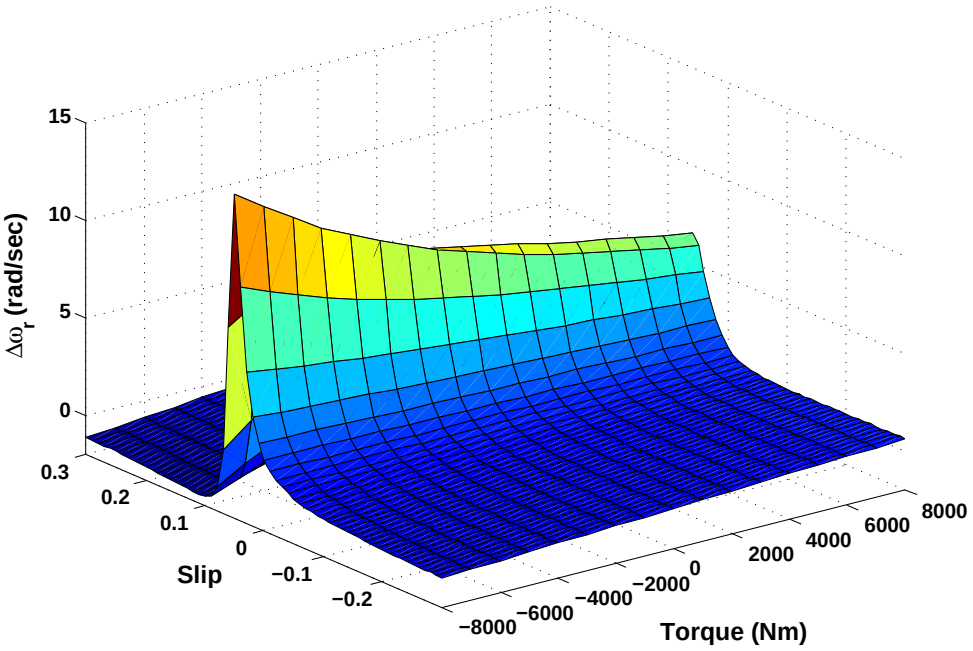

Figure 3.9 Effects of machine stator resistance variation on rotor speed estimation ($R_s = 0.5\hat{R}_s$).

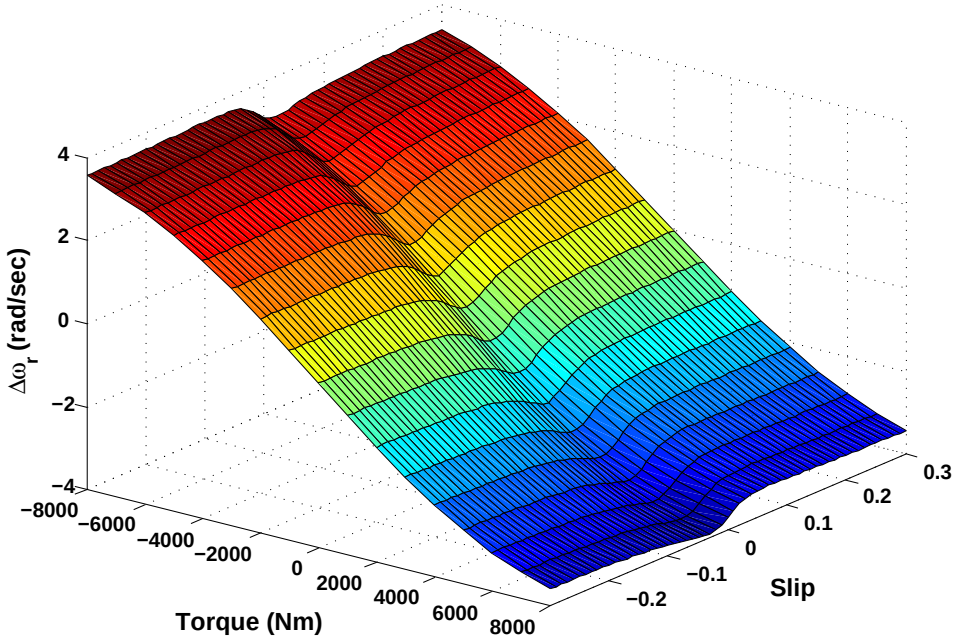

Figure 3.10 Effects of machine rotor resistance variation on rotor speed estimation ($R_r = 1.5\hat{R}_r$).

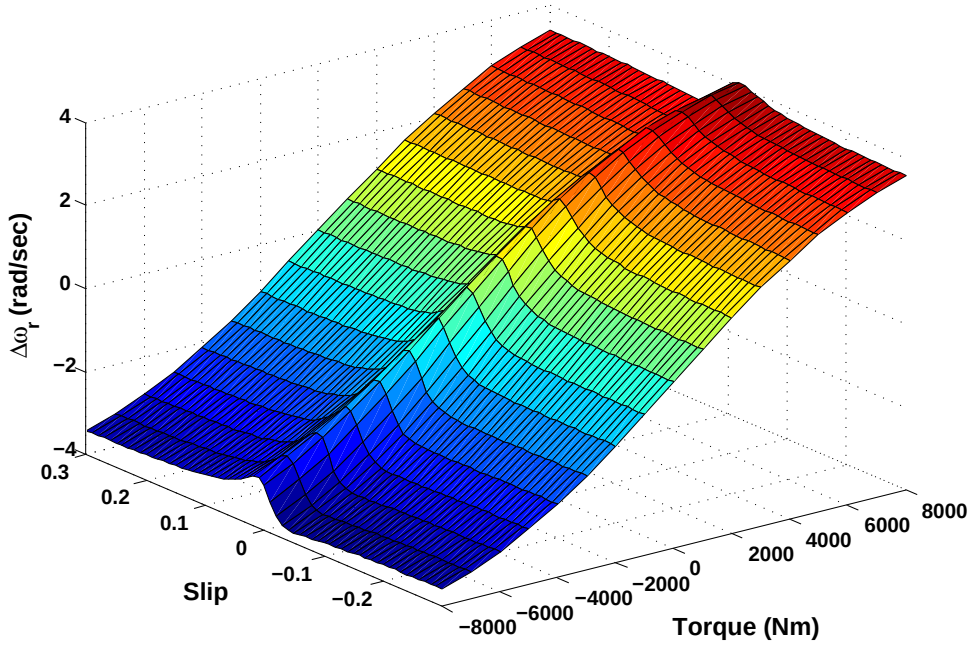

Figure 3.11 Effects of machine rotor resistance variation on rotor speed estimation ($R_r = 0.5\hat{R}_r$).

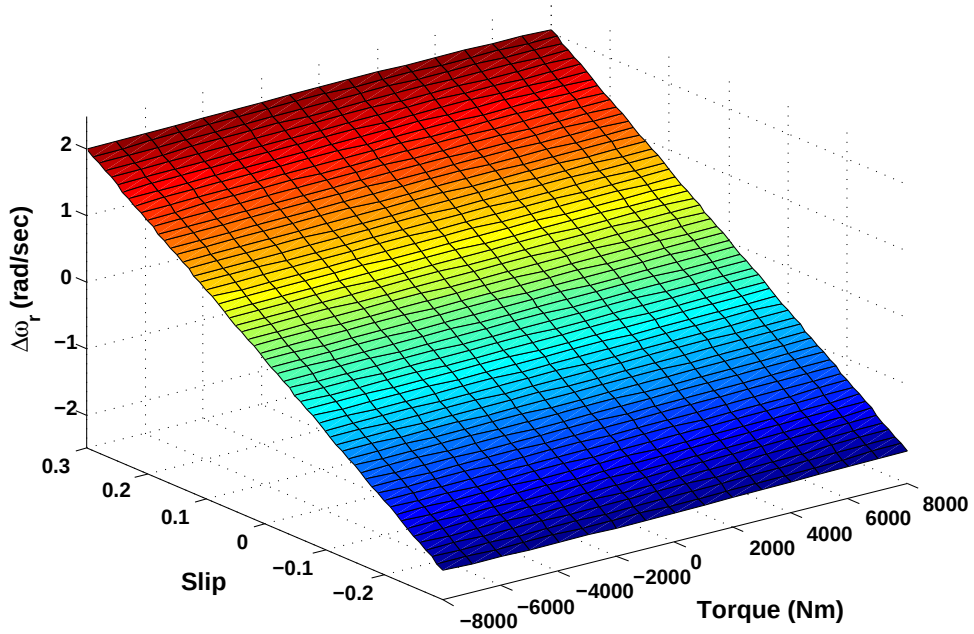

Figure 3.12 Effects of machine mutual inductance variation on rotor speed estimation ($L_m = 1.5\hat{L}_m$).

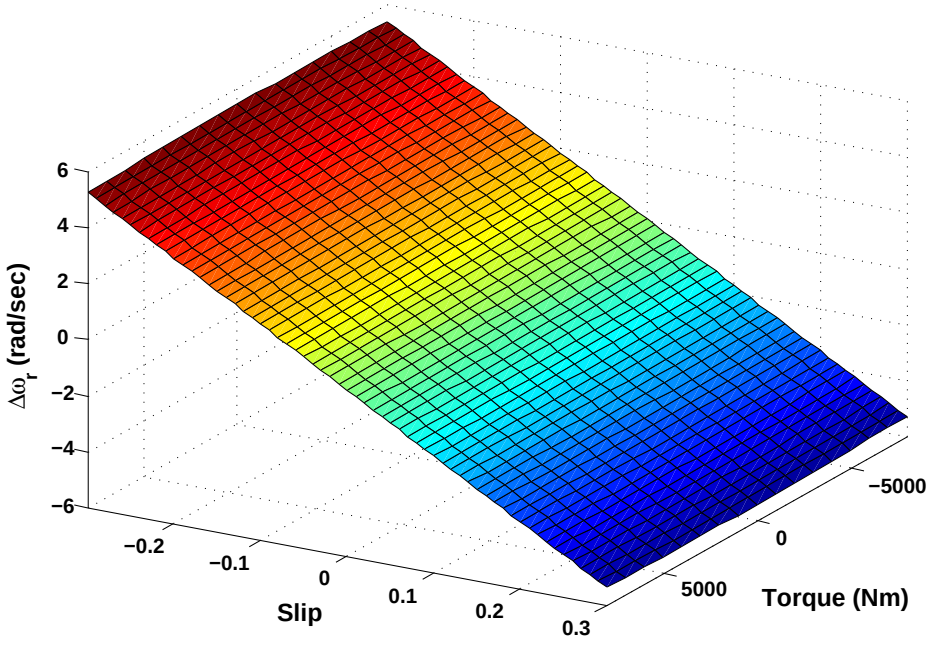

Figure 3.13 Effects of machine mutual inductance variation on rotor speed estimation ($L_m = 0.5\hat{L}_m$).

Therefore, the rotor speed estimation error against the rotor resistance error can be derived using (3.19), (3.21), (3.25), (3.29), (3.37), and (3.38) as

$$\Delta\omega_r = \frac{\omega_{ce}\mathrm{Im}\left\{\hat{\boldsymbol{i}}_{\boldsymbol{r}}\hat{\boldsymbol{\psi}}_{\boldsymbol{r}}^{*}\right\}\Delta R_r}{\left|\hat{\boldsymbol{\psi}}_{\boldsymbol{r}}\right|^2\omega_{ce} - \mathrm{Re}\left\{\hat{\boldsymbol{i}}_{\boldsymbol{r}}\hat{\boldsymbol{\psi}}_{\boldsymbol{r}}^{*}\right\}\Delta R_r}. \tag{3.39}$$

A more detailed derivation of (3.37)-(3.39) can be conducted using the similar approach for derivation of (3.30)-(3.32) in the previous context. The effects of rotor resistance variation on speed estimation are calculated by (3.39) and depicted in Figure 3.10 and Figure 3.11. In this case, the speed estimation error depends mainly on the load torque.

Finally, the effects of mutual inductance variation are investigated. The derivation of an analytical relationship between the speed estimation error and mutual inductance error similar to (3.32) and (3.39) is very cumbersome. Thus a numerical iteration approach similar to that in [44] is resorted to determine the steady-state solution of the estimated rotor speed $\hat{\omega}_r$. The results are shown in Figure 3.12 and Figure 3.13. It can be seen that the speed estimation error depends mainly on the machine speed in the case of mutual inductance variations.

Actually, (3.32) and (3.39) can be further simplified to obtain the direct derivative of the speed over the derivative of the machine resistance (R_s and R_r), which can be considered as the sensitivity of the speed against machine parameter variations. In (3.32), it is found that $a_6\left|\hat{\boldsymbol{\psi}}_{\boldsymbol{r}}^2\right|\omega_{ce} >> a_4\mathrm{Re}\left\{\hat{\boldsymbol{i}}_{\boldsymbol{s}}\hat{\boldsymbol{\psi}}_{\boldsymbol{r}}^{*}\right\}\Delta R_s$ if normal machine parameters and operating conditions are assumed. Therefore, the derivative of the speed over the stator resistance can be obtained from (3.32) as

$$\frac{\Delta\omega_r}{\Delta R_s} = -\frac{a_4\mathrm{Im}\left\{\hat{\boldsymbol{i}}_{\boldsymbol{s}}\hat{\boldsymbol{\psi}}_{\boldsymbol{r}}^{*}\right\}}{a_6\left|\hat{\boldsymbol{\psi}}_{\boldsymbol{r}}\right|^2}. \tag{3.40}$$

Similarly, the derivative of the speed over the rotor resistance can be obtained from (3.39) as

$$\frac{\Delta\omega_r}{\Delta R_r} = \frac{\mathrm{Im}\left\{\hat{\boldsymbol{i}}_{\boldsymbol{r}}\hat{\boldsymbol{\psi}}_{\boldsymbol{r}}^{*}\right\}}{\left|\hat{\boldsymbol{\psi}}_{\boldsymbol{r}}\right|^2}. \tag{3.41}$$

the derivative of the speed over the mutual inductance can also be obtained using the numerical iteration approach similar to that in [44] mentioned in the previous context.

Therefore, the sensitivity of the rotor speed against the machine parameter variations is shown in Figure 3.14 through Figure 3.16.

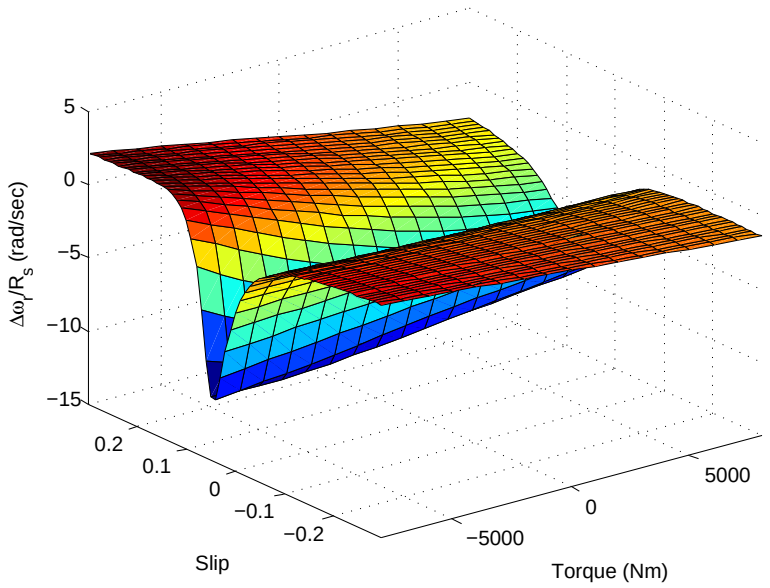

Figure 3.14 Sensitivity of rotor speed against stator resistance.

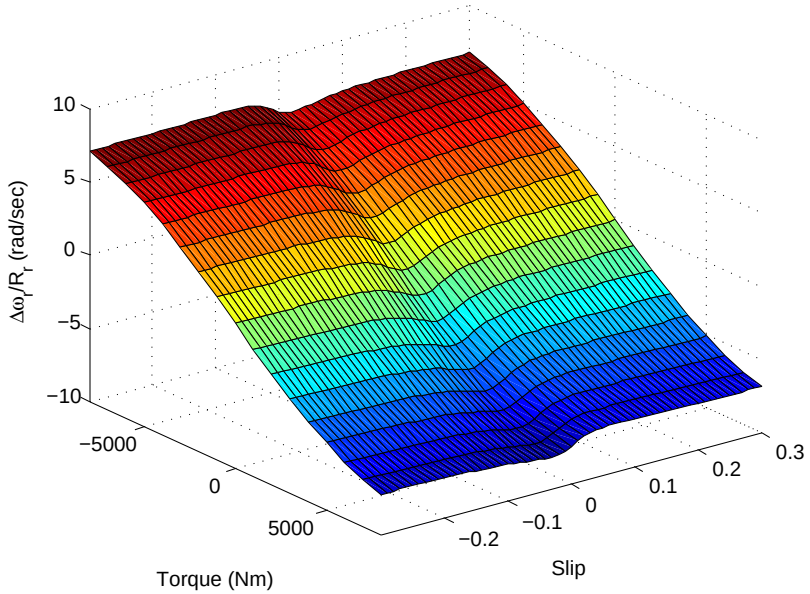

Figure 3.15 Sensitivity of rotor speed against rotor resistance.

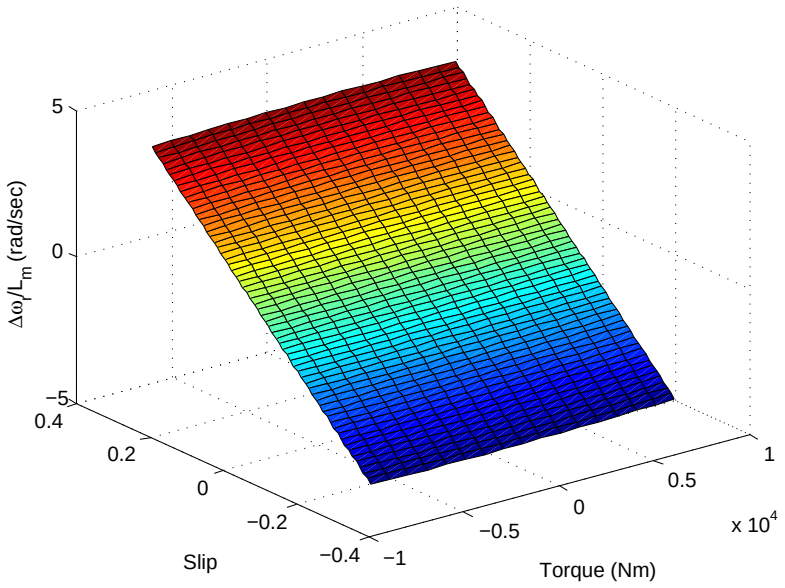

Figure 3.16 Sensitivity of rotor speed against mutual inductance.

It can be summarized from Figure 3.8-3.16 that the reduced-order observer is almost insensitive to all machine parameter variations. Among all the effects of parameter variations, the stator resistance error has the most significant influence on the "open-loop" rotor speed estimation. In previous work related to MRAS sensorless observer [13]-[15], it has been shown that their accuracy is highly dependent on the mutual inductance, which is more challenging for on-line parameter schemes because the changes in DFIG's mutual inductance due to saturation are generally more rapid than that of temperature-related resistance [40]. Another advantage of the reduced-order observer over MRAS observers is that on-line stator or rotor resistance estimators are easy to design and implement using the same framework for speed observers [41], while on-line estimation of the mutual inductance is more difficult because the knowledge of the magnetizing curve is required [42].

3.5 Real-Time Simulation Results

Simulations of the sensorless vector control system in Figure 3.3 for a 1.5-MW DFIG are carried out using the real-time simulation platform presented in Chapter 2. Based on the

proposed sensorless reduced-order observer, the rotor-side converter controls the rotor currents to track the speed and position references in stand-alone applications, or produce desired stator active and reactive powers in wind generation applications. The grid-side converter has to maintain a constant DC link voltage and regulates the converter-side reactive power, using the conventional vector control approach [30]. Both rotor-side and grid-side converters operate at the switching frequency of 6 kHz using the SVPWM technique. The parameters of the DFIG and control system are given below.

DFIG (modified from [43]): Rated apparent power $S = 1.5/0.9$ MVA. Rated power $P = 1.5$ MW. Rated voltage (line-to-line) $V_{ll} = 690$ V. Frequency $f = 60$ Hz. $R_s = 0.0014\Omega$. $R_r = 9.9187 \times 10^{-4}\Omega$. $L_m = 1.526 \times 10^{-3}$ H. $L_{ls} = 8.998 \times 10^{-5}$ H. $L_{lr} = 8.2088 \times 10^{-5}$ H. Shaft inertia $J = 18.7kg \cdot m^2$. Pole pairs $n_p = 2$.

Control System:

Reduced-order observer: speed adaptation bandwidth ≈ 40 Hz, damping coefficient ≈ 0.6; feedback gain $k_1 = 186.6$, $k_2 = -\hat{\omega}_{sl}$; adaptation gain $k_{pe} = 73.2$, $k_{ie} = 5.46 \times 10^4$.

Rotor current controller: bandwidth ≈ 70 Hz; PI controller gain $k_{pi} = 0.0574$, $k_{ii} = 13.7$.

Speed controller: bandwidth ≈ 7 Hz; PI controller gain $k_{ps} = -187.4$, $k_{is} = -4.33 \times 10^3$.

3.5.1 Speed and Torque Tracking

In the first simulation study, the DFIG is assumed to be speed controlled. The speed PI controller is designed using the similar approach as described for the adaptation PI controller in the observer. The tracking performance of the generator rotor speed and angle using proposed observer is tested under various reference speeds, including sub-synchronous, super-synchronous, and synchronous operations.

The actual and estimated rotor speeds and positions are shown in Figure 3.17 for the speed acceleration and deceleration between 0.7 pu (1260 rpm) and 1.3 pu (2340 rpm). The electromagnetic torque, q-axis rotor current, magnetizing current, and rotor phase current corresponding to the whole process are all plotted in Figure 3.18. The speed error is less than ± 3 rpm and the position error is less than ± 0.5 degree during speed variations. The mechanical

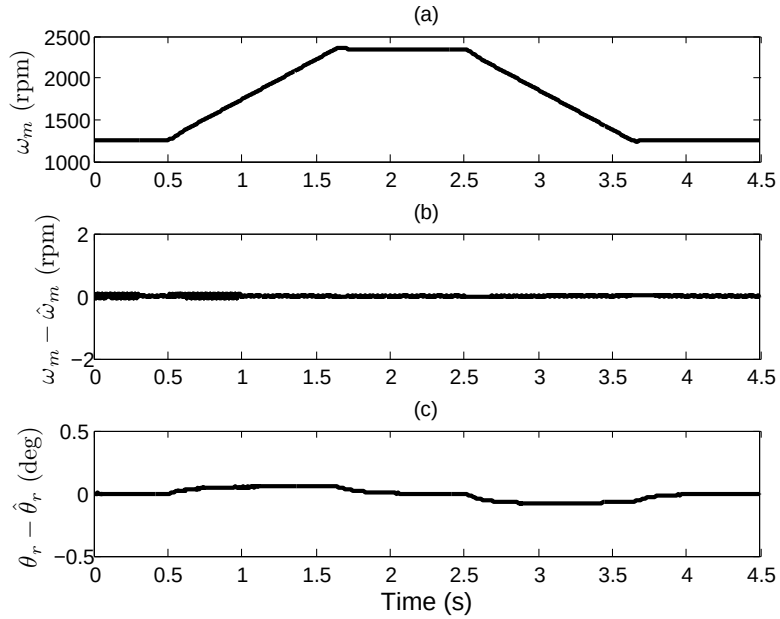

Figure 3.17 Actual and estimated rotor speeds and positions for speed variations.

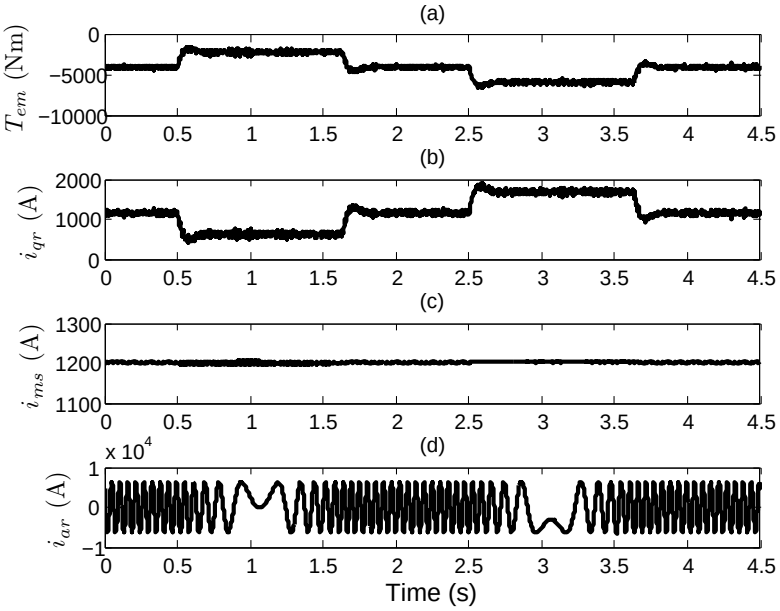

Figure 3.18 Electromagnetic torque and currents for speed variations.

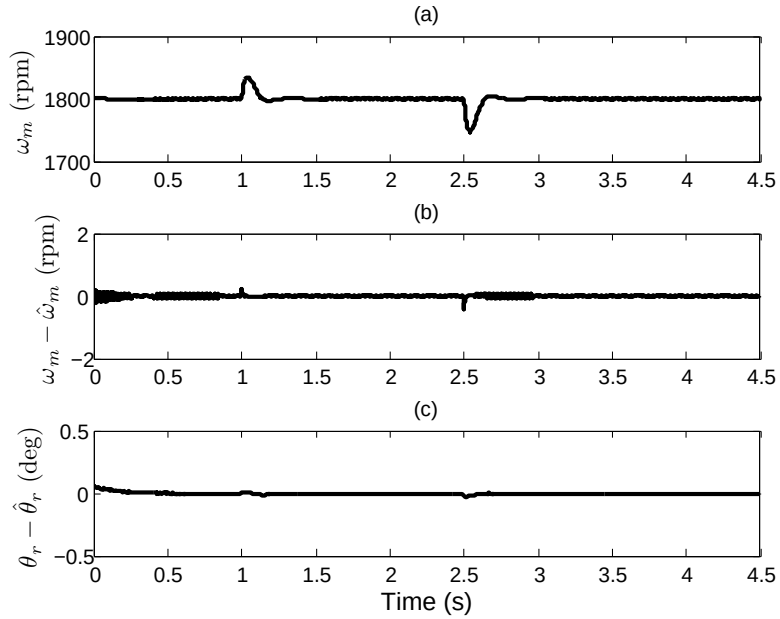

Figure 3.19 Actual and estimated rotor speeds and positions for torque variations.

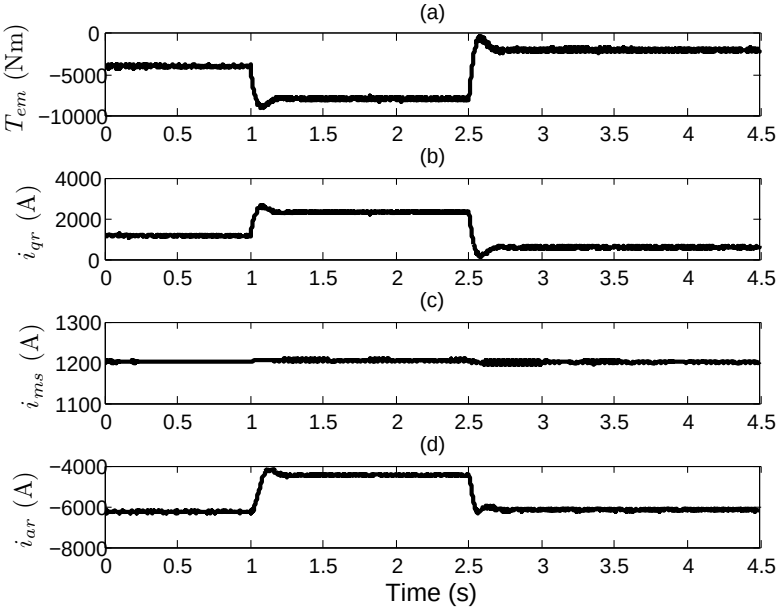

Figure 3.20 Electromagnetic torque and currents for torque variations.

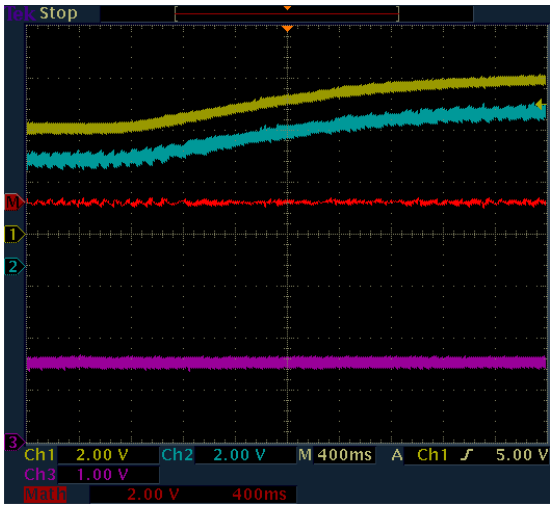

Figure 3.21 Oscilloscope trace of the speed ω_m, estimated speed $\hat{\omega}_m$, dc-link voltage V_{dc}, and speed estimation error $\Delta\omega_m = \omega_m - \hat{\omega}_m$, when the speed is controlled to increase from 0.8 pu to 1.2 pu. X-axis: 0.4s/div., Y-axis: Ch1(ω_m) 0.4 pu/div., Ch2($\hat{\omega}_m$) 0.4 pu/div., Ch3(V_{dc}) 1 kV/div., ChM($\Delta\omega_m$) 0.4 pu/div.

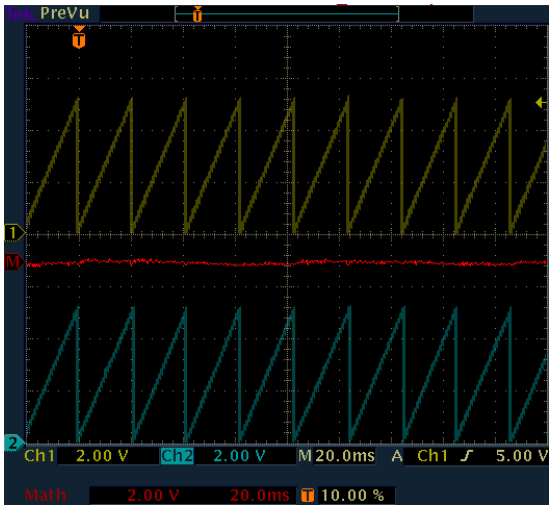

Figure 3.22 Oscilloscope trace of the rotor angle θ_m, estimated rotor angle $\hat{\theta}_m$, and rotor angle estimation error $\Delta\theta_m = \theta_m - \hat{\theta}_m$, when the speed is controlled at 0.8 pu. X-axis: 0.02s/div., Y-axis: Ch1(θ_m) 0.8π rad/div., Ch2($\hat{\theta}_m$) 0.8π rad/div., ChM($\Delta\theta_m$) 0.8π rad/div.

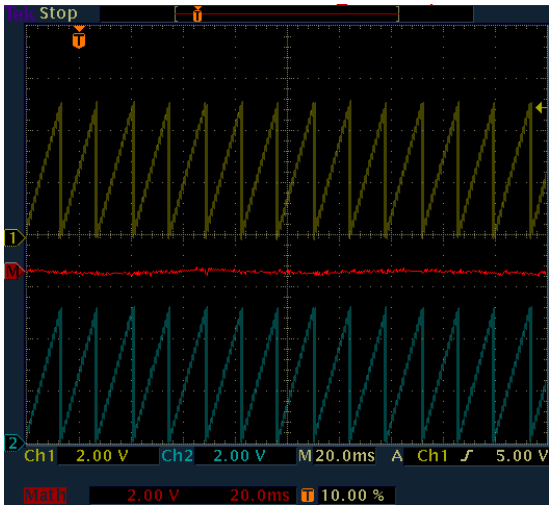

Figure 3.23 Oscilloscope trace of the rotor angle θ_m, estimated rotor angle $\hat{\theta}_m$, and rotor angle estimation error $\Delta\theta_m = \theta_m - \hat{\theta}_m$, when the speed is controlled at 1.2 pu. X-axis: 0.02s/div., Y-axis: Ch1(θ_m) 0.8π rad/div., Ch2($\hat{\theta}_m$) 0.8π rad/div., ChM($\Delta\theta_m$) 0.8π rad/div.

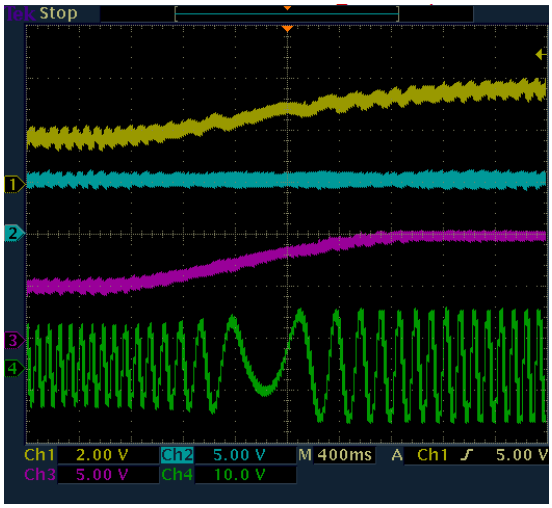

Figure 3.24 Oscilloscope trace of the electrical torque T_e, d-axis rotor current i_{dr}, q-axis rotor current i_{qr}, and phase A rotor current i_{ar}, when the speed is controlled to increase from 0.8 pu to 1.2 pu. X-axis: 0.4s/div., Y-axis: Ch1(T_e) 0.4 pu/div., Ch2(i_{dr}) 0.5 pu/div., Ch3(i_{qr}) 0.5 pu/div., Ch4(i_{ar}) 1 pu/div.

load torque is maintained at -0.5 pu (-4000 Nm). In steady state, the electromagnetic torque generated by the DFIG equals the mechanical torque. When the speed varies, an extra torque is generated for acceleration or deceleration.

The sensorless operation of DFIG at synchronous speed (1800 rpm) is shown in Figure 3.19 and Figure 3.20. The mechanical load torque is -0.5 pu initially and increases to -1 pu at $t = 1$ s and drops to -0.25 pu at $t = 2.5$ s. The performance of the reduced-order observer is satisfactory with negligible speed and position estimation errors.

In previous two simulation cases, the q-axis rotor current i_{qr} is controlled according to torque variations. The magnetizing current i_{ms} is regulated such that the stator reactive power of the DFIG is approximately zero.

Figure 3.21 through Figure 3.24 show the oscilloscope traces of DFIG parameters when the speed is controlled from 0.8 pu to 1.2 pu.

All simulation results in this section have shown fast and accurate dynamic responses of the proposed sensorless controller.

3.5.2 Maximum Wind Power Tracking

In the second case, a simulation for a complete wind generation system including a sensorless controlled DFIG-based wind turbine using the proposed reduced-order observer is carried out. Figure 3.26 shows the schematic of the simulated wind turbine system. The parameters of the turbine and grid are taken from a Simulink demo [45]. The sensorless vector control with the adaptive observer is applied to the DFIG torque control. The maximum power point tracking (MPPT) algorithm is used in this simulation study to control the wind turbine. A wind turbine model in Simulink [45] is adopted in this simulation. The mechanical power P_m as a function of generator speed, for different wind speeds and for blade pitch angle $\beta = 0$ degree, is shown in Figure 3.25. The figure is obtained with the base wind speed = 12 m/s, maximum power at base wind speed = 0.8 pu and base rotor speed = 1.2 pu. From this figure, we can observer that for each wind speed, there is a maximum point on the $P_m - \omega_m$ curve. Combining these maximum power point, a curve P_{opt} is obtained. The objective of the MPTT algorithm is to

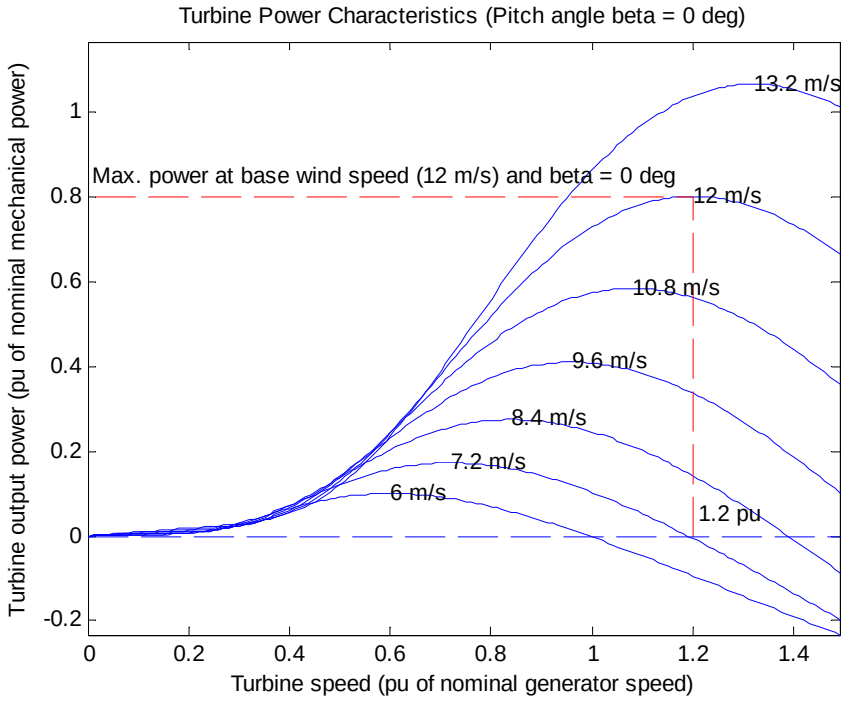

Figure 3.25 Wind turbine power-speed characteristics.

keep the turbine power output on this curve as the wind speed varies.

This is achieved by setting the generator torque command T_e^* to $K_\lambda \omega_m^2$ where ω_m is the generator rotor speed in per unit and K_λ is given by

$$K_\lambda = \frac{\pi \rho R^5 C_p(\lambda, \beta)}{2\lambda^3 G^3} \tag{3.42}$$

This ensures that in the steady state the turbine will maintain the optimal tip speed ratio λ_{opt} and the corresponding maximum power coefficient $C_p(\lambda, \beta)$.

A wind speed model modified from chapter 25.5.2 in [2] is used as the input wind profile. The wind speed and wind power are depicted in Figure 3.27. The rated wind speed is assumed to be 12 m/s and the optimal rotor speed of the DFIG at the rated condition is 1.2 pu. For wind speeds higher than rated, the turbine energy capture must be limited by applying pitch control or stall control. In this simulation study, these limiting approaches are not considered. The gearbox is assumed to be of no mechanical power loss. The DFIG is torque controlled in the simulation and the torque current i_{qr} is proportional to the square of the estimated rotor

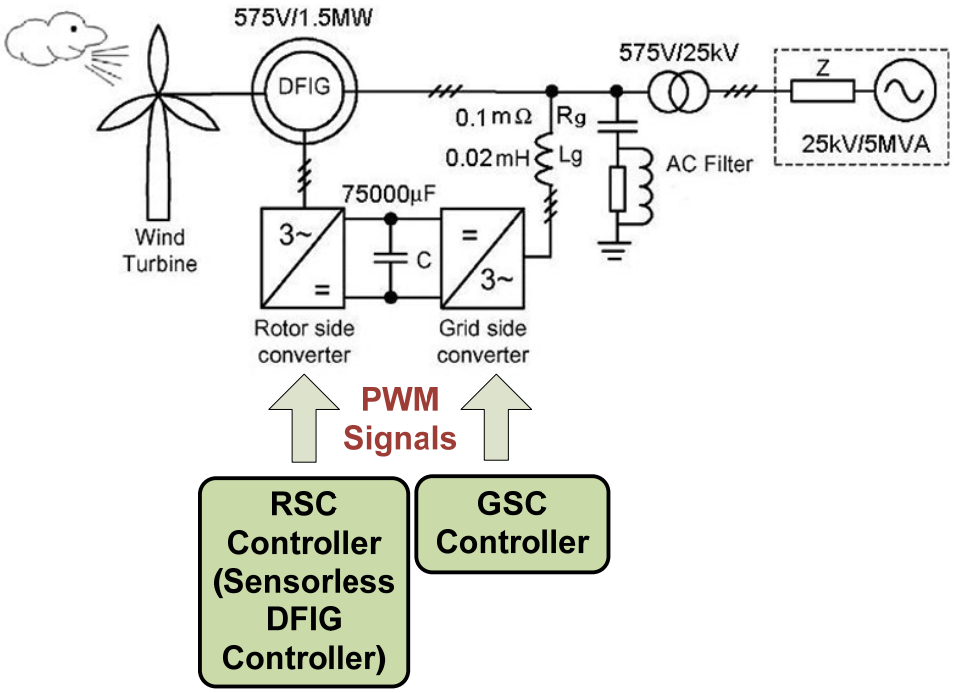

Figure 3.26 Simulated DFIG-based wind turbine system diagram.

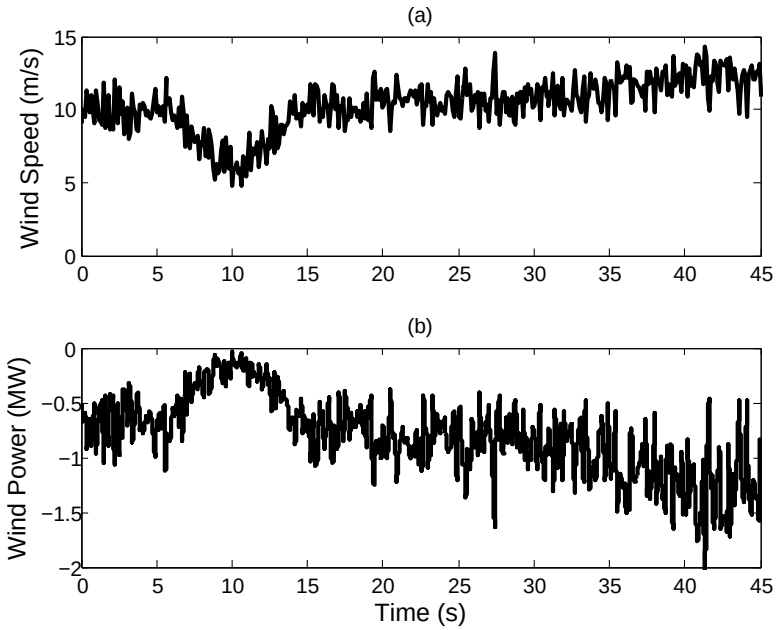

Figure 3.27 Wind speed and turbine mechanical input power.

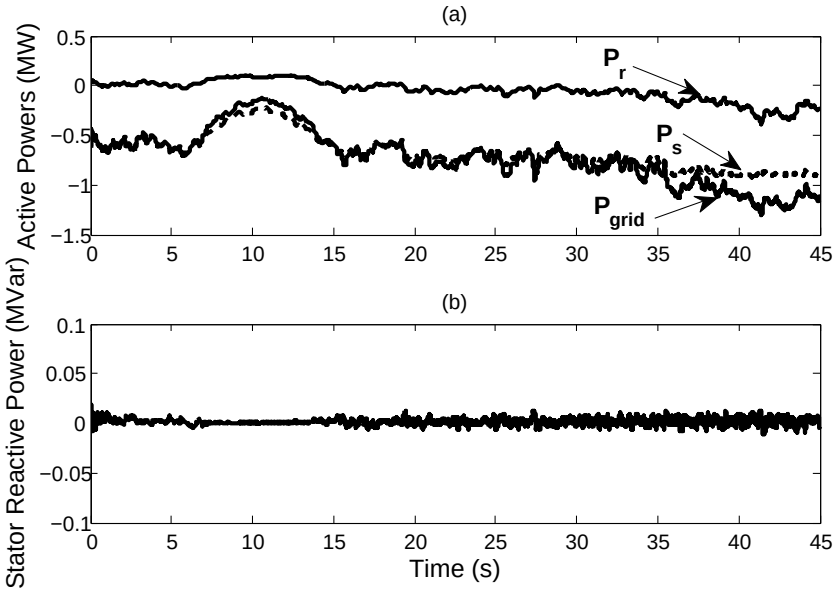

Figure 3.28 Generator active and reactive powers.

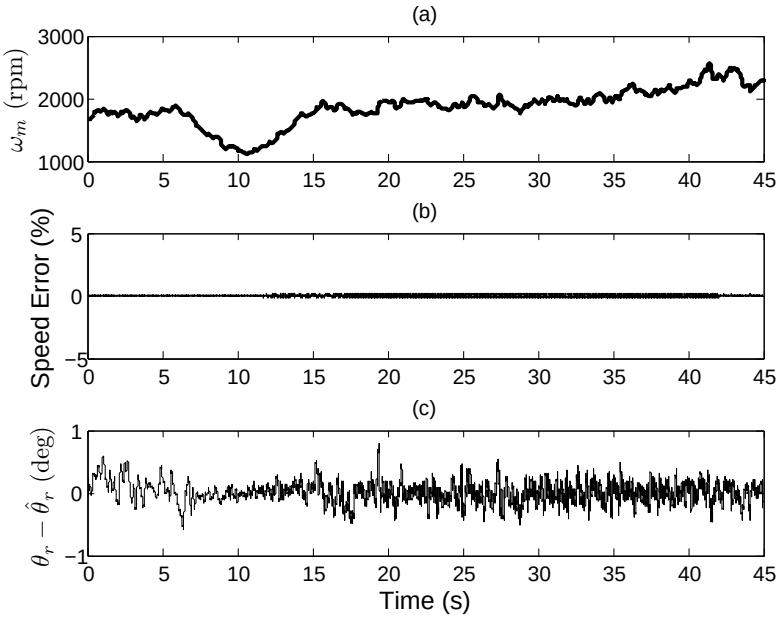

Figure 3.29 Actual and estimated rotor speeds and positions.

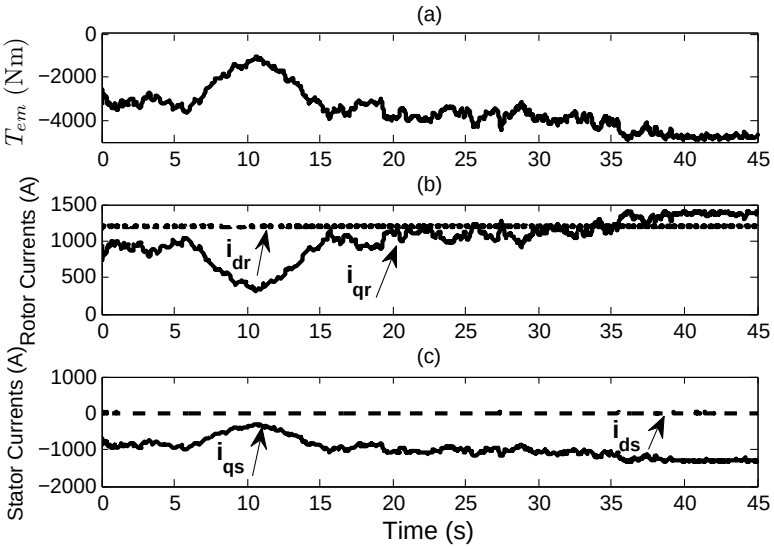

Figure 3.30 Electromagnetic torque and currents.

speed such that the maximum active power can be extracted from the wind and transferred to the grid.

The active and reactive powers of the DFIG are shown in Figure 3.28. It can be clearly seen that rotor power P_r flows from the grid to the DFIG at subsynchronous speeds and it flows in the opposite direction at supersynchronous speeds. P_{grid} is the actual power delivered to the grid. Note that all powers at the DFIG output side have relatively smoothed values compared with the discontinuous mechanical input power in Figure 3.27 due to wind gusts. The stator reactive power is regulated at around zero.

The DFIG rotor speed and estimation errors of the speed and position are shown in Figure 3.29. The estimated speed is very close to the actual speed during this fast transient process with the speed error of less than 2% and the position error of less than 1 degree.

The electromagnetic torque and various currents are plotted in Figure 3.30. It can be observed that T_{em} and i_{qs} are proportional to i_{qr} because of the stator-flux-orientation.

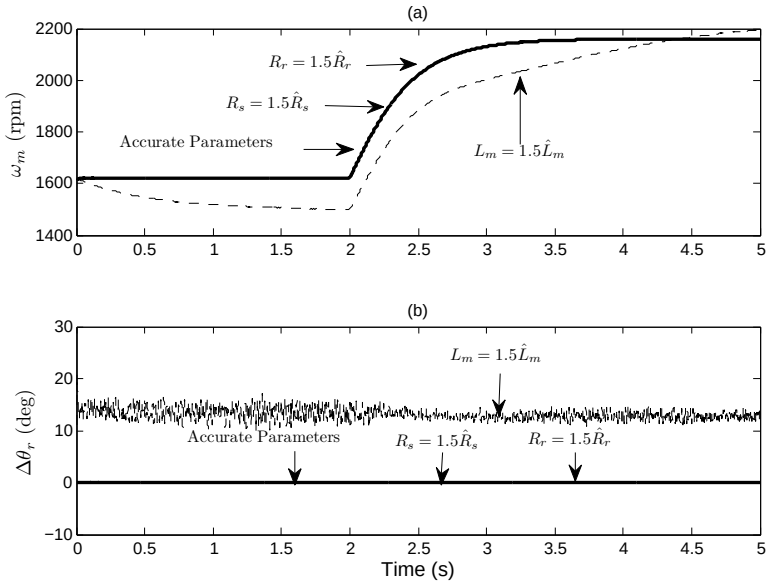

Figure 3.31 Parameter variation effects for the open-loop estimator [10] and MRAS observers [14]: (a) Rotor mechanical speed; (b) Rotor electrical angle error. Solid line corresponds to the case without parameter mismatch, dashed line to L_m mismatch, dotted line to R_s mismatch, and dashed-dotted line to R_r mismatch.

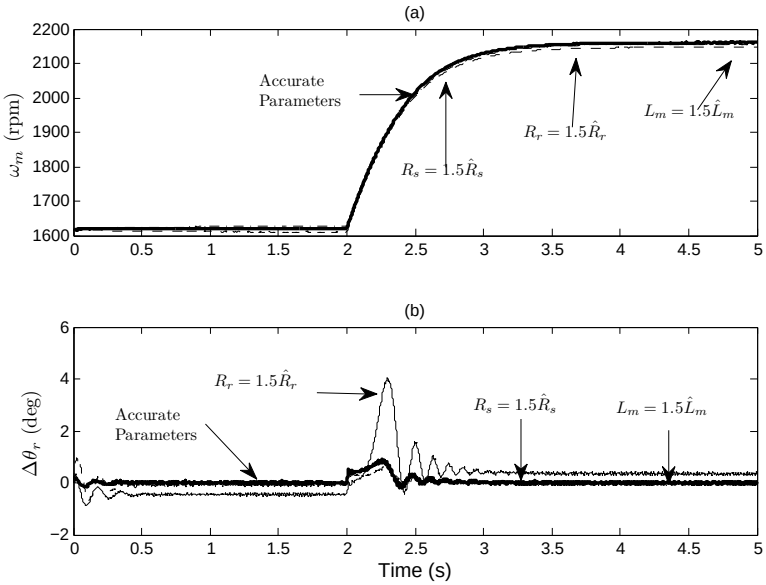

Figure 3.32 Parameter variation effects for the proposed speed-adaptive reduced-order observer: (a) rotor mechanical speed; (b) rotor electrical angle error. Solid line corresponds to the case without parameter mismatch, dashed line to L_m mismatch, dotted line to R_s mismatch, and dashed-dotted line to R_r mismatch.

3.5.3 Parameter Sensitivity

In this simulation study, the effects of parameter variations on the sensorless controlled DFIG-based wind turbine using different estimation approaches are investigated. Note that the implementation of the observer in all simulation studies in this section has the "closed-loop" manner which means the estimated rotor speed and position are used as feedback variables in the sensorless control system. The wind speed is assumed to be 9 m/s initially and increases to 12 m/s at $t = 2$ s. Therefore, the rotor speed of the DFIG is supposed to gradually increase from 0.9 pu to 1.2 pu. Effects of various types of parameter variations including the mismatch of stator resistance, rotor resistance, and mutual inductance, are investigated. When parameter mismatch occurs, only the situation where the actual parameter of the DFIG is larger than its nominal value used in the control system is examined because this happens more likely in reality. The parameter mismatch is assumed to occur at $t = 0$. The results are organized in Figure 3.31 and Figure 3.32. In Figure 3.31, it can be observed that both open-loop estimators

and MRAS observers are sensitive to the mutual inductance mismatch. The rotor electrical angle error are 15 degrees when the actual mutual inductance is 50% larger than its norminal value. Moreover, the rotor speed is not able to keep the tip-speed-ratio at its optimal value, resulting in a low energy capture. On the contrary, it can be shown from Figure 3.32 that there are no significant errors on the rotor speed in both transients and steady-state conditions even with parameters of 50% mismatch. In the case of rotor resistance mismatch, the estimated rotor angle has relatively the largest transients when the speed begins to increase and converges to the steady-state value with the error of less than 0.5 degree. Therefore, the proposed speed-adaptive reduced-order observer is the most robust approach for sensorless vector control of DFIG-based variable-speed wind turbines.

3.5.4 Speed Catching and Grid Synchronization

The last simulation study demonstrates the speed catching capability of the proposed sensorless controller during the grid synchronization. The grid synchronization is actually a start-up procedure that wind turbines should follow if the turbine initially starts from the idle state or restarts in the wind above the cut-off speed. In the DFIG topology the stator is directly connected to the grid via circuit breakers. If the magnitude and frequency of the stator voltage and the grid voltage are different, i.e. voltages are not synchronized, before closing the circuit breakers, high transient voltages and currents are likely to occur in generator windings and cause overheating and insulation failure. Therefore, care must be taken during grid synchronization to avoid undesirable transient overvoltages and overcurrents. The primary goal of a start-up procedure is to reduce the stress of the electrical and mechanical components of a wind turbine.

In this simulation, grid synchronization is achieved by equalization among the induced open-circuit stator voltage and the grid voltage. There will be minimum transient voltages and currents if the stator circuit breaker closes in this circumstance. To induce the open-circuit stator voltage equal to the grid voltage, the generator controller must be able to catch the turbine speed on-the-fly and therefore provides accurate rotor angle information. It can be

seen from the real-time simulation results that the proposed sensorless controller can almost instantly lock to the correct rotor speed and angle. Also, the induced open-circuit stator voltages are immediately locked the grid voltages and no transients can be observed when closing the circuit breakers.

The rotor d- and q-axis current commands for synthesis of grid voltages are derived now. Expanding (3.1) and (3.3) in the stator-flux-oriented reference frame and substituting the synchronization condition $v_{ds} = 0$, $v_{qs} = V_{grid}$, and $i_{ds} = i_{qs} = 0$ (open stator before connection), we have the following rotor current command values

$$i_{dr}^{*} = \frac{V_{grid}}{\omega_e L_m} \tag{3.43}$$

and

$$i_{qr}^{*} = 0 \tag{3.44}$$

where V_{grid} is the peak value of the grid phase voltage. These two rotor current commands are used in Figure 3.3 to synthesize open-circuit stator voltages before connecting to the grid. After the completion of grid synchronization, the rotor current commands are switched back to the maximum power control mode.

Figure 3.33 to Figure 3.36 show the DFIG parameters in the entire start-up procedure. We assume the turbine has accelerated to the speed of 0.8 pu by the pitch control in the wind speed of 8 m/s. In addition, the dc-link capacitor has been charged to the nominal voltage level. At 0.8 second, the rotor-side converter is enabled to catch the speed of the spinning generator and induce open-stator voltages to synchronize with grid voltages, as shown in Figure 3.37 to Figure 3.40. At 3.85 second, the stator circuit breakers are closed. The DFIG-based wind turbine is now connected to the grid, as shown in Figure 3.41 to Figure 3.44. At 4.75 second, the objective of the rotor-side controller is switched from grid synchronization to decoupled P-Q control for maximum power point tracking, as shown in Figure 3.45 to Figure 3.48. At 5 second, the wind speed starts to increase from 8 m/s to the nominal value of 12 m/s.

From the above simulation results, it can be concluded that the start-up procedure can be smoothly completed by the proposed sensorless controller.

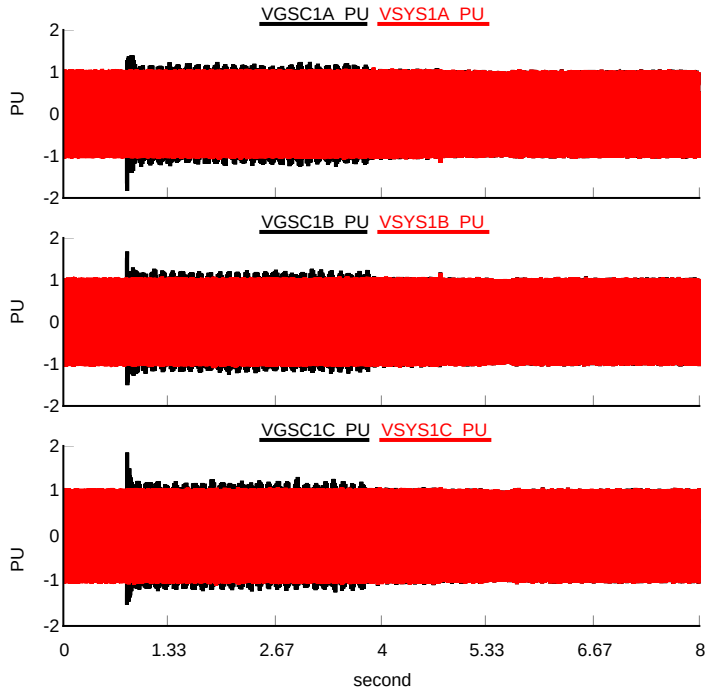

Figure 3.33 Stator and grid voltages in grid synchronization (0-8s).

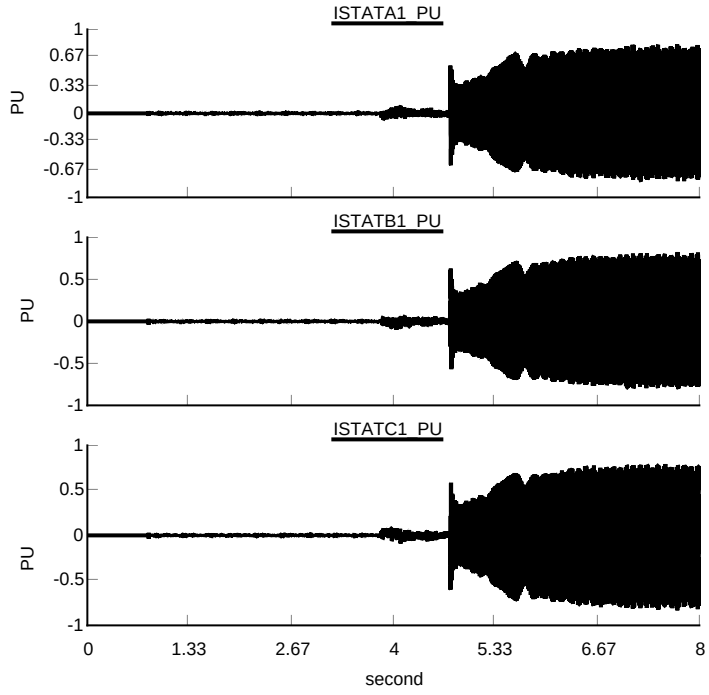

Figure 3.34 Stator currents in grid synchronization (0-8s).

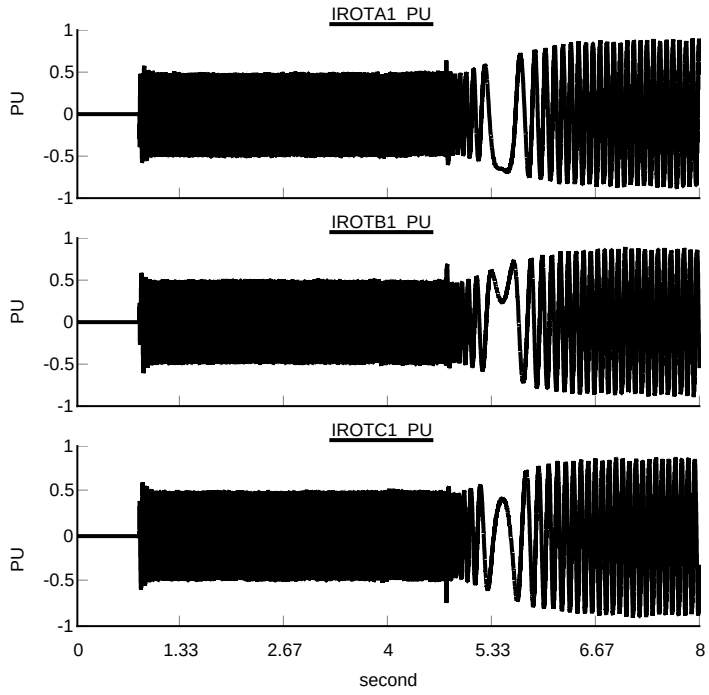

Figure 3.35 Rotor currents in grid synchronization (0-8s).

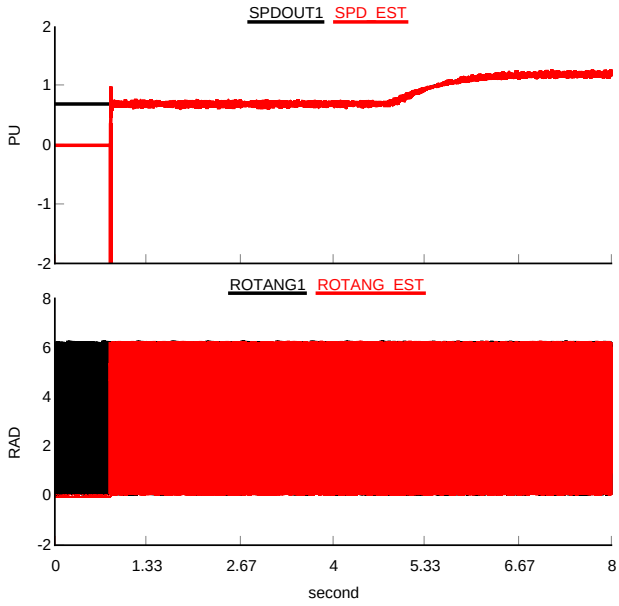

Figure 3.36 Real and estimated rotor speeds and angles in grid synchronization (0-8s).

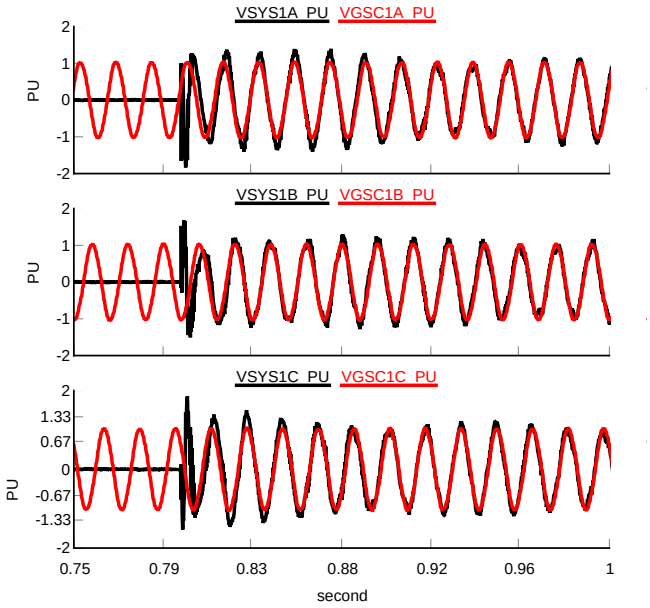

Figure 3.37 Detailed view of stator and grid voltages at 0.8 second (speed catching and grid voltage synchronization).

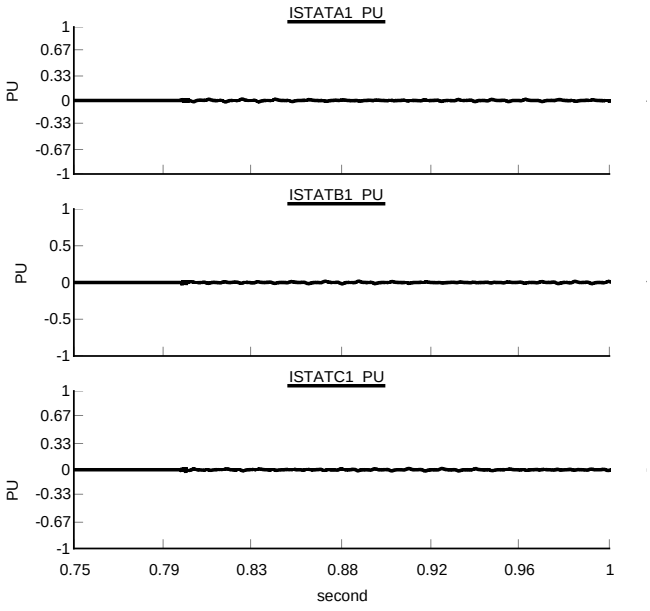

Figure 3.38 Detailed view of stator currents at 0.8 sec (speed catching and grid voltage synchronization).

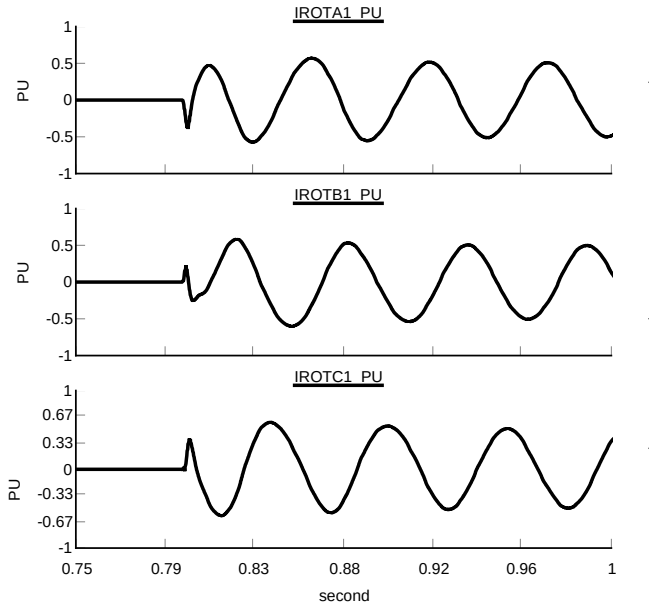

Figure 3.39 Detailed view of rotor currents at 0.8 second (speed catching and grid voltage synchronization).

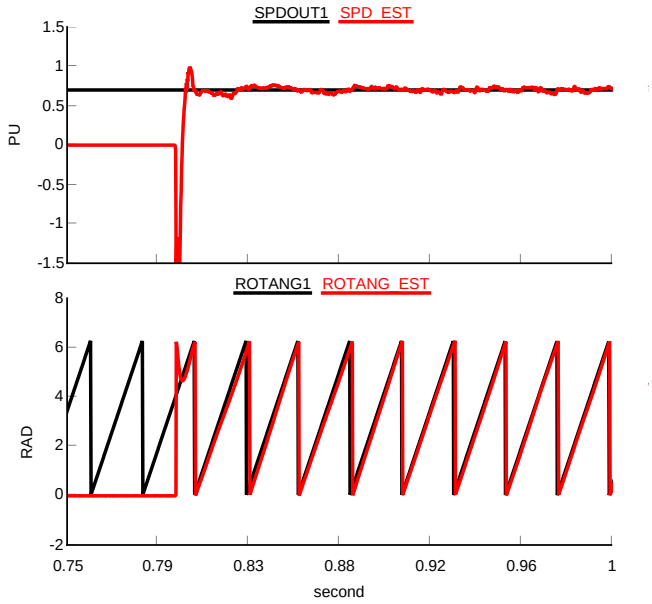

Figure 3.40 Detailed view of real and estimated rotor speeds and angles at 0.8 second (speed catching and grid voltage synchronization).

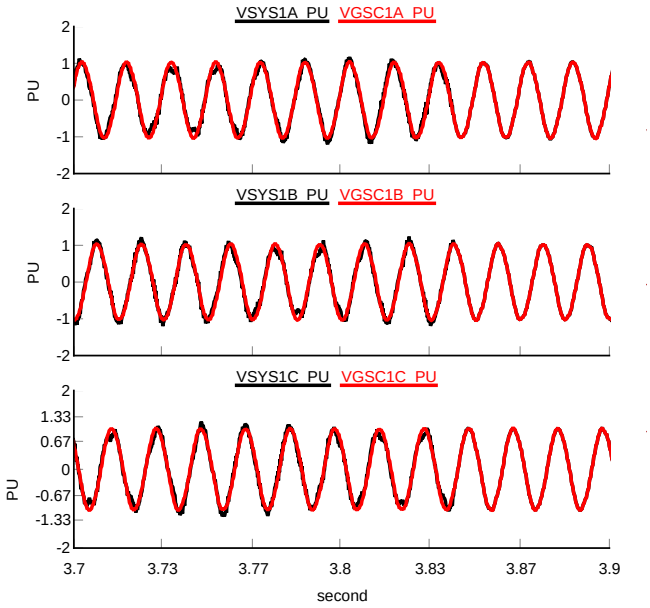

Figure 3.41 Detailed view of stator and grid voltages at 3.85 second (stator circuit breaker closing and grid connection).

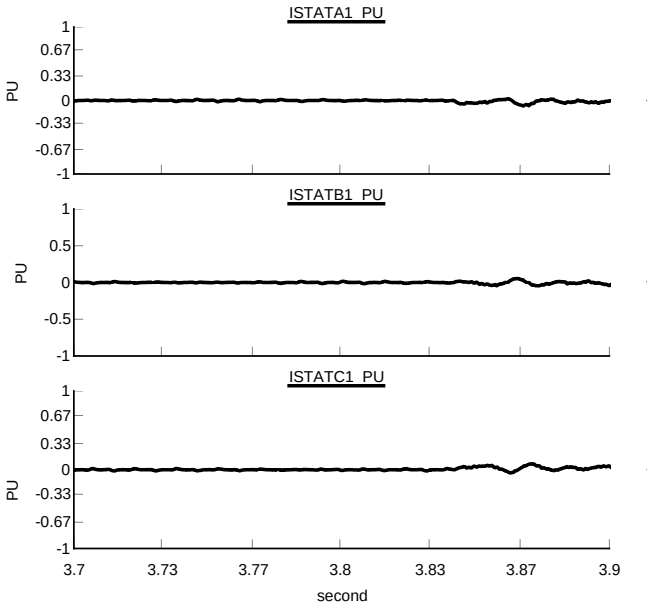

Figure 3.42 Detailed view of stator currents at 3.85 sec (stator circuit breaker closing and grid connection).

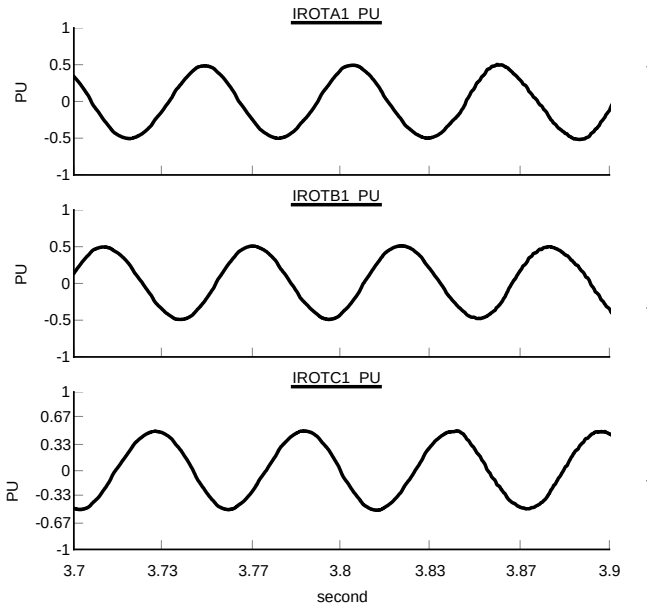

Figure 3.43 Detailed view of rotor currents at 3.85 second (stator circuit breaker closing and grid connection).

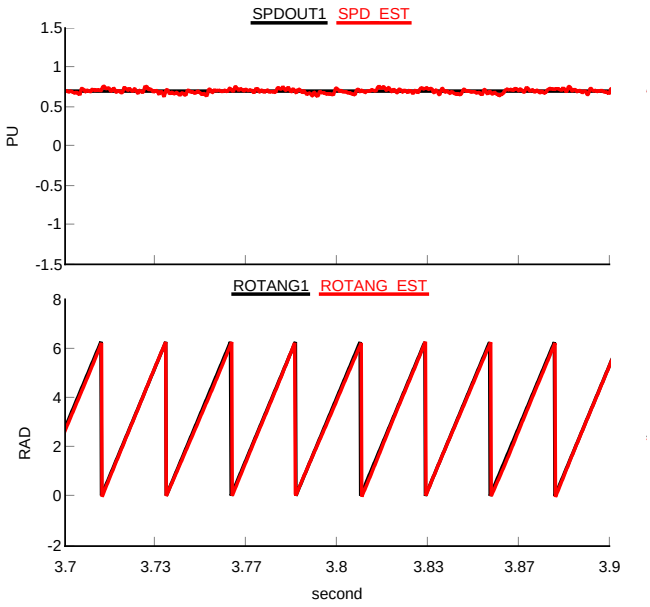

Figure 3.44 Detailed view of real and estimated rotor speeds and angles at 3.85 second (stator circuit breaker closing and grid connection).

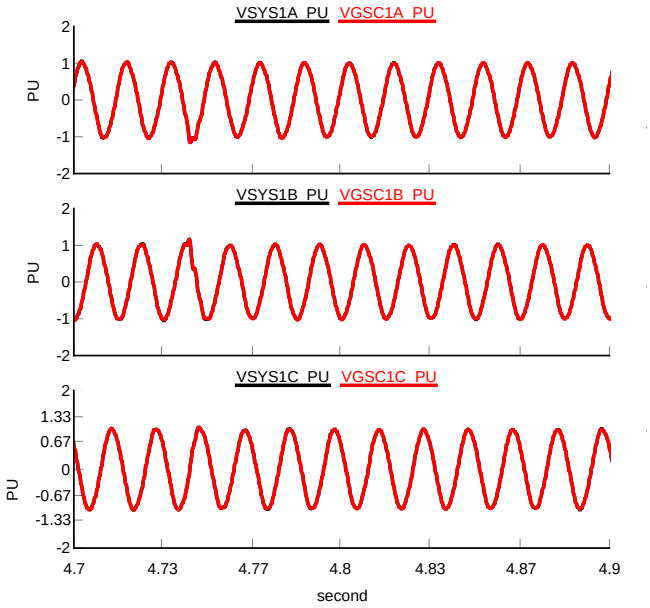

Figure 3.45 Detailed view of stator and grid voltages at 4.75 second (control objectives switched from grid synchronization to MPPT).

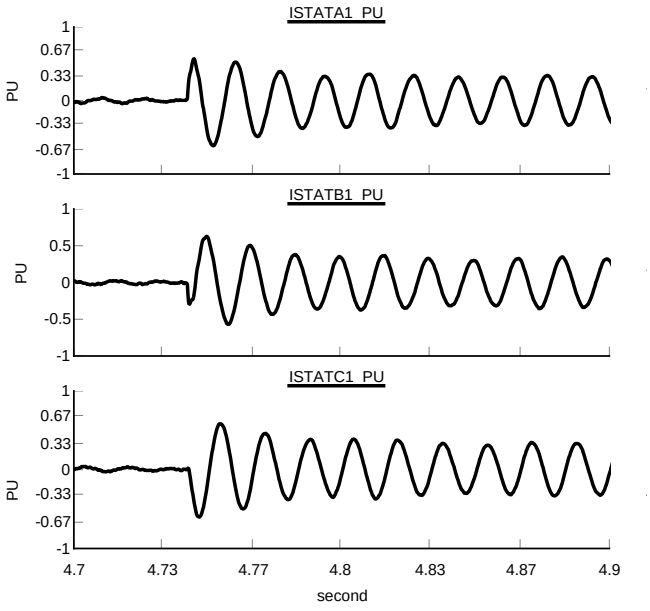

Figure 3.46 Detailed view of stator currents at 4.75 sec (control objectives switched from grid synchronization to MPPT).

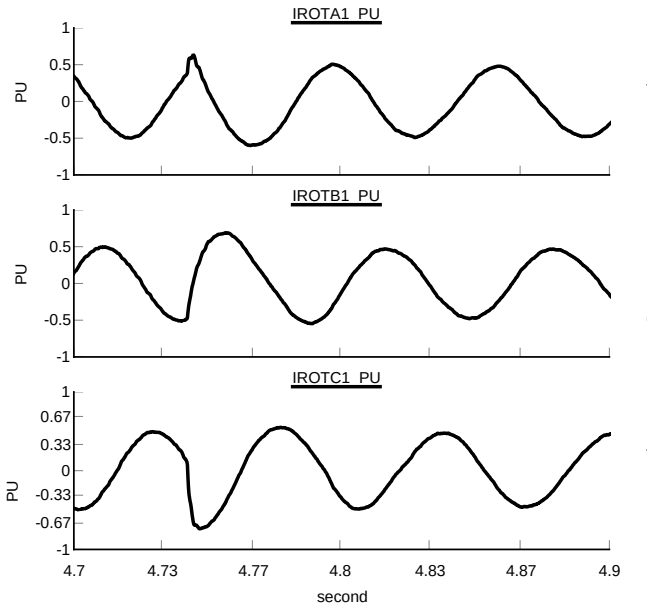

Figure 3.47 Detailed view of rotor currents at 4.75 second (control objectives switched from grid synchronization to MPPT).

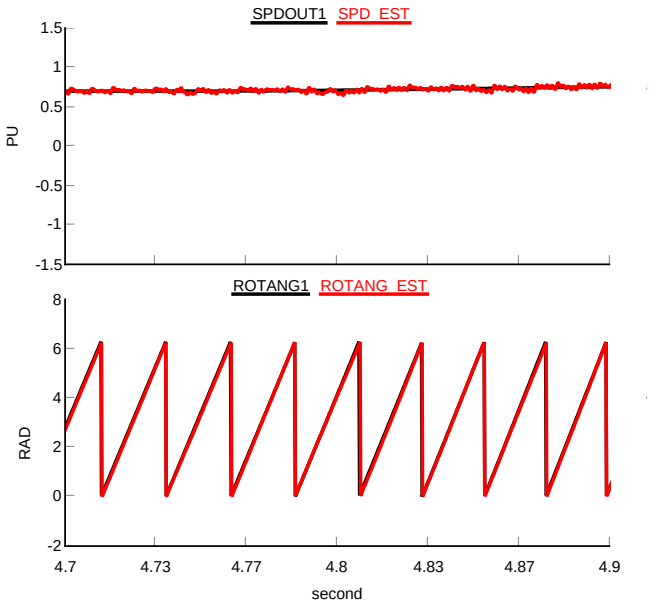

Figure 3.48 Detailed view of real and estimated rotor speeds and angles at 4.75 second (control objectives switched from grid synchronization to MPPT).

CHAPTER 4. MODELING OF PMSG-BASED WIND TURBINES FOR REAL-TIME SIMULATION

4.1 Introduction

The usage of MW-size variable-speed wind turbines as sources of energy has increased significantly during the last decade [2]. Advantages over fixed-speed wind turbines include more efficient wind power extraction, reduced grid power fluctuation, and improved grid reactive power support. There exist two major types of generation systems for VSWTs. One is the doubly-fed induction generator (DFIG) with a partial-scale power electronic converter. With the continuous price decreasing in power semiconductor devices, the PMSG with a full-scale power electronic converter has received increased attention in variable-speed wind turbine applications [46]-[52]. The PMSG-based VSWT has higher efficiency in energy conversion and suffers less from grid faults. However, the system cost will be dominated by the generator with increased pole numbers and elimination of the gearbox, which is also known as a multi-pole direct-driven PMSG [62]. Therefore, a PMSG-based VSWT with a multiple-stage gearbox is studied in this research for it is a good trade-off between the cost and performance. The bottom part of Figure 1.3 shows the general system scheme.

4.2 PMSG-Based Wind Turbine Model

A complete system model as well as the simulation platform setup is shown in Fig.2.6. The model consists of wind aerodynamics, the two-mass turbine drive train, a PMSG, a back-to-back voltage-source converter, and electrical and mechanical controllers. In this section, modeling of the following components will be described:

- Permanent magnet synchronous generator;
- Voltage source converter controller;
- Wind turbine;
- Drive train;
- Pitch angle controller.

4.2.1 PMSG Model

Table 4.1 PMSG Electrical Data (on Machine MVA Base)

MVA Base	3.0 [MVA]
Norminal Power	2.5 [MW]
Norminal Voltage (L-L RMS)	690 [V]
Norminal Frequency	60 [Hz]
Direct- and Q-axis Magnetic Inductances	0.15 [pu]
Stator Resistance	0.01 [pu]
Flux Linkage established by Magnet	1.0 [pu]
Pole Pairs	1

The detail description and model equation derivation of PMSGs can be found in most power system and electric machine references [37] [53]. The following assumptions are made in the PMSG model used in this research:

- The back electromotive forces (back-EMF) established by the permanent magnets in the stator is sinusoidal;
- No back-EMF voltage harmonics are modeled;
- The iron saturation effects are not modeled.

Generally, based on the above assumptions, the PMSG model can be described using following equations in the $d-q$ rotor reference frame:

$$\frac{d}{dt}i_{ds} = \frac{1}{L_d}v_{ds} - \frac{R_s}{L_d}i_{ds} + \frac{L_q}{L_d}\omega_r i_{qs} \tag{4.1}$$

$$\frac{d}{dt}i_{qs} = \frac{1}{L_q}v_{qs} - \frac{R_s}{L_q}i_{qs} - \frac{L_d}{L_q}\omega_r i_{ds} - \frac{\omega_r}{L_q}\psi_m \tag{4.2}$$

$$T_e = 1.5n_p\left[\psi_m i_{qs} + (L_d - L_q)i_{ds}i_{qs}\right] \tag{4.3}$$

$$\frac{d}{dt}\omega_r = \frac{n_p}{J}\left(T_e - T_m\right) \tag{4.4}$$

$$\frac{d}{dt}\theta_r = \omega_r \tag{4.5}$$

where ψ_m is the flux linkage constant established by the magnet and n_p is the pole pairs. Other symbols follow the generic nomenclature for electric machines. Machine parameters used for the PMSG model are listed in Table 4.1 [54].

4.2.2 PMSG Model Implementation in RTDS

A PMSG model is developed in the RTDS environment based on the above machine equations for real-time simulation. Since the PMSG model has to interact with the power system network solver in RTDS, it is developed as a "power system" model using CBUILDER, which is a part of the RSCAD software package distributed by RTDS. For the compatibility with other build-in real-time simulation models in RTDS, the trapezoidal rule, as shown in (4.6) is applied to the model equations for the numerical integration with a 50-μs step-size [55].

$$\int_a^b f(x)dx \approx (b-a)\frac{f(a)+f(b)}{2} \tag{4.6}$$

In each simulation time step, the user-written PMSG model reads the stator voltages in the previous simulation time step from the RTDS power system network solver, calculates internal machine variables such as the torque, speed, and rotor angle, and injects stator currents into the RTDS power system network for the current simulation time step. The procedures are listed as follows:

1. Calculate the d-q axis stator voltages v_{ds}, v_{qs} in the previous time step t_0 using known rotor angle θ_r.

$$\begin{bmatrix} v_{ds}^{t_0} \\ v_{qs}^{t_0} \end{bmatrix} = T_{3to2}(\theta_r^{t_0}) \begin{bmatrix} v_{as}^{t_0} \\ v_{bs}^{t_0} \\ v_{cs}^{t_0} \end{bmatrix} \tag{4.7}$$

where

$$T_{3to2}(\theta_r^{t_0}) = \frac{2}{3}\begin{bmatrix} \sin\theta_r^{t_0} & \sin\left(\theta_r^{t_0} - \frac{2}{3}\pi\right) & \sin\left(\theta_r^{t_0} + \frac{2}{3}\pi\right) \\ \cos\theta_r^{t_0} & \cos\left(\theta_r^{t_0} - \frac{2}{3}\pi\right) & \cos\left(\theta_r^{t_0} + \frac{2}{3}\pi\right) \end{bmatrix}.$$

2. Calculate the electromagnetic torque T_e in the previous time step t_0 using (4.3) and assign the value to the electromagnetic torque in the previous time step t_1.

3. Apply (4.6) to (4.4) and solve for the rotor angular speed ω_r in the current time step t_1.

$$\omega_r^{t_1} = \omega_r^{t_0} + \frac{\Delta t}{2}\frac{n_p}{J}(T_e^{t_1} + T_e^{t_0}) - \Delta t\frac{n_p}{J}T_m. \tag{4.8}$$

4. Apply (4.6) to (4.5) and solve for the rotor angle θ_r in the current time step t_1.

$$\theta_r^{t_1} = \theta_r^{t_0} + \frac{\Delta t}{2}(\omega_r^{t_1} + \omega_r^{t_0}). \tag{4.9}$$

5. Calculate the d-q axis stator voltages v_{ds}, v_{qs} in the current time step t_1 similar to (4.7) using the updated rotor angle $\theta_r^{t_1}$.

6. Apply (4.6) to (4.1) and (4.2) and solve for the stator currents i_{ds}, i_{qs} in the current time step t_1. The details are follows.

   Applying (4.6) to (4.1) and rearranging the equation such that all known history terms are placed on the right side, we have

$$a \cdot i_{ds}^{t_1} + b \cdot i_{qs}^{t_1} = y_1 \tag{4.10}$$

where

$$a = 1 + \frac{\Delta t}{2}\frac{R_s}{L_d}$$

$$b = -\frac{\Delta t}{2}\frac{L_q}{L_d}\omega_r^{t_1}$$

$$y_1 = \frac{\Delta t}{2}\frac{1}{L_d}(V_{ds}^{t_1} + V_{ds}^{t_0}) + \left(1 - \frac{\Delta t}{2}\frac{R_s}{L_d}\right) i_{ds}^{t_0} + \frac{\Delta t}{2}\frac{L_q}{L_d}\omega_r^{t_0} i_{qs}^{t_0}.$$

   Similarily, we have another equation from (4.2)

$$c \cdot i_{ds}^{t_1} + d \cdot i_{qs}^{t_1} = y_2 \tag{4.11}$$

where

$$c = \frac{\Delta t}{2}\frac{L_d}{L_q}\omega_r^{t_1}$$

$$d = 1 + \frac{\Delta t}{2}\frac{R_s}{L_q}$$

$$y_2 = \frac{\Delta t}{2}\frac{1}{L_q}(V_{qs}^{t_1} + V_{qs}^{t_0}) + \left(1 - \frac{\Delta t}{2}\frac{R_s}{L_q}\right) i_{qs}^{t_0} - \frac{\Delta t}{2}\frac{L_d}{L_q}\omega_r^{t_0} i_{ds}^{t_0} - \frac{\Delta t}{2}\frac{\psi_m}{L_q}(\omega_r^{t_1} + \omega_r^{t_0}).$$

Therefore, $i_{ds}^{t_1}, i_{qs}^{t_1}$ can be easily solved from (4.10) and (4.11).

7. Calculate three-phase stator currents i_{as}, i_{bs}, i_{cs} to be injected into the RTDS power system network solver for the network solution in the current time step t_1.

8. Update all the internal variables $t_0 \Rightarrow t_1$ for the next simulation time step and go back to step 1.

4.2.3 Voltage Source Converter Controller

As shown in Figure 2.6, the power electronics interface between the PMSG and grid is a back-to-back voltage source converter consisting of twelve fully controllable power semiconductor devices, i.e. Insulated-Gate Bipolar Transistors (IGBTs). The machine-side converter (MSC) functions as a rectifier converting ac power generated by the wind generator into dc power, while the grid-side converter (GSC) functions as an inverter converting dc power into ac power to be transferred into the grid. Both controllers employ a cascaded structure with a current-control inner loop and a power/var/voltage-control outer loop [54]. A detail controller scheme is shown in Figure 4.1.

The tasks of the GSC controller are to regulate the dc-link voltage and generate desired reactive power for the grid. While in the MSC controller, the power transferred to the grid P_{grid} is controlled by the q-axis current component. The d-axis current component is set at zero to maximize the torque control range and minimize resistive losses [49]. The reference generator speed is 1 pu for the power level above 0.75 pu. When the power is below 0.75

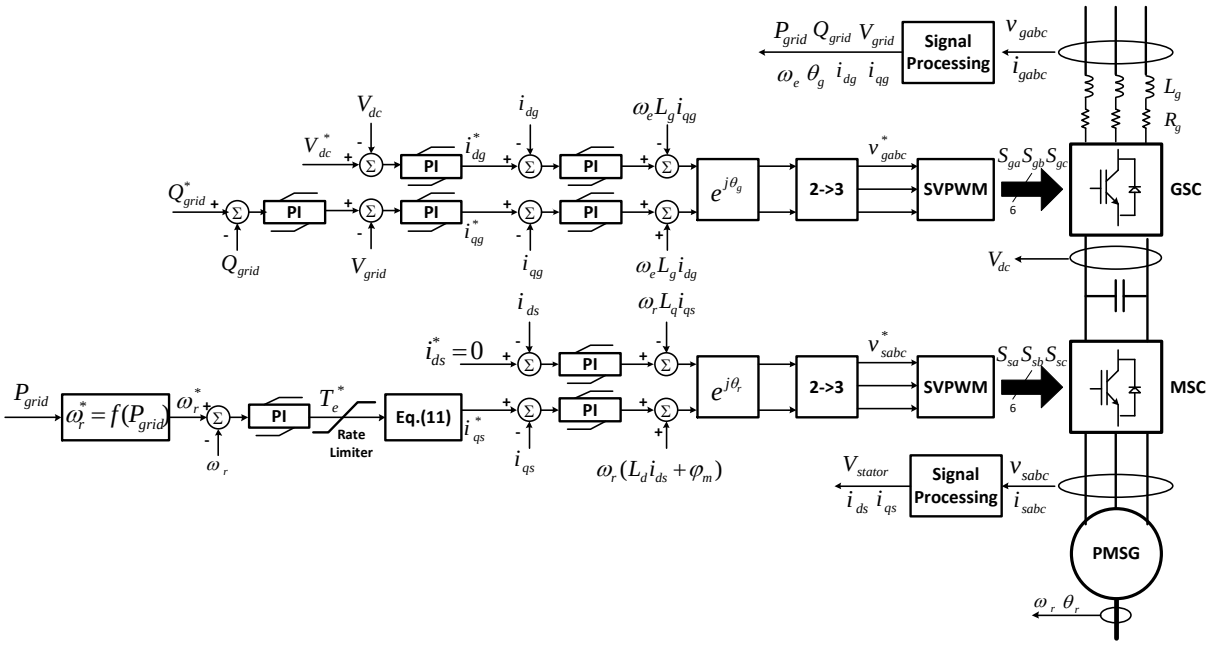

Figure 4.1 Back-to-back voltage source converter controller scheme.

pu, the following optimal speed-power tracking curve will be used for computing the reference speed in pu:

$$\omega_r^* = 1.1\sqrt[3]{P_{grid}}, \text{ for } P_{grid} < 0.75 \text{ pu}. \tag{4.12}$$

Derivation of the optimal tracking curve is presented in the next sub-section.

The PMSG is assumed to be non-salient in this study. Therefore, its d- and q-axis inductances are equal, i.e. $L_d = L_q$. Following (4.3), the q-axis reference current is calculated by:

$$i_{qs}^* = \frac{T_e^*}{1.5 n_p \psi_m}, \tag{4.13}$$

where the reference electromagnet torque T_e^* is obtained from the rotor speed PI controller.

The converter current limits in both controllers are set to 1.1 pu. The q-axis current in the MSC controller controlling the wind turbine power and the d-axis current in the GSC controlling the dc-link voltage have higher priorities if current limits are exceeded. Reference voltages are generated by the corresponding current PI controllers and some compensation terms are added to increase the PI controller performance. Firing pulses are produced using

space vector pulse-width modulation (SVPWM). Thus, the dc-link voltage can be expressed based on the ac voltages at either side by:

$$V_{dc} = \frac{V_{nom} * \sqrt{2}}{m} \tag{4.14}$$

where $0 < m < 1$ is the SVPWM index and V_{nom} is the ac-side nominal line-to-line RMS voltage. The steady-state dc-link voltage is chosen to be 1.2 kV and $m \approx 0.8$ for the nominal operating point.

The overall control scheme is developed in Matlab/Simulink with dSPACE real-time interface for the implementation on dSPACE real-time hardware.

4.2.4 Wind Turbine

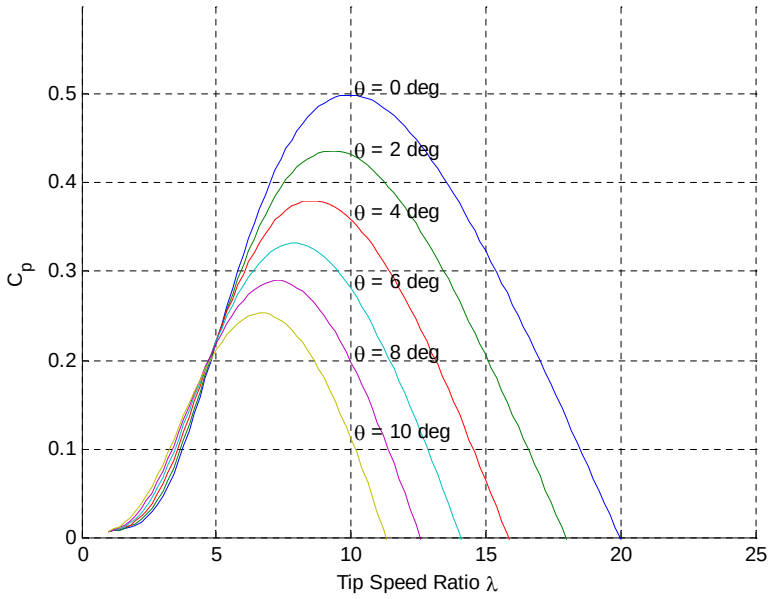

Figure 4.2 Power coefficient C_p characteristic.

The relation between wind speed v_w and mechanical power P_m extracted from the wind is given by [2]:

$$P_m = \frac{1}{2}\rho\pi R^2 C_p(\lambda, \theta) v_w^3 \tag{4.15}$$

where $\lambda = \frac{\omega_T R}{v_w}$ is the tip speed ratio, $C_p(\lambda, \theta)$ is the power coefficient, θ is the blade angle, ρ is the air density, and R is the turbine blade radius. The power coefficient $C_p(\lambda, \theta)$ is shown

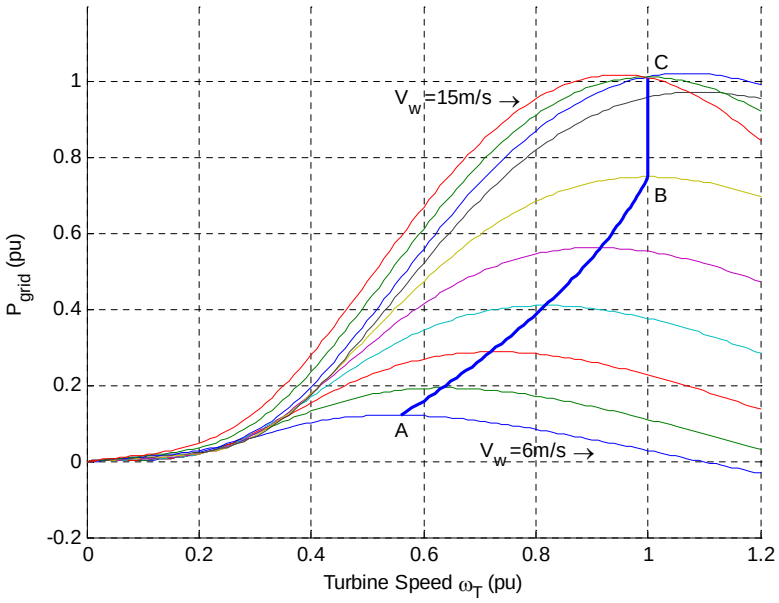

Figure 4.3 Wind Turbine Characteristic (wind speed decreases by step of 1 m/s).

in Appendix B.

The turbine characteristic is plotted in Figure 4.3. The turbine is operating at the maximum power tracking mode in region $A - B$ and the constant speed mode in region $B - C$. At the operating point B, we have the turbine power output $P_0 = 0.75$ pu, wind speed $v_{w0} = 11$ m/s and turbine speed $\omega_{T0} = 1.0$ pu. From (4.15), in the maximum power tracking region, mechanical power is proportional to the cube of the wind speed:

$$P_m = K_{wt} v_w^3, \tag{4.16}$$

and the tip speed ratio is kept at its maximum value λ_{max} such that:

$$v_w = \frac{R}{\lambda_{max}} \omega_T. \tag{4.17}$$

By solving constants K_{wt} and R from the operating point $(P_0, v_{w0}, \omega_{T0})$ and substituting (4.17) into (4.16), the power-speed tracking curve (4.12) is obtained, if $\omega_T \approx \omega_r$ is assumed in pu.

The wind turbine model is implemented in RTDS as a "control system" model.

4.2.5 Drive Train

A standard two-mass drive train [2] is modeled to represent the shaft system dynamics. In this model, the entire wind turbine mechanical system inertia is represented by two rotating masses. They are coupled by a shaft with finite stiffness. This model is useful if the shaft torsional oscillation need to be studied. The drive train data used in the model is listed in Table 4.2. The two-mass drive train model is implemented in RTDS as a "control system" model.

Table 4.2 Two-Mass Drive Train Data (on Machine MVA Base)

Inertia constant of Wind Turbine	2.8 [s]
Inertia constant of Generator	0.68 [s]
Shaft Spring Constant	3.22 [pu]
Shaft Mutual Damping	1.25 [pu]

4.2.6 Pitch Angle Controller

The wind turbine blade pitch angle controller is only activated at high wind speeds. In such circumstances, the pitch angle is adjusted to modify wind aerodynamics through the turbine rotor and limit power outputs. As seen from Figure 4.4, a negative feedback path is established by comparing the rotor speed and power output to their reference values. The blade pitch angle command is generated from combined outputs of two PI controllers. Note that the pitch angle can only change at a relative slow rate. Therefore, a rate limiter and a low-pass filter is included in the controller.

4.3 Real-Time Simulation Results

A full PMSG-based VSWT model was developed and implemented on the real-time simulation platform as shown in Figure 2.6. The 2.5-MW wind turbine is connected to the distribution feeder by a 34.5/0.69-kV step-up transformer. The entire system is connected to the 230-kV transmission system via a 10-mile cable modeled as a lumped impedance. The SVPWM switch-

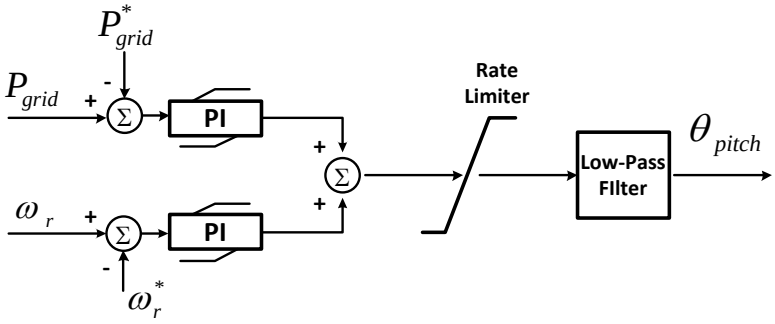

Figure 4.4 Blade pitch angle controller [54].

ing frequency for the back-to-back converter was 2 kHz. The grid power factor was controlled at unity in this simulation.

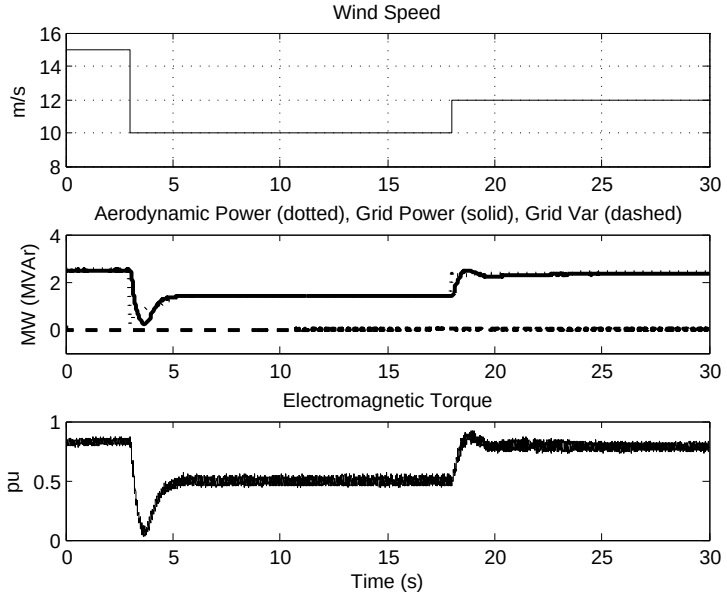

Figure 4.5 Turbine power and torque under stepwise-varying wind speed.

Firstly, a stepwise-varying wind speed was applied to the wind turbine. The wind speed suddenly dropped from 15 m/s to 10 m/s at 3.0 sec and rose to 12 m/s at 18 sec. The main wind turbine variables shown in Figure 4.5 and Figure 4.6 followed the change of the wind speed during the 30-sec period. The nominal wind turbine power (2.5 MW) was delivered to the grid before the wind disturbance. At 3.0 sec, the aerodynamic power dropped dramatically as the wind speed decreased due to the slow adjustment of the pitch angle. Consequently, the

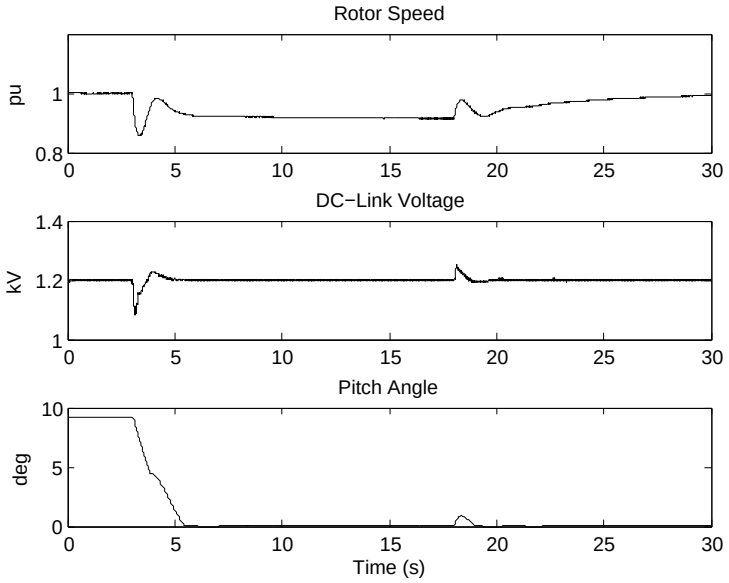

Figure 4.6 Turbine speed, dc voltage and pitch angle under stepwise-varying wind speed.

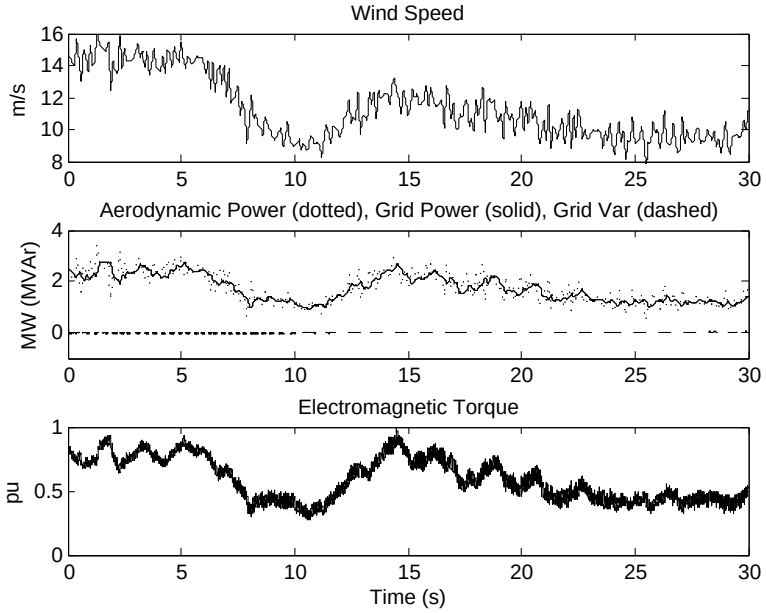

Figure 4.7 Turbine power and torque under randomly varying wind speed.

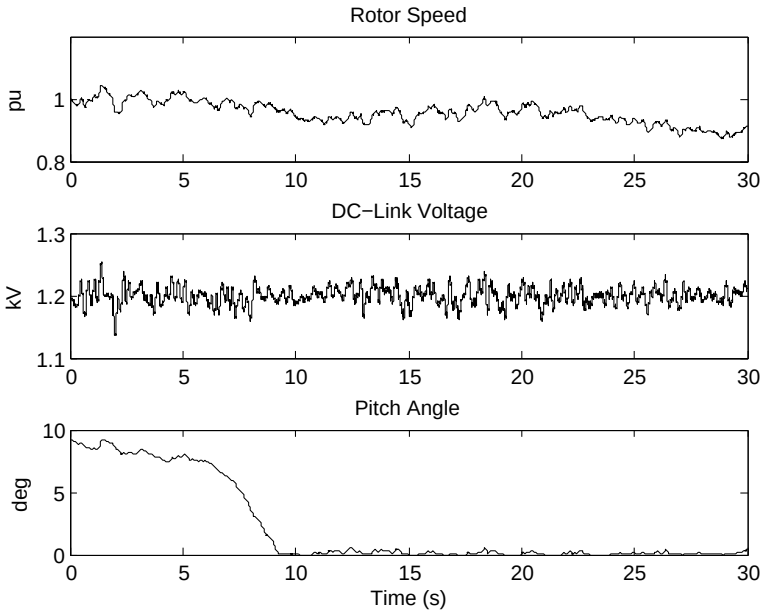

Figure 4.8 Turbine speed, dc voltage and pitch angle under randomly varying wind speed.

electromagnet torque was controlled to reduce the generator power outputs. There was a slight voltage dip on the dc-bus due to the instantaneous power unbalance at the moment of wind speed change. After the pitch angle was adjusted to the optimal value, which is zero in this situation, the system reached the steady state generating the power of 0.55 pu (1.4 MW) at the rotor speed of 0.9 pu under the wind speed of 10 m/s. This optimal operating point can be obtained from Figure 4.3 and (4.12). Reactive power was regulated to zero during the entire period as desired. The similar analysis can be applied to the turbine response after 18 sec.

Then, the model performance under a randomly varying wind speed was examined. The randomly varying wind speed was constructed using a simplified version of the method in [2]. As shown in Figure 4.7 and Figure 4.8, the wind speed fluctuated from the highest value of 16 m/s to the lowest 8 m/s. The aerodynamic power changed with the wind fluctuation, while the real power delivered to the grid varied much more smoothly. This can probably be attributed to the energy storage characteristic of the turbine inertia and dc-bus capacitor. The dc-link voltage was regulated at the constant level to support the ac power conversion despite of small fluctuations.

CHAPTER 5. IMPROVED GRID FAULT RIDE-THROUGH STRATEGIES FOR VARIABLE-SPEED WIND TURBINES

5.1 Introduction

The increasing penetration of wind power generation facilities has made it necessary to revise the existing grid code (GC) requirements to include specific requirements regarding the operation of wind power generators. It has been greatly recognized that wind turbine should remain connected to the grid in case of grid disturbances for a specific period of time to support the system voltage recovery. Such requirements are known as the fault ride-through (FRT) capability. At present, new GCs in most countries have included the FRT requirement for grid connected wind turbines to remain connected to the network without tripping when subject to a specific voltage sag profile. The specific voltage sap profile is determined by the depth and clearance time. In US, as mandated by the Federal Energy Regulatory Commission (FERC) Order 661-A wind farms are to remain online in the presence of severe voltage disturbances as low as 0.0 pu for up to 9 cycles (150 ms), as shown in Figure 5.1.

DFIG and PMSG are the main wind generators installed in the power system nowadays. DFIG-based wind turbines are very sensitive to voltage dips because its stator winding is directly connected to the grid. As it can be seen in the next section, the voltage drop in the stator windings produces a sudden change in the stator flux of the DFIG, which will induce overcurrents in the rotor windings due to the magnetic coupling [57]. These overcurrents, which can be seven to ten times the nominal value of currents [58], can easily damage the motor windings and the power semiconductors of the rotor-side converter. This is more critical considering the fact that the rotor-side converter is only sized about 30% of the nominal rating of the DFIG.

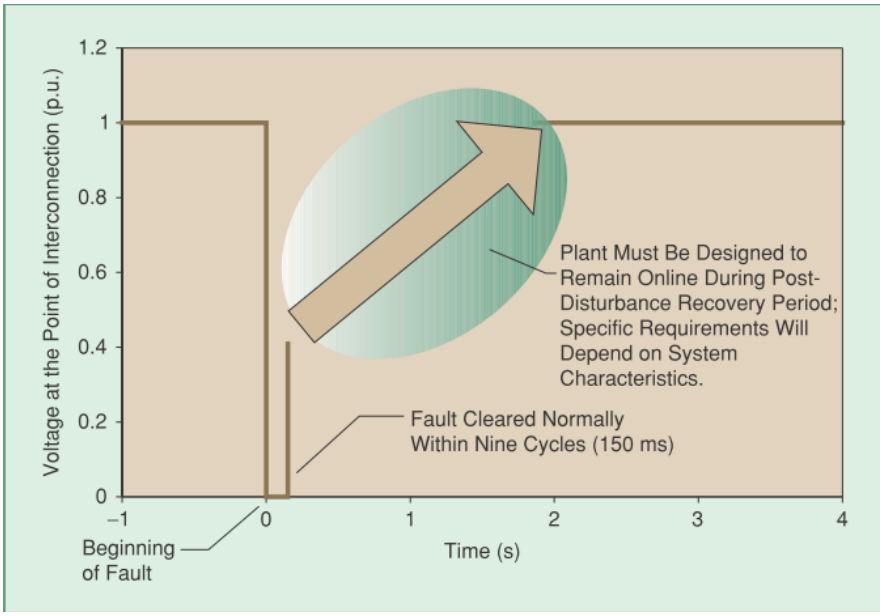

Figure 5.1 FERC Order 661A requires wind generators to remain connected for voltage as low as zero lasting for up to nine cycles (source: [56]).

Many studies have been carried out in order to improve the FRT capability of DFIG-based wind turbines. The most widely used solution is based on a protective circuit connected to the rotor windings known as crowbar [59]. This equipment consists of a bank of resistors that are connected to the rotor windings via power semiconductors, such as thyristors or GTOs/IGBTs. In this way, the rotor windings can be connected to the resistors when a grid fault occurs. Therefore, the induced high rotor current flows through the resistors instead of the rotor-side converter. Crowbars equipped with thyristors are known as passive crowbars while those equipped with GTOs/IGBTs are know as active crowbars. The active crowbars shown in Figure 5.2 allow almost instant connection and disconnection to the rotor windings, enabling fast protection in the fault inception and resuming normal operation after the fault clearance.

Despite the fact that a crowbar circuit is able to reduce the current peaks in the fault inception, it permanently disconnects the rotor-side converter when the crowbar is active. The rotor windings are short-circuited through the crowbar resistors. Therefore, the DFIG

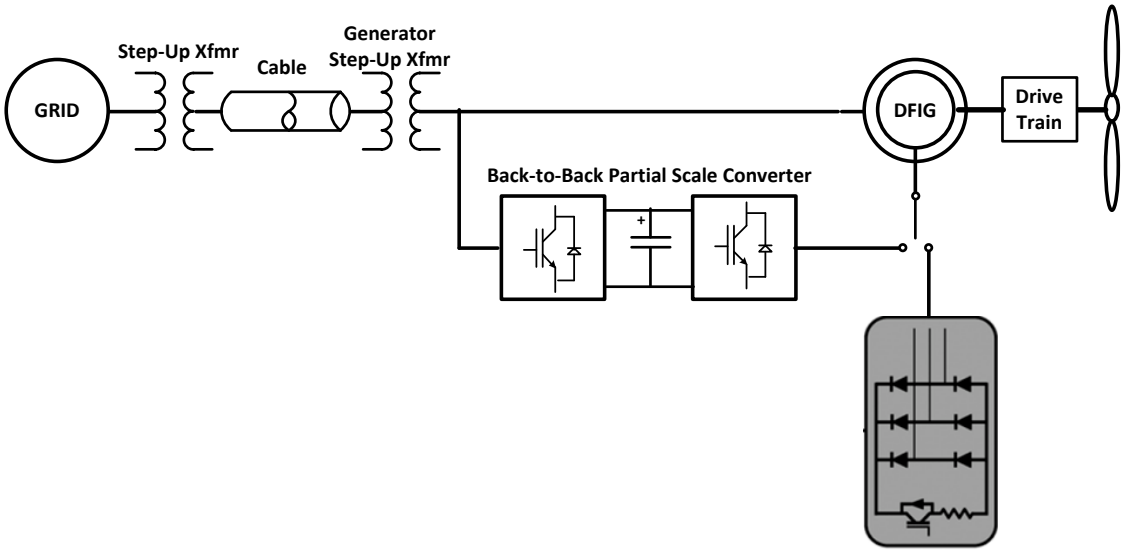

Figure 5.2 DFIG-based wind turbine with an active crowbar.

becomes a squirrel cage machine and the decoupled active and reactive power control can not be achieved. In other words, the DFIG is out of control when the crowbar is connected. This is not allowed under the new GCs because wind turbines are required to remain online during grid disturbances and collaborate in resuming normal operation of the grid. Moreover, overcurrents may be induced in the rotor windings again when the fault is cleared. The crowbar will be re-triggered in this situation, resulting in delay of resuming normal operation of the wind turbine.

Some researchers have proposed new FRT solutions to avoid permanent disconnection of rotor-side converter during the fault. In [60], it is proposed to inject a current into the rotor windings to counteract the natural stator flux induced by voltage dips. As can be seen from the analysis in the next section, the rotor overcurrent comes from the rotor overvoltage induced by the natural flux. The injected current can be considered as a demagnetizing current to weaken the effect of the stator natural flux on the rotor. Therefore, the rotor overcurrent can be reduced.

However, the demagnetizing method can not fully eliminate the rotor overcurrent during the first moment of a severe voltage dip. The reason is that the demagnetizing current required

to completely cancel the natural flux effect at that moment is usually several times of the nominal value, which exceeds the capability of the rotor-side converter. In this research, we have proposed a combined FRT solution where the crowbar is only triggered at the first moment of a fault while the demagnetizing current is injected immediately after the rotor current is lower than the converter limit. The demagnetizing current is able to accelerate the decay of rotor overcurrents during the fault. In this way, the rotor-side converter is only disconnected for a very short period of time and the DFIG can immediately resume normal operation to support grid voltage recovery.

Compare to the DFIG-based wind turbine, the PMSG-based wind turbine with a full-scale power converter inherently has better FRT capabilities because it is decoupled from the grid by the dc-link capacitor [62]. However, the dc-link capacitor is likely to be overcharged during grid disturbances and this will cause unacceptable overvoltages on the dc bus. Recently, a number of studies have been conducted to find hardware and software solutions for FRT strategies of PMSG-based VSWTs [63] [64] [65]. In [63], a state feedback linearization controller was proposed to limit the converter current levels. However, the controller parameters tuning appeared to be difficult and its performance was not fully tested. In [64], the authors proposed a combined hardware and software scheme using a breaking chopper and pitch angle control. However, the response of the pitch angle controller might not be fast enough for the FRT control. Hansen [65] modified reference variables for the wind turbine electrical controller to ride through grid faults without additional hardware. This approach requires a complete redesign of the controller structure and parameter tuning since previously decoupled controller variables are now coupled to each other. In this research, a straightforward software-only FRT approach to mitigate dc-link overvoltages is proposed and analyzed. This method ensures the dc-link voltage is kept within the acceptable range during grid faults and the voltage recovery stage.

5.2 Improved Grid Fault Ride-Through Strategy for DFIG-Based Wind Turbine

5.2.1 DFIG Behavior Under Voltage Dips

In the section, the DFIG behavior under three-phase voltage dips is briefly analyzed. It reveals the root cause of overvoltages and overcurrents generated on the rotor and enlightens the research of FRT solutions. The analysis in this section is based on [57].

5.2.1.1 Rotor Voltage

Starting from (3.1) and (3.2), the DFIG model in the stationary stator-oriented reference frame can be expressed as

$$\boldsymbol{v_s^s} = R_s \boldsymbol{i_s^s} + \frac{d\boldsymbol{\psi_s^s}}{dt} \tag{5.1}$$

$$\boldsymbol{v_r^s} = R_r \boldsymbol{i_r^s} + \frac{d\boldsymbol{\psi_r^s}}{dt} - j\omega_r \boldsymbol{\psi_r^s}. \tag{5.2}$$

The superscript s indicates the stationary stator-oriented reference frame is assumed. The stator and rotor fluxes have the same form as (3.3) and (3.4):

$$\boldsymbol{\psi_s^s} = L_s \boldsymbol{i_s^s} + L_m \boldsymbol{i_r^s} \tag{5.3}$$

$$\boldsymbol{\psi_r^s} = L_r \boldsymbol{i_r^s} + L_m \boldsymbol{i_s^s}. \tag{5.4}$$

From the flux equations, the stator current can be eliminated and the rotor flux can be expressed as

$$\boldsymbol{\psi_r^s} = \frac{L_m}{L_s} \boldsymbol{\psi_s^s} + \sigma L_r \boldsymbol{i_r^s} \tag{5.5}$$

where $\sigma = 1 - \frac{L_m^2}{L_s L_r}$. Therefore, from (5.2) and (5.5), the rotor voltage can be expressed as

$$\boldsymbol{v_r^s} = \underbrace{\frac{L_m}{L_s}\left(\frac{d}{dt} - j\omega_r\right)\boldsymbol{\psi_s^s}}_{\boldsymbol{v_{ro}^s}} + \left(R_r + \sigma L_r \left(\frac{d}{dt} - j\omega_r\right)\right)\boldsymbol{i_r^s}. \tag{5.6}$$

It can be seen that the first term in the rotor voltage equation (5.6) is related to the rotor voltage when the rotor is open-circuit. It is denoted by $\boldsymbol{v_{ro}^s}$ and it is due to the evolution of stator flux by magnetic coupling. The second term exists when the rotor is connected to an external circuit, e.g., the rotor-side converter or a crowbar.

5.2.1.2 Behavior in Normal Operation

In normal operation, the stator voltage space vector can be expressed as

$$\boldsymbol{v_s^s} = V_s e^{j\omega_s t} \tag{5.7}$$

where V_s is the constant amplitude and ω_s is the synchronous speed.

The stator flux can be expressed from the last equation and (5.1) neglecting the stator resistance R_s:

$$\boldsymbol{\psi_s^s} = \frac{V_s}{j\omega_s} e^{j\omega_s t}. \tag{5.8}$$

Therefore, the open-circuit rotor voltage $\boldsymbol{v_{ro}^s}$ can be expressed from (5.6), (5.7), and (5.8) by

$$\boldsymbol{v_{ro}^s} = \frac{L_m}{L_s}\frac{\omega_s - \omega_r}{\omega_s} V_s e^{j\omega_s t} = \frac{L_m}{L_s} s\boldsymbol{v_s^s} \tag{5.9}$$

where $s = \frac{\omega_s - \omega_r}{\omega_s}$ is the slip. The complete rotor voltage expression considering the rotor current can then be expressed as

$$\boldsymbol{v_r^s} = \boldsymbol{v_{ro}^s} + \left(R_r + \sigma L_r \left(\frac{d}{dt} - j\omega_r\right)\right) \boldsymbol{i_r^s}. \tag{5.10}$$

By multiplying $e^{-j\omega_r t}$, the voltage and current space vectors are transformed to the rotor reference frame. Thus, the rotor voltage in the rotor reference frame is obtained from the last equation

$$\boldsymbol{v_r^r} = \boldsymbol{v_{ro}^r} + R_r \boldsymbol{i_r^r} + \sigma L_r \frac{d\boldsymbol{i_r^r}}{dt} \tag{5.11}$$

where the superscript r indicates the rotor reference frame. A equivalent circuit for DFIG seen the rotor can be drawn as in Figure 5.3. From the equivalent circuit seen from the rotor, the

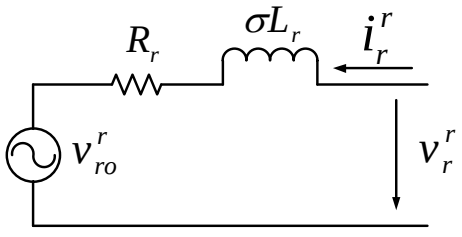

Figure 5.3 DFIG equivalent circuit seen from the rotor.

DFIG is equivalent to a voltage source due to the stator flux in series with the rotor resistance R_r and the transient rotor inductance σL_r.

In (5.11), the first term is related to the stator voltage and the second term is related to the rotor current. If the rotor is open-circuit, the rotor voltage, which is just $\boldsymbol{v_{ro}^r}$, is proportional to the slip frequency and the stator voltage. Even if the rotor is connected and the rotor current is present, since R_r and σL_r are usually very small, the total rotor voltage $\boldsymbol{v_r^r}$ is still dominated by $\boldsymbol{v_{ro}^r}$. Therefore, considering $|s| \leq 0.3$ in normal operation of a typical DFIG, the amplitude of rotor voltage usually does not exceed 30% of the nominal stator voltage.

5.2.1.3 Behavior under Voltage Dips

The DFIG behavior under a three-phase voltage dip is analyzed in this section. It is assumed that the generator operates at normal condition and a three-phase fault occurs in the grid at time $t = 0$ and causes a voltage dip from the initial amplitude V_0 to $V_1 (< V_0)$ at the stator windings

$$\boldsymbol{v_s^s} = \begin{cases} V_0 e^{j\omega_s t} & \text{for } t = 0^- \\ V_1 e^{j\omega_s t} & \text{for } t = 0^+ \end{cases} . \tag{5.12}$$

Firstly, the rotor is assumed open-circuit. From (5.1), the stator flux can be expressed as

$$\frac{d}{dt}\boldsymbol{\psi_s^s} + \frac{R_s}{L_s}\boldsymbol{\psi_s^s} = \boldsymbol{v_s^s}. \tag{5.13}$$

This is a first-order differential equation. Therefore, the stator flux can be easily solved by using the initial and final conditions in (5.12) as

$$\boldsymbol{\psi_s^s} = \frac{V_1}{j\omega_s} e^{j\omega_s t} + \frac{V_0 - V_1}{j\omega_s} e^{-t/\tau_s} \tag{5.14}$$

where $\tau_s = \frac{L_s}{R_s}$ is the stator time constant. The first term in the last equation is a rotational flux space vector corresponding to the grid voltage during the fault. The second term is a flux vector fixed to the stator and its amplitude decreases exponentially to zero by the stator time constant. These two terms can be considered as the forced flux and natural flux [57], or the positive and zero sequence flux during the fault.

The open-circuit rotor voltage $\boldsymbol{v_{ro}^{s}}$ can then be obtained by substituting (5.14) in (5.9). After transformation to the rotor reference frame by multiplying $e^{-j\omega_r t}$, it becomes

$$\begin{aligned}\boldsymbol{v_{ro}^{r}} &= \frac{L_m}{L_s}\left(sV_1 e^{j\omega_{sl}t} - \left(\frac{1}{\tau_s} + j\omega_r\right)\frac{V_0 - V_1}{j\omega_s}e^{-j\omega_r t}e^{-t/\tau_s}\right) \\ &\approx sV_1 e^{j\omega_{sl}t} - (1-s)(V_0 - V_1)e^{-j\omega_r t}e^{-t/\tau_s}\end{aligned} \tag{5.15}$$

where $\frac{1}{\tau_s} << \omega_r$ and $L_m \approx L_r$ are assumed. Therefore, the maximum rotor voltage is

$$V_{ro,max}^{r} \approx |s|\, V_1 + (1-s)(V_0 - V_1). \tag{5.16}$$

In the last equation, the first term is proportional to the slip frequency and the grid voltage during the fault. The second term is proportional to the rotor frequency and the depth of the voltage dip. Therefore, the maximum rotor voltage during the fault is dominated by the second term, especially when the DFIG operates at a supersynchronous speed in the pre-fault condition and the fault causes a deep voltage dip. Considering that a full voltage dip occurs when the DFIG is operating at the speed of 1.2 pu, the maximum rotor voltage could be 1.2 pu, which is four times the normal operation value according to (5.9). Such high voltage can easily result in breakdown of the insulation material of the rotor and the power semiconductors of the rotor-side converter.

Next the situation in which there are currents flowing through the rotor is considered. From Figure. 5.3, the rotor current is controllable only if the rotor-side converter is able to generate a voltage close to the voltage supply, which is the open-circuit rotor voltage in this case. However, the open-circuit rotor voltage can be as high as 1.2 pu of the stator voltage at the first moment of the fault, as shown in the previous analysis. This means the rotor-side converter has to be sized up to the stator rating, which loses advantages of the configuration of the DFIG-based wind turbine.

If the rotor-side converter is sized for its normal rating (around 30% of the stator rating), the rotor current will be uncontrollable at the beginning of the fault, and probably also at the fault clearance because of the sudden voltage rise. The transient onvercurrent will depend on the maximum voltage that can be generated by the converter and the rotor parameters. The rotor parameters such as the resistance R_r and transient inductance σL_r are ofter very

small. Therefore high overcurrents are likely to appear in the rotor windings. The approximate maximum stator and rotor currents have been derived in [58] and [66] as

$$i_{s,max} \approx \frac{1.8V_s}{\sqrt{X_s'^2 + R_{\text{ext}}^2}} \tag{5.17}$$

$$i_{r,max} \approx \frac{V_s}{(1-s)\sqrt{X_s'^2 + R_{\text{ext}}^2}} \tag{5.18}$$

where $X_s' = X_{s\sigma} + \frac{X_{r\sigma}X_m}{X_{r\sigma}+X_m}$ is the transient stator reactance. It is cleared that limiting rotor overcurrents requires connecting external impedances, e.g., the crowbar circuit.

5.2.2 Improved Fault Ride-Through Control

The crowbar circuit as shown in Figure 5.2 is the most common technique so far used to protect the rotor-side power electronic converter during voltage dips. The basic idea of the crowbar circuit is to bypass the rotor-side converter by short-circuiting the rotor of DFIG with an external resistor upon detection of a fault. Therefore, the rotor current will flow through the external resistor, protecting the converter from high transient currents.

When the crowbar circuit was initially introduced into wind turbines for protection, the power semiconductor devices connecting the resistance to the rotor are thyristors. With no gate turn-off capability, DFIG-based wind turbines with this type of "passive" crowbar circuit are not able to resume operation as soon as the transient current/voltage has decayed. This will prevent large wind farms from collaborating in resuming normal grid operation required by new GCs. Therefore, wind turbine manufacturers have developed the "active" crowbar circuit as shown in Figure 5.2 to improve the fault ride-through capability. It consists of a three-phase rectifier and a power semiconductor device with gate turn-off capability as well as an external resistor. The power semiconductor device can be a gate turn-off (GTO) thyristor or an insulated gate bipolar transistor (IGBT). The turn-on and turn-off time of these devices is usually several micro-seconds. Thus, The active crowbar circuit allows the instant connection and disconnection of a wind turbine to the grid, enabling fast protection and resuming of normal operation.

As mentioned in previous sections, the main disadvantage of the crowbar is that while it remains connected, the DFIG operates as a squirrel cage machine since the rotor is short circuited. The active and reactive power control is no longer available and and the DFIG absorbs reactive power from the grid when operating as a squirrel cage machine. This will further deteriorate the situation during a grid fault and slow down the fault recovery process or even result in voltage collapse. Thus, it is better to reduce the connection time of the crowbar and enable the wind turbine normal operation as soon as the transients have decayed. As can be seen from the analysis in the previous section, the difficulty of keeping the rotor-side converter connected during a voltage dip comes from the overvoltage induced by the natural flux in the rotor.

Recently, some researchers have proposed other fault ride-through techniques that do not require a crowbar circuit. Among them, a typical solution presented in [60] is to inject a current into the rotor that is opposite to the natural stator flux in order to weaken its effect on the rotor. It can be seen from (5.14) and (5.16) that the rotor overcurrents result from the natural stator flux component in the stator flux. Also (5.5) shows that the rotor current can be controlled to counter the undesired components in the stator flux. If the rotor currents are controlled to cancel the natural flux component in the stator flux, the rotor flux will decrease and there is little chance that overcurrents will exhibit. Therefore, the fault ride-through technique in [60] can be considered as the demagnetizing method.

However, the effectiveness of this demagnetizing method is limited by the fact that a very high demagnetizing current is required to completely cancel the natural flux component of a typical DFIG in case of a severe voltage dip, which is well beyond the capability of the rotor-side converter. The reason is shown here. It can be seen from (5.14) that the natural flux dominates the stator flux at the beginning of a severe voltage dip because $V_1 \approx 0$. Thus (5.5) can be used to calculate an approximate demagnetizing current required to completely cancel the natural stator flux as follows:

$$\boldsymbol{i_r^s} = -\frac{L_m}{L_s}\frac{1}{\sigma L_r}\boldsymbol{\psi_s^s}. \tag{5.19}$$

The above equation shows that the demagnetizing current is inversely proportional to

the rotor transient inductance σL_r, which is normally very small. Although $\boldsymbol{i_r^s}$ need to be transformed to the rotor reference frame for implementation, the amplitude remains unchanged after the transformation. Considering the DFIG model used in the real-time simulation in this chapter, the demagnetizing current in per unit in the beginning of a full voltage dip to cancel the natural flux can be estimated as follows:

$$|i_{r,demag}| = \frac{L_m}{L_s}\frac{1}{\sigma L_r} = 2.86. \tag{5.20}$$

Such large demagnetizing current can not be generated by the rotor-side converter which is normally sized at 30% of the machine rating.

By combining the crowbar circuit and the demagnetizing technique, it is possible to reduce not only the rotor overcurrent at the beginning of a voltage dip but also the crowbar activation time. The sooner the crowbar is disconnected, the faster the converter can resume normal operation and contribute to the grid voltage recovery. It is possible to keep the converter connected to the rotor during grid voltage dips and support the grid even during the dip [58], [59], [61].

It is proposed in this research that the crowbar should be connected at the beginning of a voltage dip to reduce the initial rotor current spike, while the demagnetizing solution is inapplicable since it would require a current beyond the capacity of the converter. When the rotor current has decayed to a value less than the converter limit, the crowbar is disconnected and the rotor-side converter is enabled. The demagnetizing current can then be injected to further assist reducing the rotor current.

The sequence of the proposed fault ride-through control is summarized as follows.

1. Enable the crowbar immediately after a grid fault is detected.

2. At the same time, start injecting a demagnetizing current into the rotor that is calculated as follows:

$$\boldsymbol{i_{r,demag}^r} = -\frac{L_m}{L_s}\frac{1}{\sigma L_r}\boldsymbol{\psi_{sn}^s} e^{-j\omega_r t} \tag{5.21}$$

where $\boldsymbol{\psi_{sn}^s}$ is the natural flux. If the calculated demagnetizing currents exceed the converter current limit, just inject the demagnetizing currents that are equal to the

converter limit.

3. As the amplitude of the rotor current decreases, disconnect the crowbar. The converter progressively injects the reactive current component to the grid in order to generate reactive power. The rotor total current including the demagnetizing and reactive currents should not exceed the converter current limit.

4. After the grid fault is cleared, the converter can resume its normal operation generating the active and reactive power.

The scheme diagram of the described fault ride-through control is shown in Figure 5.4.

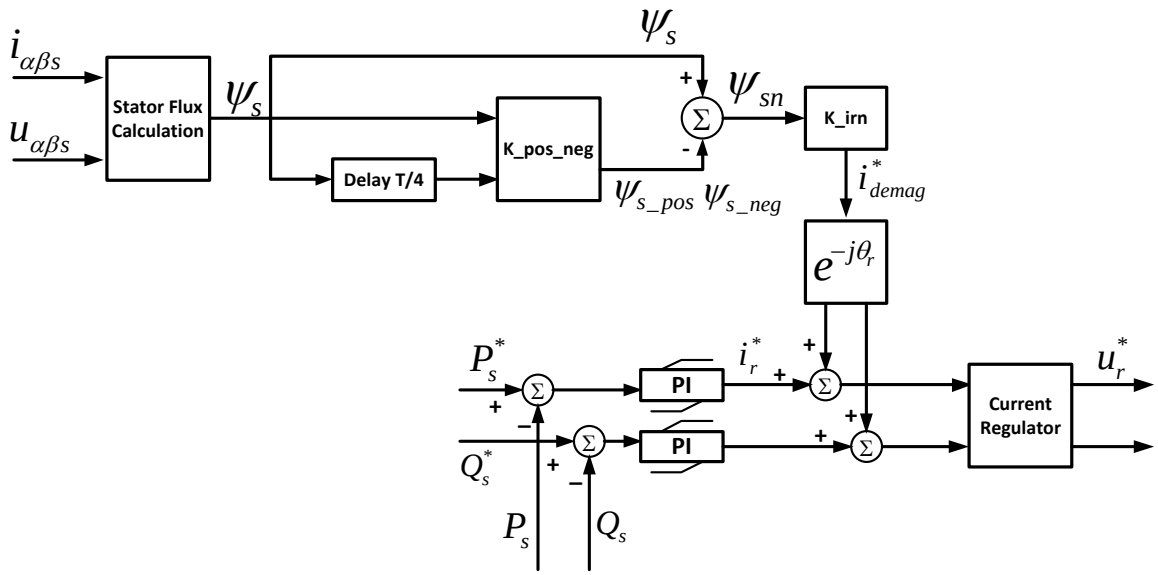

Figure 5.4 Improved Fault ride-through control strategy for DFIG-based wind turbine.

The proposed FRT control strategy requires fast and accurate separation of stator flux into forced flux and natural flux components. Since the natural flux is actual the zero sequence flux, the "one quarter delay" method described in [67] is used here. This method can be expressed as

$$\boldsymbol{\psi_{s\alpha\beta+}}(t) = 0.5[\boldsymbol{\psi_{s\alpha\beta}}(t) + j\boldsymbol{\psi_{s\alpha\beta}}(t - T/4)] \tag{5.22}$$

and

$$\boldsymbol{\psi_{s\alpha\beta-}}(t) = 0.5[\boldsymbol{\psi_{s\alpha\beta}}(t) - j\boldsymbol{\psi_{s\alpha\beta}}(t - T/4)] \tag{5.23}$$

where $\boldsymbol{\psi_{s\alpha\beta}}(t) = \boldsymbol{\psi_{s+}}e^{j\omega_s t} + \boldsymbol{\psi_{s-}}e^{-j\omega_s t}$,and T is the time period of the fundamental frequency. Therefore, the natural flux can be calculated as follows

$$\boldsymbol{\psi_{sn\alpha\beta}}(t) = \boldsymbol{\psi_{s\alpha\beta}}(t) - \boldsymbol{\psi_{s\alpha\beta+}}(t) - \boldsymbol{\psi_{s\alpha\beta-}}(t). \tag{5.24}$$

The demagnetizing current can thus be calculated and superimposed on the reference current after the converter is re-enabled as shown in Figure 5.4.

5.2.3 Real-Time Simulation Results

To verify the proposed FRT approach, the model responses under severe grid disturbances were examined using the real-time simulation platform. The behavior of a 1.5-MW DFIG-based wind turbine equipped with an active crowbar, with and without the implementation of demagnetizing current injection, was compared. The wind turbine was operating at its rated power and its maximum speed (s=-0.2) when at time t=0. Assuming the worst scenario, a 150-ms three-phase short-circuit fault was assumed to occur at the high-voltage side of the generator step-up transformer at 0.2 second. The stator-side voltages are shown in Figure 5.5. The rotor current and converter current, as well as the crowbar control signal, are plotted in the following figures.

Figure 5.6 shows the rotor and converter current without any protection. It can be seen that the rotor fault current oscillates and slowly decays from the initial peak value of over 2.6 pu at the first instant of the voltage dip. The fault current also exceeds the converter limit (1.5 pu) at the fault clearance.

Figure 5.7 shows the rotor and converter current with a crowbar circuit. It can be seen that the crowbar has triggered at the fault inception resulting in limiting the converter current. However, the rotor current still exhibits large oscillations over the converter limit and the crowbar was kept enabled for around 3 cycles. During this period, the DFIG is not controllable in terms of the power outputs.

Figure 5.8 shows the rotor and converter current with the implementation of the demagnetizing current injection. It can be seen that the demagnetizing current injection can successfully reduce the amplitude of the rotor fault current oscillation such that it never exceeds the con-

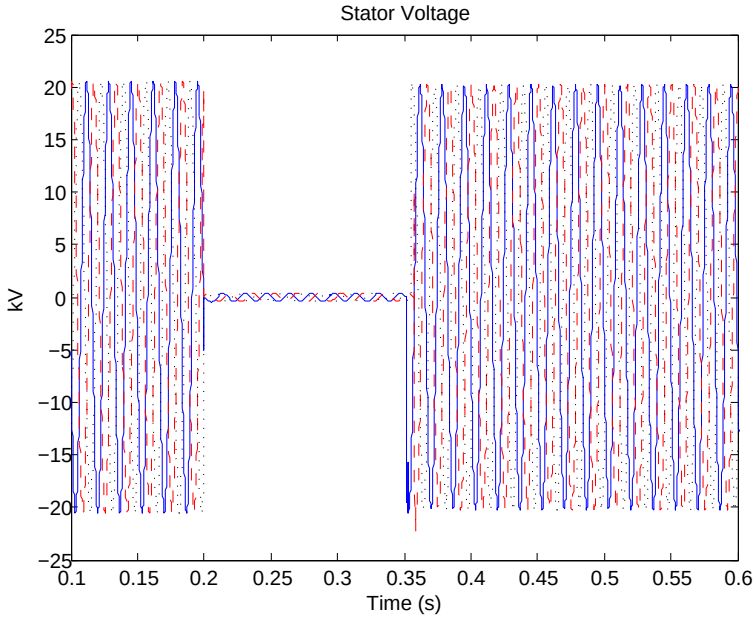

Figure 5.5 Stator-side voltages.

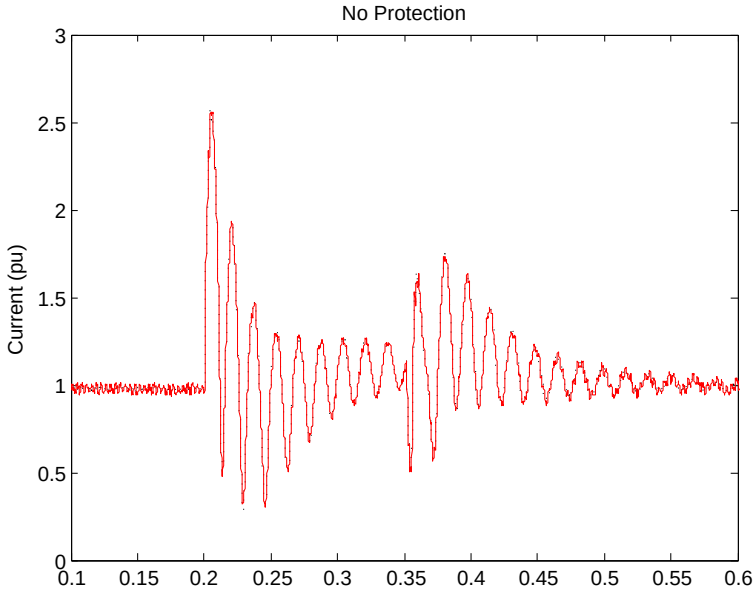

Figure 5.6 Rotor current (dotted balck) and converter current (solid red) without protection.

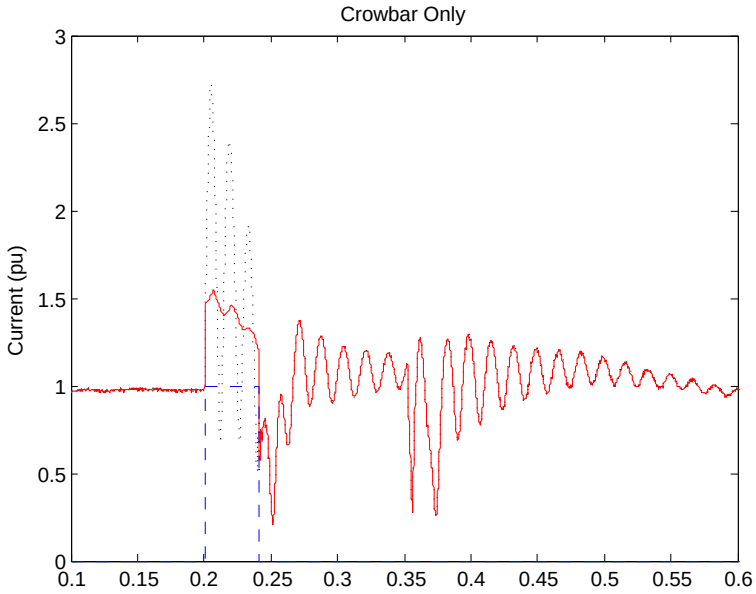

Figure 5.7 Rotor current (dotted balck), converter current (solid red) and crowbar trigger signal (dashed blue) with crowbar only.

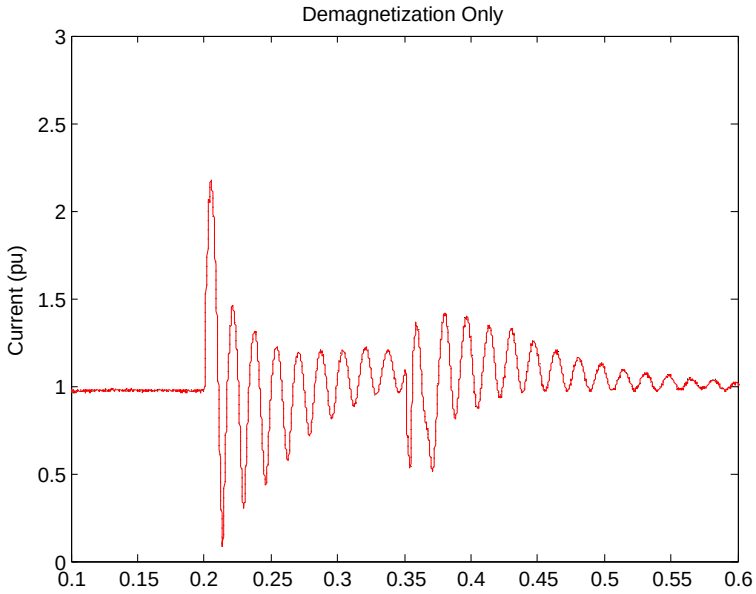

Figure 5.8 Rotor current (same as converter current) with demagnetizing current injection only.

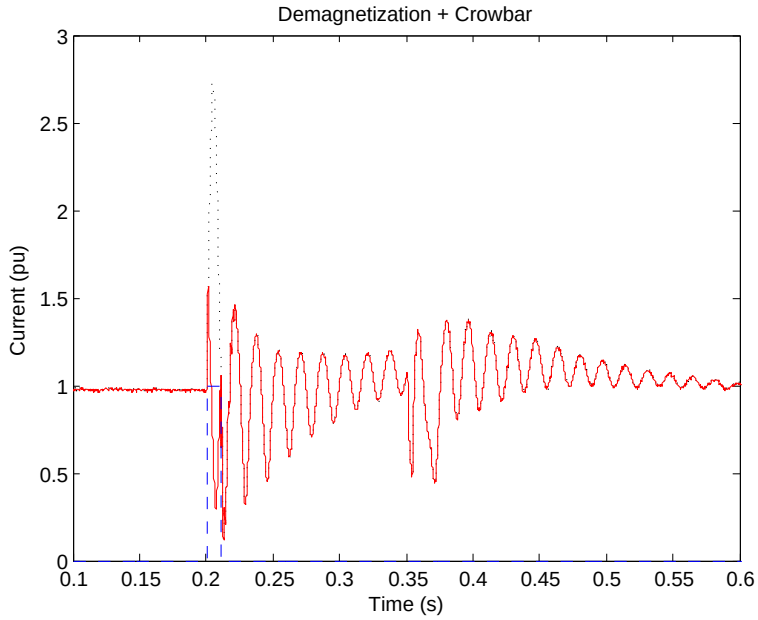

Figure 5.9 Rotor current (dotted balck), converter current (solid red) and crowbar trigger signal (dashed blue) with both crowbar and demagnetizing current injection.

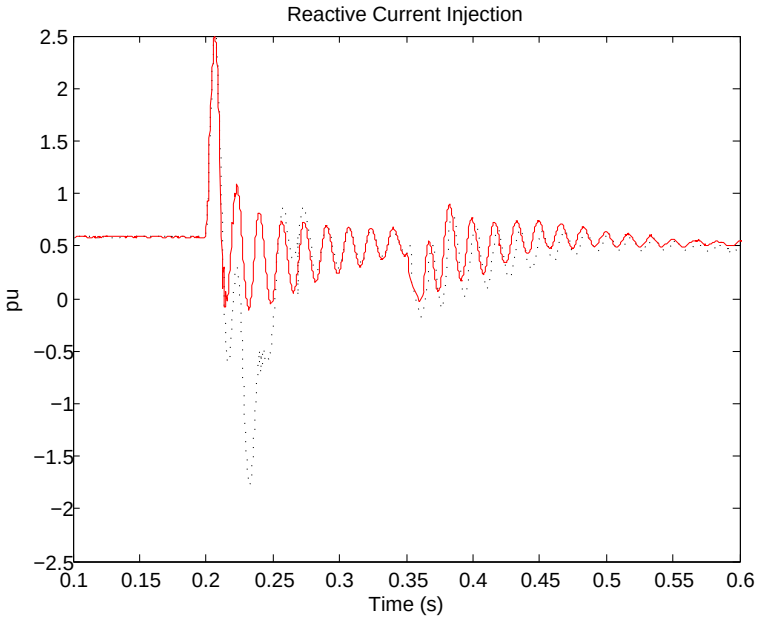

Figure 5.10 Reactive current injection into the grid for crowbar only (dotted black) and crowbar plus demagnetizing current injection (solid red).

verter except for the first instant of the voltage dip due to the inevitable control delay. The converter overcurrent at the first instant of the voltage dip can not be solved by the demagnetizing current injection based on the analysis in the previous section.

Figure 5.9 show the rotor and converter current with both the crowbar and the implementation of the demagnetizing current injection. Combining of these two FRT techniques results in limiting the initial amplitude of the fault current and enabling fast fault current decay. The crowbar connection time was reduced by approximately 2 cycles. The DFIG is able to resume its normal control after a shorter period of time compared to the situation where only the crowbar is implemented. This can be verified in Figure 5.10 where the reactive currents injected into the grid are plotted. Thanks to the proposed combined FRT technique, the reactive power support to the grid can be provided by the wind turbine sooner even during the fault.

5.3 Improved Grid Fault Ride-Through Strategy for PMSG-Based Wind Turbine

5.3.1 Improved Fault Ride-Through Control

In this section, the behavior of a PMSG-based VSWT under grid fault conditions is firstly analyzed. Then, a modified generator torque control scheme for fault ride-through is proposed.

When a grid disturbance occurs, a voltage dip will appear on the point of connection of the wind turbine to the grid. The fault behavior depends on different types of wind turbines. For DFIG-based wind turbines, a voltage dip on the grid side will probably induce overvoltages and overcurrents on generator rotor outputs because its stator is directly connected to the grid. The PMSG-based wind turbines are less affected by grid disturbances since the generator dynamics are completely decoupled from the grid by the dc-link capacitor. However, it is the decoupling that may result in overvoltages on the dc bus during grid disturbances. The analysis is presented here. The active power P_{dc} flowing through the dc bus is given by

$$P_{dc} = V_{dc} I_{dc} = C V_{dc} \frac{d}{dt} V_{dc}, \tag{5.25}$$

and its relation with the machine-side power P_m and the grid-side power P_g without losses is

$$P_{dc} = P_m - P_g. \tag{5.26}$$

In the steady state, the active power P_m generated from the wind turbine approximately equals to the active power P_g delivered to the grid and then $P_{dc} \approx 0$. The grid active power P_g can also be expressed as

$$P_g = V_{dg} I_{dg} = v_{ag} i_{ag} + v_{bg} i_{bg} + v_{cg} i_{cg} \tag{5.27}$$

where $V_{dg} = |V_g|$ and I_{dg} are d- axis grid voltage and current components in the grid-voltage reference frame. It can be seen from (5.27) the power that can be delivered to grid is proportional to the grid voltage. During a severe grid disturbance where the grid voltage drops to nearly zero, no power can be delivered to grid. In the same time, the wind turbine still produces a large amount of power because it does not "know" a grid fault has happened. In this situation, the dc-link capacitor will be charged by the extra power and its voltage will increase in an uncontrollable way without protection.

A breaking resistor with a power electronic switch can be inserted into the dc circuit in parallel with the capacitor to dissipate the energy from the wind turbine [64]. The resistor size and material should be chosen and the switch duty cycle control scheme need carefully design to avoid overheating. Pitch angle control can also be utilized to limited wind power captured during grid disturbances. However, even with the maximum changing rate of 20° per second it is not fast enough to reduce the overvoltages [64].

Instead of dissipating wind energy to the breaking resistor, it is also possible to reserve the energy in the wind turbine in the kinetic form during grid disturbances and release it after the fault is cleared. A straightforward FRT approach for PMSG-based VSWTs is presented here. As indicated from (5.25) and (5.26), there would be no capacitor charging and overvoltages if the active powers injected into and delivered out of the dc bus were kept balanced during grid disturbances, i.e., $P_g = P_m$. Assuming no copper losses and iron losses, the active power from PMSG in steady-state can be expressed as

$$P_m = T_e \omega_r. \tag{5.28}$$

Considering (5.26),(5.27), and (5.28), it is proposed that during grid disturbances the reference electromagnet torque in the MSC controller is switched to

$$T_e^* = (v_{ag}i_{ag} + v_{bg}i_{bg} + v_{cg}i_{cg})/\omega_r. \tag{5.29}$$

Therefore, the active power generated by the PMSG is regulated to follow the grid-side power profile, resulting in minimum dc-link voltage disturbances. Unlike the pitch angle controller which is realized by servo motors, the bandwidth of the PWM-based generator current controller is normally high enough such that the proposed FRT scheme can response to sudden grid voltage drops. The turbine speed may increase by a few percents for temporary conservation of wind energy as the kinetic energy. Since most grid disturbances last less than several hundreds of milliseconds, such speed increase is expected to have negligible impact on large wind turbines with high inertia.

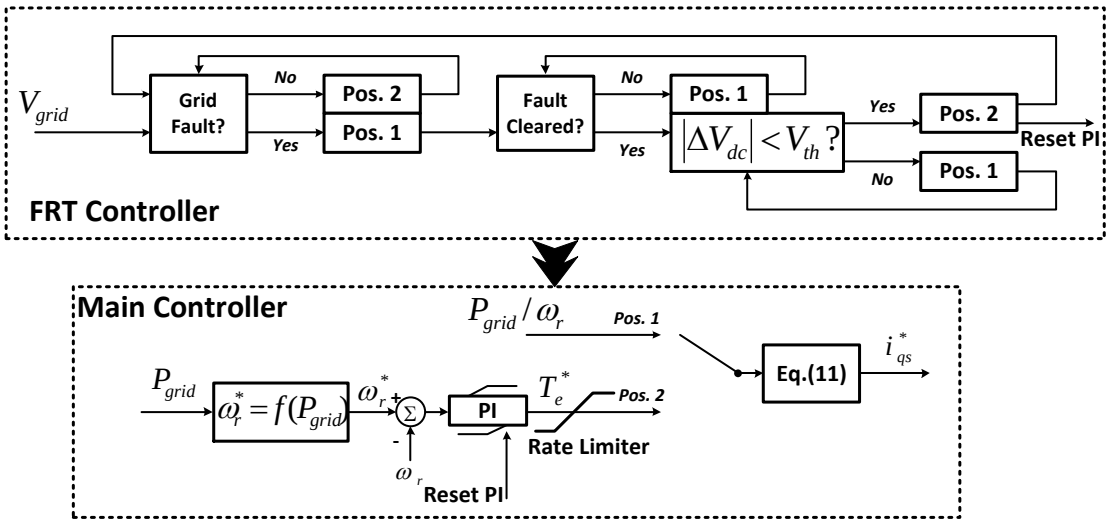

Figure 5.11 Improved Fault ride-through control strategy for PMSG-based wind turbine.

The overall control scheme is shown in Fig. 5.11. Once a grid fault is detected, the turbine power output is immediately controlled to track the actual power injected into the grid, thus preserving the power balance on the dc-link capacitor. To avoid large transients during the voltage recovery stage, the input of the reference electromagnet torque does not change from

position 1 to position 2 immediately after the fault is cleared. Instead, the dc-link voltage is continuously monitored until its disturbance is less than some threshold, i.e. 0.05 pu. The rotor speed PI controller output is then reset to the current reference electromagnet torque value. In addition, the rate limiter on the reference electromagnet torque ensures a smooth change from its current value to the optimal steady-state value. In this way, the dc-link voltage disturbance can be minimized both during grid faults and in the post-fault condition. Of course, the breaking resistor can still be used as a backup protection scheme to enhance the FRT capability in case of long-term faults.

5.3.2 Real-Time Simulation Results

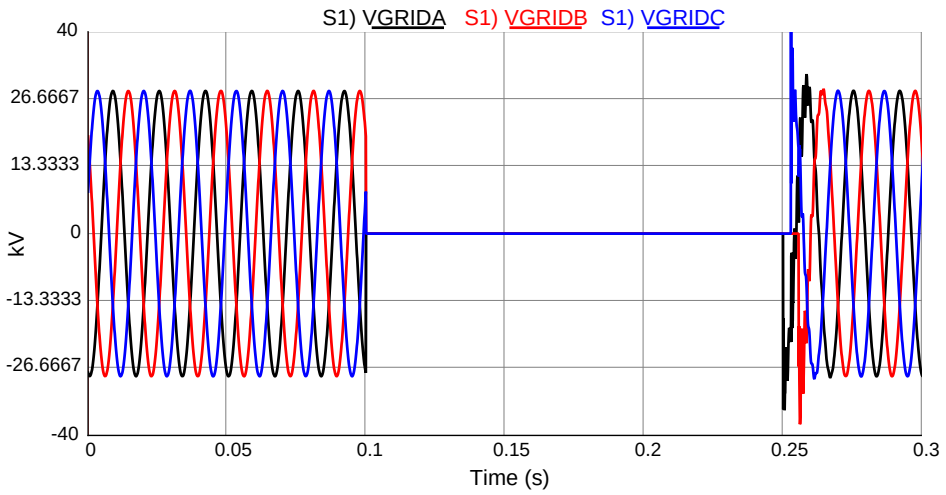

Figure 5.12 Three-phase grid fault.

To verify the proposed FRT approach, the model responses under severe grid disturbances were examined. Assuming the worst scenario, a 150-ms three-phase short-circuit fault was assumed to occur at the high-voltage side of the generator step-up transformer at 0.1 sec, as shown in Fig.5.12. The waveforms of the generator speed, power, and the dc-link voltage are plotted in Fig. 5.13 and Fig. 5.14. The wind turbine was assumed to be operating at the full load under the nominal wind speed before the fault occurred.

As can be seen from Fig. 5.13, the grid was unable to absorb the power delivered by the wind turbine during the grid fault. Without the FRT control, the wind turbine continued to generate

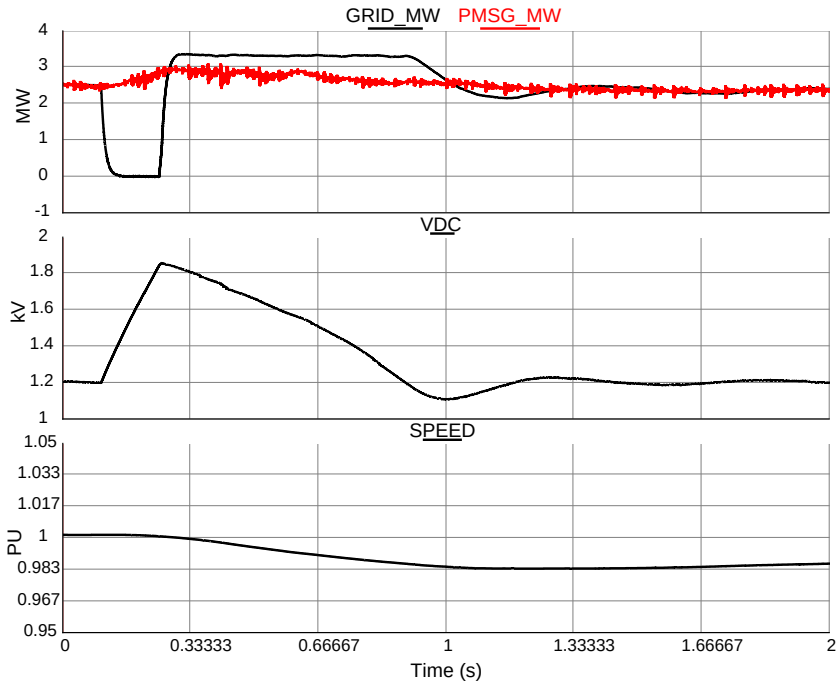

Figure 5.13 Turbine response without FRT control.

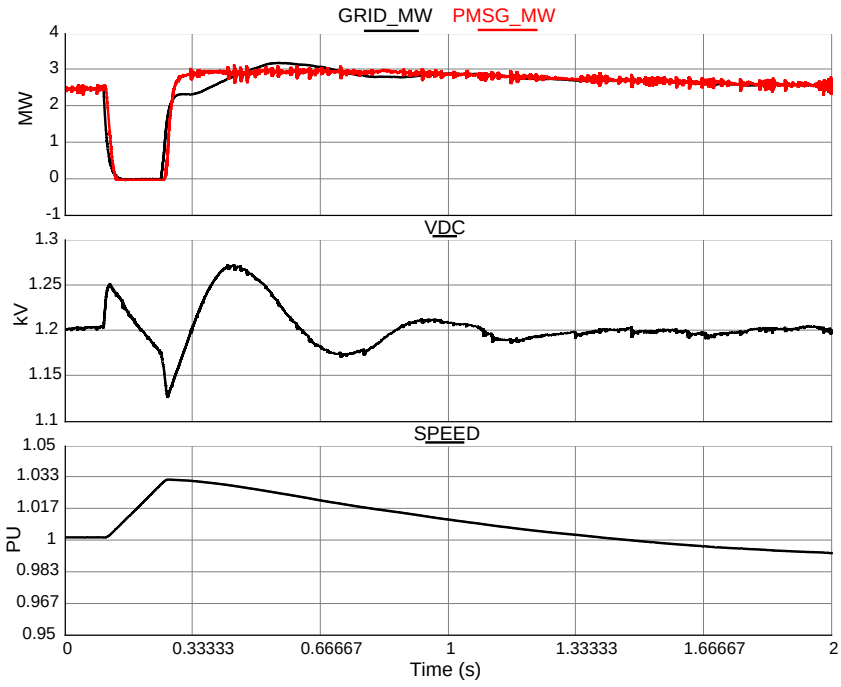

Figure 5.14 Turbine response with FRT control.

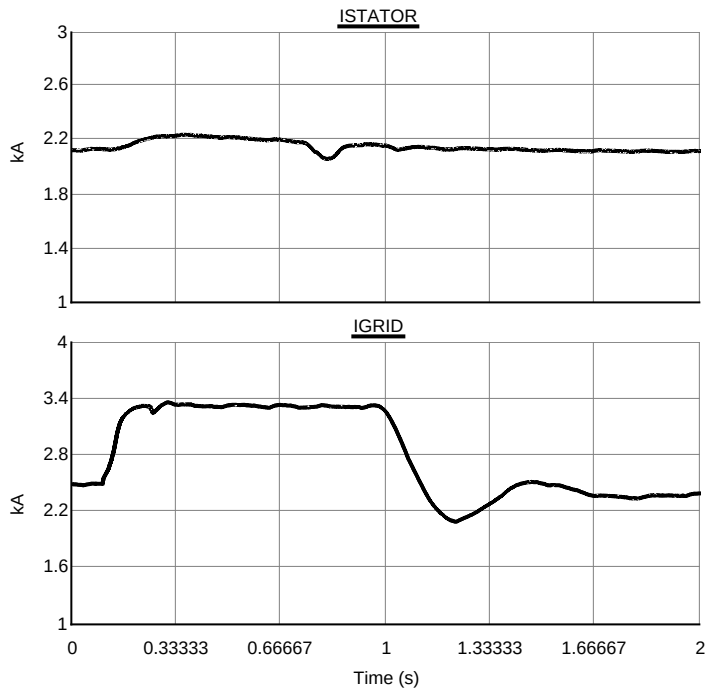

Figure 5.15 Converter current (MSC current (upper) and GSC current (lower)) without FRT control.

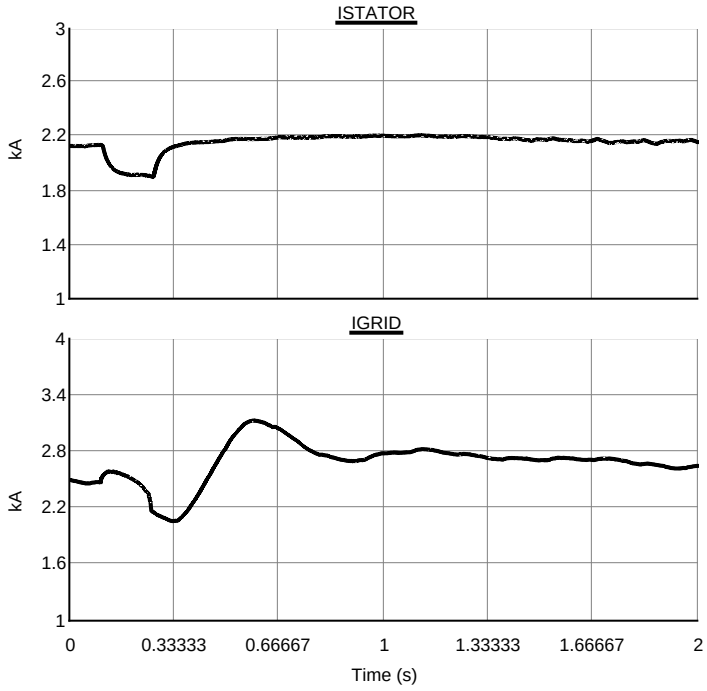

Figure 5.16 Converter current (MSC current (upper) and GSC current (lower)) with FRT control.

power as in the pre-fault condition. Therefore, the extra power started to charge the dc-bus capacitor resulting in overvoltages of more than 1.5 pu. Fig. 5.14 shows the effectiveness of the FRT control. At the fault occurrence, the reference generator torque immediately changed such that the generator power kept track on the grid power profile. A dc-link voltage peak occurred right after the fault occurrence due to the inevitable controller delay. The turbine speed slightly increased to 1.033 pu. After the fault clearance, The generator torque was controlled such that the turbine power smoothly returned to the nominal value. The peak dc-link voltage was successfully limited within 1.05 pu during the entire fault period without adding any extra hardware components. Fig. 5.15 and Fig. 5.16 show the converter current without and with the proposed FRT control, respectively. It can be seen that the converter current is kept within 120% of the rated value if the FRT control is implemented. In this range, the full-scale converter is able to ride-through the grid fault without other protection measures.

CHAPTER 6. CONCLUSIONS

6.1 Conclusions

The objective of this thesis is to investigate the modeling, control, and protection of variable-speed wind turbines, typically consisting a DFIG or a PMSG as the generation system. Special attention has been paid on the sensorless control and grid fault ride-through strategies, as well as the real-time implementation and verification of the wind turbine model and controller.

Complete electromagnetic transient models for MW-size grid-connected variable-speed wind turbines based on either a DFIG or a PMSG are developed for real-time simulation. The model includes the aerodynamic, mechanical and electrical components, and the mechanical and electrical controllers of the wind turbine.

The sensorless generator control is desirable for variable-speed wind turbines. Specially, a speed-adaptive reduced-order observer implemented in the synchronous reference frame for sensorless vector control of DFIGs is proposed and analyzed. The rotor current dynamics are simulated as an adaptive model and a speed-adaptation loop is included in the observer. The design guidelines for feedback and adaptation gains are provided based on the derived closed-loop observer model. Effects of parameter variations on the steady-state and dynamic performance have been investigated, and no serious influences are observed. Simulation results have demonstrated the desired performance of this sensorless control approach for a wide operating range.

It is of great importance for today's variable-speed wind turbines to remain connected on-line during severe grid voltage dips and contribute to voltage recovery in the post-fault condition. Improved fault ride-through strategies are proposed for DFIG- and PMSG-based

wind turbines to reduce overvoltages and overcurrents in electrical components and provide immediate grid recovery support with minimum hardware components.

All wind turbine models and control strategies previously mentioned are implemented in real-time on a new integrated simulation platform based on RTDS and dSPACE. A unique feature of this "Hardware-in-the-loop" type of platform is that a real physical interface between the system and its controller can be preserved and invistigated in simulation. Simulation results demonstrate the effectiveness of the integrated real-time simulation environment in representing the dynamic behavior of complex high-order wind turbine models and controllers. At the same time, the simulation time is significantly reduced. It is expected to have broad application prospects in wind turbine controller design and grid interconnection studies.

6.2 Contributions

The major contributions of this thesis are summarized as follows.

1. A novel integrated real-time simulation platform based on industry standard simulation tools, RTDS and dSPACE, is developed. RTDS features the real-time digital simulation of power system electromagnetic transients, while dSPACE is capable of rapid prototyping of comprehensive and complex controller designs. Unlike the previous work, the proposed simulation platform can emulate the actual interface between the physical equipment and its controller, for example, the interface where the firing pulses and measurements are transmitted back and forth between the power electronic converter and the firing pulse controller in the wind generation system. Another obvious advantage is the significant improved simulation speed. This simulation platform has served as the tool for the verification of the wind turbine models and control strategies throughout this thesis.

2. Complete electromagnetic transient models for MW-size grid-connected variable-speed wind turbines based on either a doubly-fed induction generator or a permanent-magnet synchronous generator are developed for real-time simulation. The model includes the aerodynamic, mechanical and electrical components, and the mechanical and electrical

controllers of the wind turbine. The developed models have been implemented and verified on the real-time simulation platform.

3. A new sensorless controller for the DFIG-based wind turbine generation system is proposed and analyzed. The sensorless controller utilizes a reduced-order state observer to extract the machine rotor speed and position information from voltage and current measurements, eliminating the traditional mechanical speed sensor. The observer gain design is presented. Compared to other sensorless approaches, this controller is more robust against machine parameter variations.

4. For DFIG-based wind turbines, an improved fault ride-through method combining the traditional crowbar protection circuit and the demagnetizing current injection is analyzed and verified. A theoretical analysis of the behavior of the DFIG during a three-phase voltage dip shows the rotor overcurrents are caused by the voltage induced by the natural flux which is a transient flux that appears during a voltage dip. A recently proposed demagnetizing current injection method aims to cancel this natural flux but it normally fails at the fault inception due to the converter current limit. The improved combination approach reduces the crowbar activation time and helps the wind turbine resume its normal operation and support the grid recovery as soon as the fault is less severe, even before the fault clearance.

5. For PMSG-based wind turbines, an improved fault ride-through method is proposed without using any extra protection hardware. This technique can be directly embedded into the original wind turbine electrical controller. The idea is to maintain the instantaneous energy balance at the dc bus by reserving the energy in the turbine rotor in the kinetic form during grid disturbances. It ensures the dc-link voltage is kept within the acceptable range during a voltage dip and the post-disturbance recovery period.

6.3 Future Work

From the results of this thesis, a number of recommendations for further research can be obtained.

1. The model developed in Chapter Four represents a PMSG-based wind turbine with a multiple-stage gearbox. It may also be of interest to investigate the modeling of a direct-driven or gearless PMSG-based wind turbine system. As compared to a gearbox-coupled wind turbine generator, a direct-driven generator has lower installation and maintenance cost. It can be installed in offshore wind farms or other locations with high levels of dust and sand where the gearbox is prone to fail. A multi-pole PMSG is usually selected for the direct-drive wind turbine. However, the larger number of poles results in "softer" driven shaft train, meaning the system can easily get excited by mechanical of electrical load changes. The oscillation leads to the fluctuation in the output power and the increase of mechanical fatigue of the drive train. Therefore, special damping controller should be designed to suppress the oscillations and avoid instability.

2. The DFIG behavior under a three-phase voltage dip is analyzed in Chapter Five. Asymmetrical voltage dips, such as the single-phase-to-ground fault, phase-to-phase fault, and two-phase-to-ground fault, may also be investigated in terms of the DFIG behavior and fault ride-through strategies. Unlike symmetrical faults, asymmetrical faults induce not only transitory current components but also permanent (negative sequence) components which remain throughout the whole dip. The effectiveness of the demagnetizing current injection technique is limited because the current needed to cancel the negative sequence components is usually beyond the converter limit and the fault current components do not decay during the fault. One possible solution is to use a series grid-side converter to compensate the unbalanced stator flux during asymmetrical faults. However, this will increase the total system cost and control system complexity. Therefore, other converter protection strategies for asymmetrical faults still need to be developed.

3. The real-time simulation platform used throughout the thesis is specially designed for the

study of the behavior of an individual wind turbine connected to the grid. However, the RTDS itself can also be used for real-time simulation of aggregated wind farms connected to a small-scale system whose size depends on the number of the available simulator racks. Thus, it might be of interest to investigate the interaction of two wind farms nearby, for example, whether a DFIG or PMSG-based wind farm equipped with FRT strategies can help a nearby fixed-speed induction generator-based wind farm to ride through a grid fault, without implementation of any additional ride-through strategy in the fixed-speed induction generator-based wind farm.

APPENDIX A. A WEB-BASED REMOTE CONTROL LABORATORY

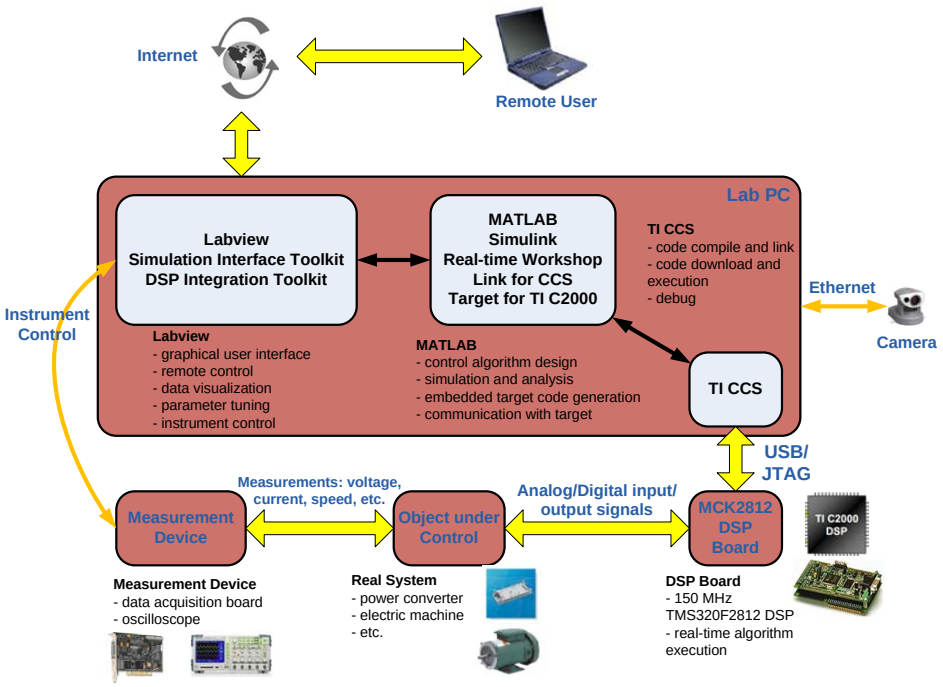

Figure A.1 A web-based remote control laboratory.

Prior to the development of the proposed real-time simulation platform at ISU, a digital-signal-processor-based remote laboratory was developed, as shown in Figure A.1. A space vector pulse-width modulator (SVPWM) is designed and implemented using the model-based design (MBD) approach. The entire process is published on web through a graphical user interface developed using Labview. The proposed sensorless vector controller will be designed, implemented, and tested following the similar procedure.

Figure A.1 shows the configuration of this remote laboratory. This remote laboratory is composed of a MCK2812 DSP board, a 3-phase IGBT power module, a laboratory PC, a

network camera, a controllable 3-phase power supply, and measurement equipment. The DSP board is connected to the laboratory PC, which is, in turn, connected to the Internet. The control system implementing a control algorithm that is developed using Simulink, is converted to executable codes for the DSP. Then the control system can drive the real process through the analog and digital I/O signals. At the same time, the virtual instrument for experiments run on the laboratory PC to enable remote control. Virtual instruments are published on the Web using the Labview built-in Web Publishing Tool. Once the VI is published, anyone can access and control an experiment using a standard web browser with proper permission. A network camera with pan, tilt and zoom control enables advanced remote monitoring over Ethernet by delivering high quality video and audio streams.

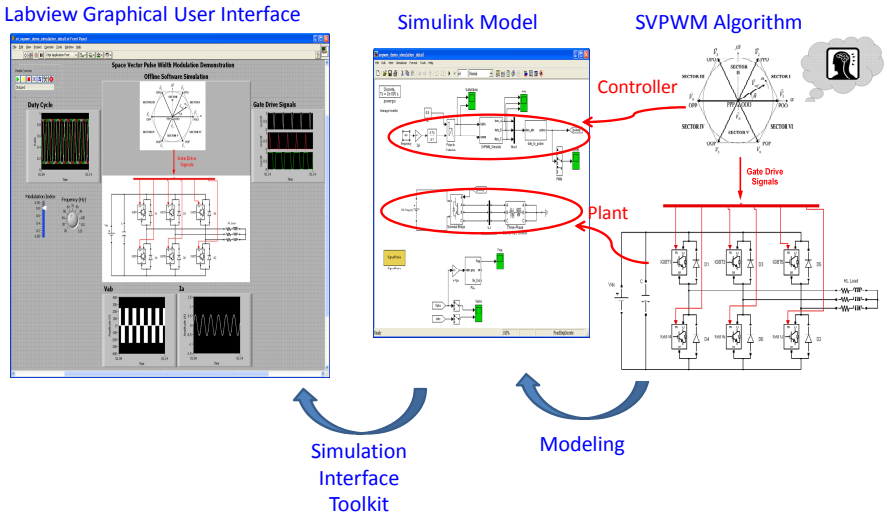

Figure A.2 SVPWM simulation in the remote laboratory: step 1, offline software simulation.

Figure A.2 shows the first step in the MBD flow. In this step, the SVPWM algorithm, power supply, IGBT power bridge, and RL load are modeled and simulated in Simulink. The Labview GUI allows remote users to modify the modulation index and frequency and observer the response.

Figure A.3 shows the second step in the MBD flow. In this step, the controller model in Simulink is compiled. The target codes are automatically generated using code generation

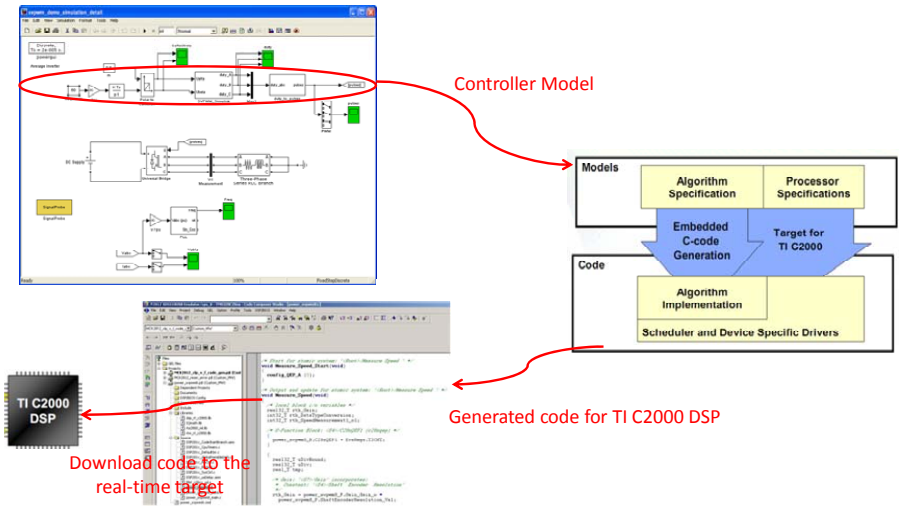

Figure A.3 SVPWM simulation in the remote laboratory: step 2, rapid prototyping of the controller.

tools for DSPs. It is worth noting that the controller model should be optimized for the target processor in order to generate efficient codes.

Figure A.4 shows the third step in the MBD flow. Once the target codes are generated and downloaded to the DSP, a processor-in-the-loop (PIL) simulation is conducted. The purpose is to test the control algorithm in the real embedded controller. In this case, the DSP communicates with the plant model through a PIL interface in a handshaking mode. Another Labview GUI also allows remote users to modify the modulation index and frequency and observer the response.

Figure A.5 shows the final step in the MBD flow. In this step, a hardware experiment is set up in the laboratory to verify the controller design. a Kikusui PCR6000W2 three-phase controllable power supply is used as the power input for the power converter and RL load. The power supply is equipped with a General Purpose Interface Bus (GPIB) interface module. The amplitude and frequency of output voltage is fully controllable by the laboratory PC via GPIB with the help of instrument drives. A Tektronix oscilloscope is also connected to the Labview GUI for the observation of actual current waveforms.

The proposed real-time simulation platform can fit into this MBD design flow between step 3 and step 4 as a middle step. The voltage-source inverter and the load can be simulated

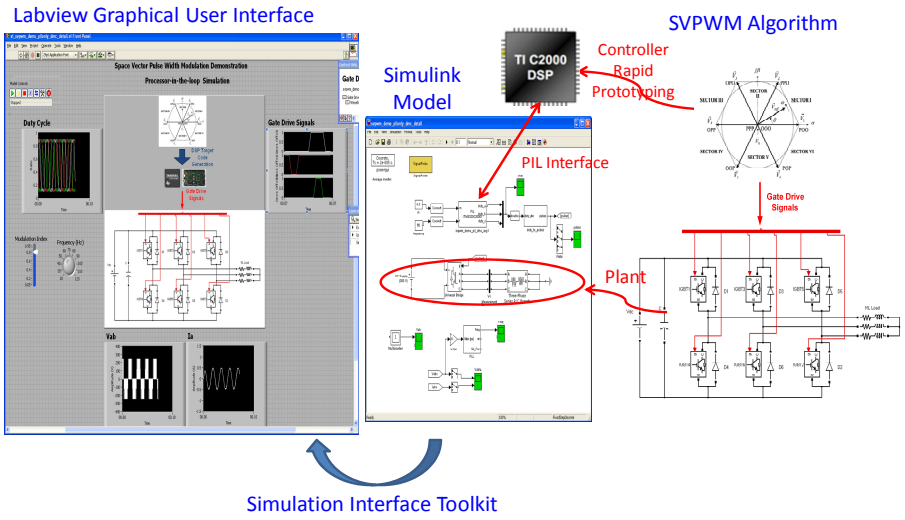

Figure A.4 SVPWM simulation in the remote laboratory: step 3, processor-in-the-loop simulation.

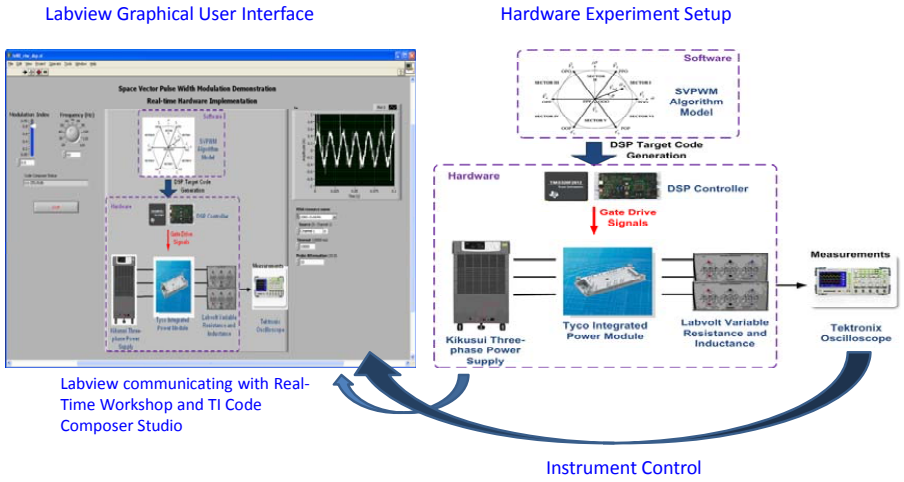

Figure A.5 SVPWM simulation in the remote laboratory: step 4, hardware verification.

in RTDS ans the SVPWM controller is implemented in dSPACE, using a similar approach described in Chapter 2.

APPENDIX B. WIND TURBINE POWER COEFFICIENT $C_p(\lambda, \theta)$

The power coefficient $C_p(\lambda, \theta)$ of the wind turbine in this thesis is determined by the following equation [45]:

$$C_p(\lambda, \theta) = c_1 \left\{ c_6 \lambda + [m c_2 - (2.5 + \theta) c_3 - c4] \, e^{-m c_5} \right\} \tag{B.1}$$

where

$$m = \frac{1}{\lambda + (2.5 + \theta) c_7} - \frac{c_8}{1 + (2.5 + \theta)^3}$$

and

$$c_1 = 0.645, c_2 = 116, c_3 = 0.4, c_4 = 5,$$

$$c_5 = 21, c_6 = 0.00912, c_7 = 0.08, c_8 = 0.035.$$

The characteristic of $C_p(\lambda, \theta)$ is shown in Figure 4.2. It can be seen that $C_{p,max} = 0.5$ when $\theta = 0$ and $\lambda = \lambda_{max} = 9.95$.

BIBLIOGRAPHY

[1] 20% Wind Energy by 2030: Increasing Wind Energy's Contribution to U.S. Electricity Supply. [Online]. Available: http://www.nrel.gov/docs/fy08osti/41869.pdf

[2] T. Ackermann, *Wind Power in Power Systems*, Hoboken, NJ: Wiley, 2005.

[3] S. Muller, M. Deicke and Rik W. De Doncker, "Doubly fed induction generator systems for wind turbines," *IEEE Industry Applications Magazine*, vol. 8, no. 3, pp. 26-33, May-Jun. 2002.

[4] H. Li and Z. Chen, "Overview of different wind generator systems and their comparisons," *IET Renewable Power Generation*, vol. 2, no. 3, pp. 123-138, 2008.

[5] K. Rajashekara, A. Kawamura, and K. Matsuse, Eds., *Sensorless Control of AC Motors*, Piscataway, NJ: IEEE Press, 1996.

[6] J. Holtz, "Sensorless control of induction motor drives," *Proc. IEEE*, vol. 90, no. 8, pp. 1359-1394, Aug. 2002.

[7] J. Holtz, "Sensorless control of induction machines–With or without signal injection?" *IEEE Trans. Ind. Electron.*, vol. 53, no. 1, pp. 7-30, Feb. 2006.

[8] L. Xu and W. Cheng, "Torque and reactive power control of a doubly-fed induction machine by position sensorless scheme," *IEEE Trans. Ind. Appl.*, vol. 31, no. 3, pp. 636-641, May 1995.

[9] L. Morel, H. Godfroid, A. Mirzaian, and J. M. Kauffmann, "Doubly-fed induction machine: converter optimization and field oriented control without position sensor," *Proc. Inst. Elect. Eng., Electr. Power Appl.*, vol. 145, no. 4, pp. 360-368, Jul. 1998.

[10] B. Hopfensperger, D. J. Atkinson, and R. A. Lakin, "Stator-flux oriented control of a doubly-fed induction machine with and without position encoder," *Proc. Inst. Elect. Eng., Electr. Power Appl.*, vol. 147, no. 4, pp. 241-250, Jul. 2000.

[11] R. Datta and V. T. Ranganathan, "A simple position sensorless algorithm for rotor side field oriented control of would rotor induction machine," *IEEE Trans. Ind. Electron.*, vol. 48, no. 4, pp. 786-793, Aug. 2001.

[12] M. Abolhassani, P. Enjeti, and H. Toliyat, "Integrated doubly fed electric alternator/active filter (IDEA), a viable power quality solution, for wind energy conversion systems," *IEEE Trans. Energy Conversion*, vol. 23, no. 2, pp. 642-650, Jun. 2008.

[13] R. Cardenas, R. Pena, J. Proboste, G. Asher, and J. Clare, "MRAS observer for sensorless control of stand-alone doubly-fed induction generators," *IEEE Trans. Energy Conversion*, vol. 20, no. 4, pp. 710-718, Dec. 2005.

[14] R. Pena, R. Cardenas, J. Proboste, G. Asher, and J. Clare, "Sensorless control of doubly-fed induction generators using a rotor-current-based MRAS observer," *IEEE Trans. Ind. Electron.*, vol. 55, no. 1, pp. 330-339, Jan. 2008.

[15] R. Cardenas, R. Pena, J. Clare, G. Asher, and J. Proboste, "MRAS observers for sensorless control of doubly-fed induction generators," *IEEE Trans. Power Electron.*, vol. 23, no. 3, pp. 1075-1084, May. 2008.

[16] C. Schauder, "Adaptive speed identification for vector control of induction motors without transducers," *IEEE Trans. Ind. Appl.*, vol. 28, no. 5, pp. 1054-1061, Sept./Oct. 1992.

[17] M. Hinkkanen and J. Luomi, "Digital implementation of full-order flux observers for induction motors," In *Proc. EPE-PEMC'02*, Cavtat and Dubrovn, Croatia, CD-ROM.

[18] A. D. Hansen, F. Iov, P. Sørensen, N. Cutululis, C. Jauch, F. Blaabjerg, "Dynamic wind turbine models in power system simulation tool DIgSILENT," RisøNational Laboratory Report R-1400(ed.2), Denmark, August 2007.

[19] D. Maclay, "Simulation gets into the loop," *IEE Review*, vol. 43, no. 3, pp. 109-112, May 1997.

[20] P. Terwiesch, T. Keller, and E. Scheiben, "Rail vehicle control system integration testing using digital hardware-in-the-loop simulation," *IEEE Trans. Control Syst. Technol.*, vol. 7, no. 3, pp. 352-362, May 1999.

[21] D. Zhang, H. Li, "A stochastic-based FPGA controller for an induction motor drive with integrated neural network algorithms," *IEEE Trans. Ind. Electron.*, vol. 55, no. 2, pp. 551-561, Feb. 2008.

[22] S. Abourida, C. Dufour, J. Belanger, G. Murere, N. Lechevin, and B. Yu, "Real-time PC-based simulator of electric systems and drives," In *Proc. IEEE Appl. Power Electron. Conf.*, 2002, pp. 433-438.

[23] A. Monti, E. Santi, R. Dougal, and M. Riva, "Rapid prototyping of digital controls for power electronics," *IEEE Trans. Power Electron.*, vol. 18, no. 3, pp. 915-923, May 2003.

[24] R. Champagne, L.-A. Dessaint, H. Fortin-Blanchette, and G. Sybille, "Analysis and validation of a real-time AC drive simulator," *IEEE Trans Power Electron.*, vol. 19, no. 2, pp. 336-345, Mar. 2004.

[25] Y. Li, D. M. Vilathgamuwa, and P. C. Loh, "Design, analysis, an real-time testing of a controller for multibus microgrid system," *IEEE Trans. Power Electron.*, vol. 19, no. 5, pp. 1195-1204, Sep. 2004.

[26] H. Li, M. Steurer, S. Woodruff, K. L. Shi, D. Zhang, "Development of a unified design, test, and research platform for wind energy systems based on hardware-in-the-loop real time simulation," *IEEE Trans. Ind. Electron.*, vol. 53, no. 4, pp. 1144-1151, Jun. 2006.

[27] K. Maki, A. Kulmala, S. Repo, P. Jarventausta, "Studies on grid impacts of distributed generation in a combined real-time simulation environment," in 7th International Conference on Power System Transients, IPST 2007, 4-7 June, Lyon, France, 6 p.

[28] A. Makinen and H. Tuusa, "Wind turbine and grid interaction studies using integrated real-time simulation environment," in Nordic Workshop on Power and Industrial Electronics, NORPIE/2008, Finland.

[29] T. Maguire and J. Giesbrecht, "Small Time-Step ($< 2\mu sec$) VSC Model for the Real Time Digital Simulator," In *Proc. IPST 2005*, Montreal Canada, June 2005.

[30] R. Pena, J. C. Clare, and G. M. Asher, "Double fed induction generator using back-to-back PWM converter and its application to variable-speed wind-energy generation," *Proc. IEE B Electr. Power Appl.*, vol. 143, no. 3, pp. 231-241, May 1996.

[31] A. Tapia, G. Tapia, J. X. Ostolaza, and J. R. Saenz, "Modeling and control of a wind turbine driven doubly fed induction generator," *IEEE Trans. Energy Convers.*, vol. 18, no. 2, pp. 194-204, Jun. 2003.

[32] G. Tapia, A. Tapia, and J. X. Ostolaza, "Two alternative modeling approaches for the evaluation of wind farm active and reactive power performances," *IEEE Trans. Energy Convers.*, vol. 21, no. 4, pp. 909-920, Dec. 2006.

[33] H. Kubota, K. Matsuse, and T. Nakano, "DSP-based speed adaptive flux observer of induction motor," *IEEE Trans. Ind. Electron.*, vol. 29, no. 2, pp. 344-348, Mar./Apr. 1993.

[34] G. Yang and T. -H. Chin, "Adaptive-speed identification scheme for a vector-controlled speed sensorless inverter-induction motor drive," *IEEE Trans. Ind. Appl.*, vol. 29, no. 4, pp. 820-825, Jul./Aug. 1993.

[35] W. Leonhard, *Control of Electrical Drives*, Springer-Verlag, Berlin, 2001.

[36] D. W. Novotny and T. A. Lipo, *Vector Control and Dynamics of AC Drives*, Oxford, 1998.

[37] B. K. Bose, *Modern Power Electronics and AC Drives*, Prentice-Hall, Upper Saddle River, NJ, 2002.

[38] S. Yang and V. Ajjarapu, "A speed-adaptive reduced-order observer for sensorless vector control of doubly fed induction generator-based variable-speed wind turbines," *IEEE Trans. Energy Convers.*, vol. 25, no. 3, pp. 891-900, Sep. 2010.

[39] L. Harnefors and M. Hinkkanen, "Complete stability of reduced-order and full-order observers for sensorless IM drives," *IEEE Trans. Ind. Electron.*, vol. 55, no. 3, pp. 1319-1329, Mar. 2008.

[40] H. A. Toliyat, E. Levi, and M .Raina, "A review of RFO induction motor parameter estimation techniques," *IEEE Trans. Energy Convers.*, vol. 18, no. 2, pp. 271-283, Jun. 2005.

[41] M. Rashed, F. Stronach, and P. Vas, "A new stable MRAS-based speed and stator resistance estimators for sensorless vector control induction motor drive at low speeds," in *Conf. Rec. IEEE-IAS Annu. Meeting*, vol. 2, pp. 1181-1188, Salt Lake City, UT, 2003.

[42] E. Levi and M. Wang, "Online identification of the mutual inductance for vector controlled induction motor drives," *IEEE Trans. Energy Convers.*, vol. 18, no. 2, pp. 299-305, Jun. 2003.

[43] R. Fadaeinedjad, M. Moallem, and G. Moschopoulos, "Simulation of a wind turbine with doubly fed induction generator by FAST and simulink," *IEEE Trans. Energy Convers.*, vol. 23, no. 2, pp. 690-700, Jun. 2008.

[44] M. Hinkkanen and J. Luomi, "Stabilization of regenerating-mode operation in sensorless induction motor drives by full-order flux observer design," *IEEE Trans. Ind. Electron.*, vol. 51, no. 6, pp. 1318-1328, Dec. 2004.

[45] *MATLAB SIMULINK SimPowerSystems User's Manual*, MathWorks Inc., 2010.

[46] V. Akhmatova, A. H. Nielsenb, J. K. Pedersenc and O. Nymann, "Variable-speed wind turbines with multi-pole synchronous permanent magnet generators. Part I: Modelling in dynamic simulation tools," *Wind Engineering*, vol. 27, no. 6, pp. 531-548, 2004.

[47] K. Tan and S. Islam, "Optimum Control Strategies in Energy Conversion of PMSG Wind Turbine System Without Mechanical Sensors," *IEEE Trans. Energy Convers.*, vol. 19, no. 2, pp. 392-399, 2004.

[48] S. Morimoto, H. Nakayama, M. Sanada and Y. Takeda, "Sensorless Output Maximization Control for Variable-Speed Wind Generation System Using IPMSG," *IEEE Trans. Ind. Appl.*, vol. 41, no. 1, pp. 60-67, 2005.

[49] M. Chinchilla, S. Arnaltes and J. C. Burgos, "Control of Permanent-Magnet Generators Applied to Variable-Speed Wind-Energy Systems Connected to the Grid," *IEEE Trans. Energy Convers.*, vol. 21, no. 1, pp. 130-135, 2006.

[50] A. Hansen and G. Michalke, "Modelling and Control of Variable-speed Multi-pole Permanent Magnet Synchronous Generator Wind Turbine," *Wind Energy*, vol. 11, pp. 537-554, May 2008.

[51] W. Qiao, L. Qu, and R. G. Harley, "Control of IPM Synchronous Generator for Maximum Wind Power Generation Considering Magnetic Saturation," *IEEE Trans. Ind. Appl.*, vol. 45, no. 3, pp. 1095-1105, 2009.

[52] Md. E. Haque, M. Negnevitsky and K. M. Muttaqi, "A Novel Control Strategy for a Variable-Speed Wind Turbine With a Permanent-Magnet Synchronous Generator," *IEEE Trans. Ind. Appl.*, vol. 46, no. 1, pp. 331-339, 2010.

[53] I. Boldea *Variable Speed Generators*, CRC Press, Boca Raton, FL, 2006.

[54] K. Clark and N. W. Miller and J. J. Sanchez-Gasca, "Modeling of GE Wind Turbine-Generators for Grid Studies," GE Energy, Schenectady, NY, Aug. 2009.

[55] *RTDS Reference Manual*, RTDS, Inc., Winnipeg, Manitoba, Canada, 2009.

[56] R. Zavadil, N. Miller, A. Ellis, E. Muljadi, E. Camm, and B. Kirby, "Queuing up," *IEEE Power and Energy Magazine*, vol. 5, no. 6, pp. 47-58, Nov-Dec. 2007.

[57] J. Lopez, P. Sanchis, X. Roboam, and L. Marroyo, "Dynamic behavior of the doubly fed induction generator during three-phase voltage dips," *IEEE Trans. Energy Convers.*, vol. 22, no. 3, pp. 709-717, Sep. 2007.

[58] J. Morren and S. W. H. Haan, "Short-circuit current of wind turbines with doubly fed induction generator," *IEEE Trans. Energy Convers.*, vol. 22, no. 1, pp. 174-180, Mar. 2007.

[59] J. Morren and S. W. H. Haan, "Ridethrough of wind turbines with doubly-fed induction generator during a voltage dip," *IEEE Trans. Energy Convers.*, vol. 20, no. 2, pp. 435-441, Jun. 2005.

[60] D. Xiang, L. Ran, P. J. Tavner, and S. Yang, "Control of a doubly fed induction generator in a wind turbine during grid fault ride-through," *IEEE Trans. Energy Convers.*, vol. 21, no. 3, pp. 652-662, Sep. 2006.

[61] J. Niiranen, "Voltage dip ride through of doubly-fed generator equipped with active crowbar," presented at the Nordic Wind Power Conf., Gorhenburg, Sweden, Mar. 2004.

[62] H. Li and Z. Chen, "Overview of different wind generator systems and their comparisons," *IET Renew. Power Gener.*, vol. 2, no. 2, pp. 123-138, 2006.

[63] A. Mullane, G. Lightbody and R. Yacamini, "Wind-Turbine fault ride-through enhancement," *IEEE Trans. Power Syst.*, vol. 20, no. 4, pp. 1929-1937, Nov. 2005.

[64] J. F. Conroy and R. Watson, "Low-voltage ride-through of a full converter wind turbine with permanent magnet generator," *IET Renew. Power Gener.*, vol. 1, no. 3, pp. 182-189, 2007.

[65] A. Hansen and G. Michalke, "Multi-pole permanent magnet synchronous generator wind turbines grid support capability in uninterrupted operation during grid faults," *IET Renew. Power Gener.*, vol. 3, no. 3, pp. 333-348, 2009.

[66] N. D. Tleis, *Power Systems Modeling and Fault Analysis, Theory and Practice*, Burlington, MA: Newnes, 2008.

[67] Y. Zhou, P. Bauer, J. A. Ferreira, and J. Pierik, "Operation of grid-connected DFIG under unbalanced grid voltage condition," *IEEE Trans. Energy Convers.*, vol. 24, no. 1, pp. 240-246, Mar. 2009.